CESIUM ADSORPTION ON THE Zr/O/W(100) SURFACE

Hsiung-Ku Chen
B.Sc., Fu-jen University, Taiwan, 1974
M.S., Temple University, Philadelphia, 1976

A dissertation submitted to the faculty
of the Oregon Graduate Center
in partial fulfillment of the
requirements for the degree
Doctor of Philosophy
in
Applied Physics

July 1981

The dissertation "Cesium Adsorption on the Zr/O/W(100) Surface" by Hsiung-Ku Chen has been examined and approved by the following Examination Committee:

Lynwood W. Swanson, Thesis Advisor
Professor

Paul R. Davis,
Associate Professor

Richard A. Elliott
Associate Professor

Nicholas G. Eror
Associate Professor

Jon H. Orloff
Associate Professor

TABLE OF CONTENTS

Page

LIST OF TABLES

FIGURE CAPTIONS

Figure 1 The sequence of surface studies.

Figure 2 Schematic electronic potential energy diagram for a metal(M) - adsorbate(A) system when interaction is negligible. ϕ = work function; E_F = Fermi energy of M; I = ionization potential of A.

Figure 3 Schematic potential energy diagrams showing the position of an atomic level relative to the Fermi level of a metal substrate as a function of adsorbed atom - substrate distance, x. ϕ, substrate work function; M, substrate; A, adsorbate; I, ionization potential of adsorbate. Bell-shaped curves indicate broadening of A level. (Ref. 12).

Figure 4 Electron density distributions for the homogeneous background model of alkali adsorption on a high work function substrate.

Figure 5 Schematic of the experimental chamber.

Figure 6 Mass spectrum of the background gases with ultimate pressure of 4×10^{-10} torr.

Figure 7 Potential energy diagram for a field electron retarding potential analyzer.

Figure 8 The difference ϵ_p in energy between the peak of the TED curve and the Fermi level as a function of T and energy parameter d.

Figure 9 Diagram of the FERP gun.

ABSTRACT

CESIUM ADSORPTION ON THE Zr/O/W(100) SURFACE

Hsiung-Ku Chen, Ph.D.
Oregon Graduate Center, 1983

Supervising Professor: Lynwood W. Swanson

Interest in zirconium covered tungsten as an electrode material has been stimulated by recent work on the model surface Zr/O/W(100). This surface has been shown to have an effective thermionic work function of ~ 2.6 eV, when properly prepared, with very low volatility and excellent thermal stability. For advanced thermionic converter applications and for proposed future nuclear electric propulsion systems, the emitter requirement is $\phi_{eff} \leq 2.4$ eV at 1600 K. The corresponding collector must have a work function $\lesssim 1.4$ eV at ~ 600 K. For any electrode materials yet studied, these requirements dictate the presence of an equilibrium pressure of cesium vapor.

The adsorption/desorption characteristics of cesium in the Zr/O/W(100) surface and the effect of cesium coverage on the surface work function have been studied, using Auger electron spectrometetry (AES), field emission retarding potential work function measurements (FERP) and thermal desorption mass spectrometry (TDS). The minimum work function attained for cesium adsorption on the Zr/O/W(100) surface was 2.12 eV. The desorption spectrum of cesium from this

surface shows major binding states at 1.1 and 1.3 eV, with desorption complete at $T \leqslant 900$ K.

Adsorption of excess oxygen on the low work function Zr/O/W(100) surface increases the affinity of the surface toward cesium and lowers the minimum work function. Cesium adsorbed on a saturated layer of excess oxygen shows a terminal desorption temperature of 1300 K and minimum work function of 1.37 eV. Thermal equilibrium of the excess oxygen removes some oxygen and zirconium from the surface, changing the cesium adsorption characteristics.

Measurement of low energy electron reflection from the Zr/O/W(100) surface with and without adsorbed cesium indicates that the presence of cesium reduces the reflection coefficient of Zr/O/W(100) near the threshold beam potential for current collection.

Two adsorption sites for Cs adsorption on clean W(100) were found in the thermal desorption spectra. The Cs/W(100) bonding is stronger than the bonding of Cs on Zr/O/W(100) surface.

CHAPTER 1

INTRODUCTION

Interest in zirconium covered tungsten as a thermally stable, low work function surface has been stimulated by recent work on the model surface Zr/O/W/(100). The surface has been shown to have an effective thermionic work function of ~ 2.6 eV, with very low volatility and excellent thermal stability.[1]

The adsorption of alkali metals on the surfaces of various metals has received considerable attention because of its technological significance. If a fraction of a monolayer of alkali metal is adsorbed on a metal surface, its electron and ion emission properties are greatly altered. This phenomenon has very important implications in the development of thermionic converters and other physical electronics devices. The fact that alkali metals have the lowest ionization potential of all elements makes them very attractive for application in advanced energy conversion and ion propulsion devices requiring low-energy plasmas and ion beams. In this regard, particular interest is attached to cesium, which is widely used in thermionic energy converters. The cesium-tungsten system has been the subject of a rather large volume of investigation, from the classic article of Taylor and Langmuir,[2] up to quite recent studies. It is known that coadsorption of electropositive and electronegative elements on a metal surface can increase the electron

emission and reduce the work function of the surface more than adsorption of electropositive elements alone. For example, Cs/O/W(100) has a lower minimum work function (ϕ_m = 1.3 eV) than the ϕ_m = 1.6 eV of the Cs/W(100) surface,[3] and Cs/O/W(100) has a much lower ϕ_m = 1.02 eV than the ϕ_m = 1.45 eV of Cs/W(100).[4]

The purpose of this investigation was to gain understanding of the composite Cs/Zr/O/W(100) surface by studying the work function changes and thermal stability of Cs. The motivation for these measurements was the following: Since a low work function surface is needed for higher efficiency in thermionic energy converters (TEC), the main interest in this study was to determine whether a much lower work function could be achieved by Cs adsorption and Cs/O_2 coadsorption on the Zr/O/W(100) surface. Because the emitter electrode in a TEC operates at elevated temperature, it was also important to learn if the low work function surfaces were stable up to a high temperature. Because the knowledge of the surface structures on an atomic scale formed by adsorption on a solid surface is necessary for a complete understanding of that system and sometimes contributes to the interpretation of the kinetics of the adsorption process, the structural properties of clean and cesiated surfaces of Zr/O/W(100) were also studied. The electronic structure of alkali metal adsorption on metals has always been a concern in the interaction between alkali metal and metal surface. Thus, investigation of the chemical bonding in the systems Cs with Zr/O/W(100) and Cs with O/Zr/O/W(100)

was pursued.

The results obtained for Cs adsorption and Cs/O_2 coadsorption on Zr/O/W(100) using Auger electron spectrometry (AES), field emission retarding potential work function measurement (FERP), thermal desorption mass spectrometry (TDS) and low energy electron diffraction (LEED) are reported here. The surface structure, work function and thermal desorption energy measurements are all made concurrently on the same surfaces in the same UHV system. Therefore, the results can be correlated without any doubt that each separate measurement is made under equivalent conditions. The analytical tools and surface properties to be measured are outlined in Table I.

Since Cs/W(100) is a well studied surface, the main purpose of Cs/W(100) investigation in this study was to compare with the work of J.-L Desplat[3] to verify the analysis techniques used. Also, a comparison between the Cs/W(100) and Cs/Zr/O/W(100) systems can be made. In addition, the TDS of Cs/W(100) was studied because it has not been reported previously in the literature. The sequence of various surfaces which were investigated in this study is shown in Figure 1.

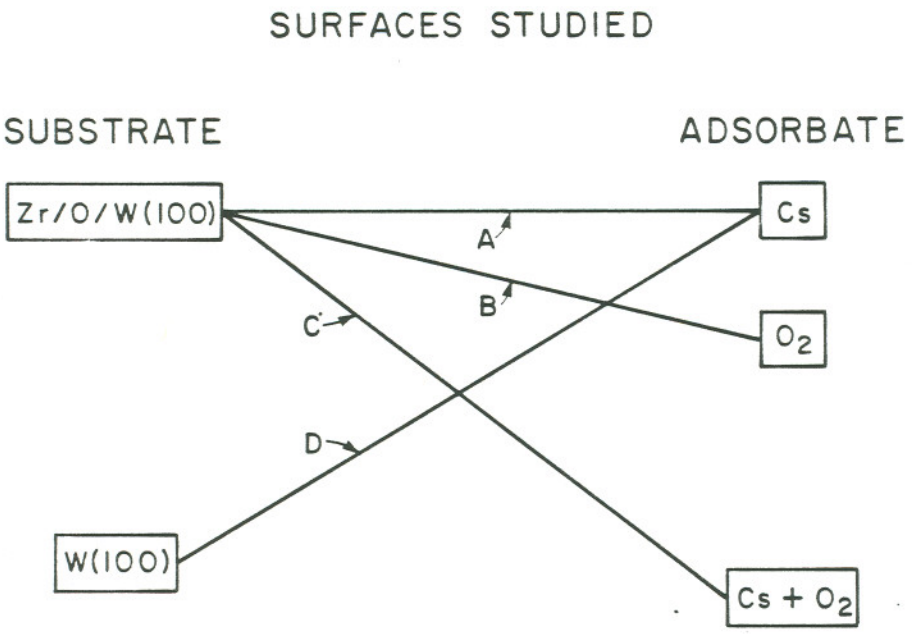

Figure 1. The sequence of surface studies.

TABLE I

CESIATED SURFACE CHARACTERIZATION ANALYSES AND TOOLS

EXPERIMENTAL METHODS OF APPROACH

CHARACTERIZATION TECHNIQUE	STRUCTURE	COMPOSITION	WORK FUNCTION
FERP			X
AES (RFA)		X	
MASS SPECTROMETRY		X	
LEED	X		

The adsorption of Zr onto W surface has received considerable study, primarily by field emission microscopy. The following is a brief literature review related to these studies.

V.N. Shrednik[5] showed that with a monoatomic coating the work function of Zr on W in the (100) crystallographic regions decreases to 2.62 eV. R.A. Collins and B.H. Blott[6] found that, during adsorption of zirconium on clean tungsten at residual pressures below 1×10^{-10} torr, it was necessary to outgas the Zr source above ~ 2400 K to obtain reproducibility, and that the presence of oxide contamination lowered the work function. The ring structure on the (100) regions, previously noted in field emission patterns by Shrednik, was only observed with Zr deposits from a contaminated source. A LEED and RHEED study of the adsorption of zirconium on single crystal W(100) substrate was carried out by Hill et al.,[7] although source purity could not be guaranteed due to lack of an Auger spectrometer. Deposition onto a substrate at room temperature gave rise to a (1 x 1) pseudomorphic layer of zirconium with increasing order up to 600 K. Higher temperature annealing of monolayer deposits led to a new surface structure, W(100) C(4/3 x 2) - Zr, at roughly three-quarter monolayer coverage.

L.W. Swanson and L.C. Crouser[8] showed that Zr/W field cathodes possess the following desirable properties:

1. Low work function (2.6 - 2.8 eV);

2. High degree of thermal stability (i.e., stable up to 1700 K);

3. Selective lowering of the (100) plane work function, thereby causing a high degree of beam confinement along the (100) emission direction. If a well outgassed zirconium source is employed, preferential lowering of the work function of the (100) crystal faces of tungsten was not obtained.[9]

P.R. Davis,[10] showed that Zr adsorption at $T \leqslant 350$ K causes a work function decrease of 1.1 eV from the clean value at $\theta = 1/2$, and a layer that grows pseudomorphically as indicated by a (1 x 1) LEED pattern over the entire coverage range $0 < \theta \leqslant 1$. In contrast, adsorption at $900 \leqslant T \leqslant 100$ K yields a minimum work function 0.6 eV below the clean value, at $\theta = 1/2$, and a concurrent sharp c(2 x 2) pattern which returns to (1 x 1) at $\theta = 1$.

CHAPTER 2

WORK FUNCTION

Since Taylor and Langmuir's classic study of cesium adsorption on tungsten there have been several attempts to formulate theories of alkali adsorption.

2.1 Classical Studies of Electronic Structure and Bonding

The theoretical model has been derived from the original Taylor and Langmuir work.[8] Realizing that the ionization potential of unperturbed cesium is less than the work function of metals such as tungsten and that cesium is physically a large atom has led to the following simple picture. The alkali atom is adsorbed on a metal surface basically as an ion. The ion-metal interaction is described by the classical image force. The surface dipole formed was believed to explain the observed reduction of work function with surface coverage. In addition, the attraction between the alkali metal ion and its image was considered to give rise to the bonding force. The reduction of the dipoles with coverage was explained by mutual field depolarization using some form of the Topping formula.[11]

Since the Taylor-Langmuir work, there have been many other measurements of the work function, of electron and ion emission, and of desorption energy of alkali metal on metal substrate system. These measurements have shown the inadequacies of the classical theory.

First, the adsorbed alkali metal is usually not completely ionic. Second, the metal substrate is not a perfect conductor with an atomically smooth surface. Third, the classical theory does not fit work function curves at coverages approaching one layer[12]. The field depolarization allowed for in the classical theory is an oversimplified point of view, since orbital overlapping is overlooked and is known to be important at high coverages. Fourth, the contribution of covalent bonding is commonly neglected.[12] These inadequacies can be remedied to some degree by wave mechanical treatments.

2.2 Wave Mechanical Treatments of Electronic Structure and Bonding

Gurney[13] originally noted that the interaction of an atom with a metal causes the valence level of the atom to become broadened. He then noted that this broadening could result in the formation of polar bonds between the adsorbate and substrate which were not necessarily ionic in character. The work of Gomer and Swanson[14] has provided criteria, based on Gurney's suggestion, for establishing the nature of the adsorbate-substrate bond, that is, whether it is ionic, polar metallic, or covalent. They point out that the position of the shifted and broadened ns level (n is the principal quantum number of the valence electron of the particular alkali in question) relative to the occupied portion of the conduction band largely determines the nature of the bond. They considered the metal (M) and the adsorbate (A) as potential wells (Figure 2) and inquired

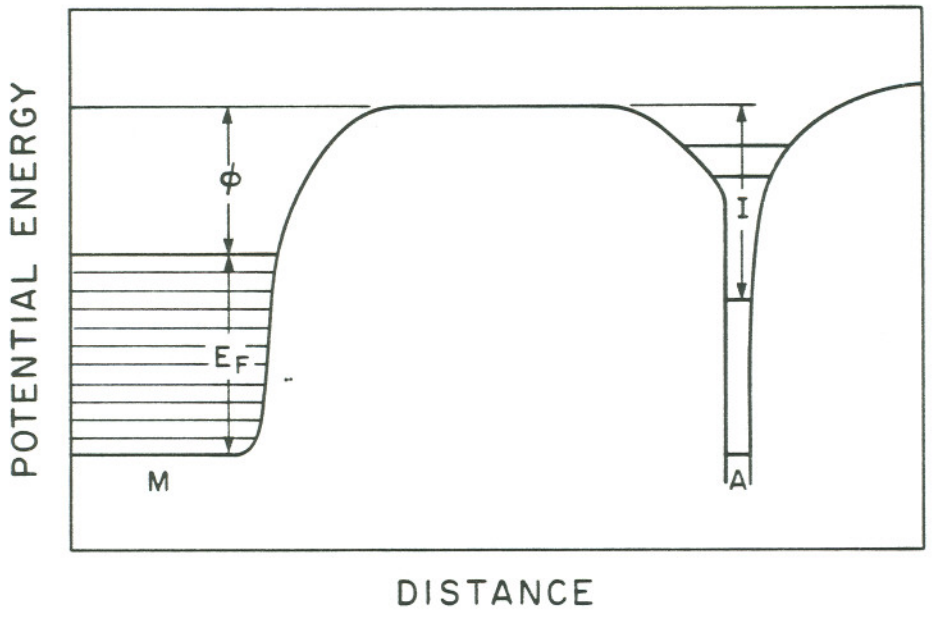

Figure 2. Schematic electronic potential energy diagram for a metal (M) - adsorbate (A) system when interaction is negligible. ϕ = work function; E_F = Fermi energy of M; I = ionization potential of A.

into the electron energy levels and their population in various quantum system as the M-A separation x is decreased.

In order to understand the electronic situation it is useful to construct electronic potential energy diagrams in which the adsorbate level is plotted as a function of adsorbate-surface distance.[12,14] It is seen from Figure 3 that four cases must be considered. If I is only slightly larger than ϕ, the effect of image level will raise the adsorbate level above the Fermi level at $x \leqslant x_c$. In this case ionic desorption can result if the adsorbate band is empty when x is slightly less than x_c. Neutral desorption in this case corresponds to an adiabatic transition in which an electron tunnels into the adsorbate level at $x > x_c$. If the adsorbate level does not remain above the Fermi leval, at $x < x_c$, ionic adsorption is excluded and metallic adsorption occurs. The third case is that where $I < \phi$ which leads to ionic adsorption and desorption. The fourth case is adsorption by localized bonding, where $I - \phi - 3.6/x$ (where 3.6/x is the image potential in eV if x is in Å) for the unperturbed A level falls below the conduction band.

Duke and Alferieff[15] treated the substrate-adsorbate interface with a one-dimensional exactly soluble pseudopotential model. They concluded that the presence of an atomic valence level in the adsorbate can cause resonance transmission of electrons through the potential barrier during field emission. Experimental evidence was offered for zirconium on tungsten.[16] Gadzuk et al., found that the

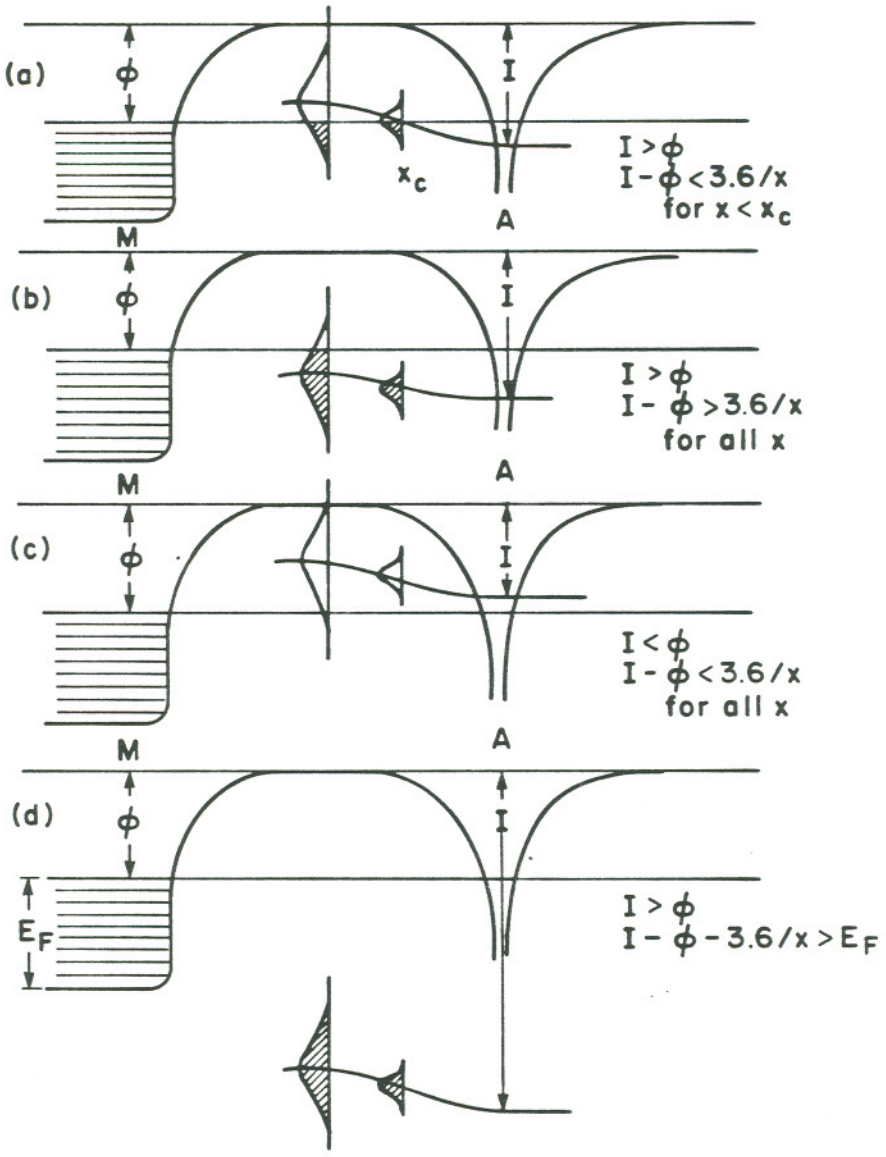

Figure 3. Schematic potential energy diagrams showing the position of an atomic level relative to the Fermi level of a metal substrate as a function of adsorbed atom - substrate distance x. ϕ, substrate work function; M, substrate; A, adsorbate; I, ionization potential of adsorbate. Bell-shaped curves indicate broadening of A level. (Ref. 12)

enhanced tunneling probability through the Zr atoms is related to the 'atomic band' of Zr which is shifted by $\Delta E \sim 1.0 - 1.5$ eV with a width $\Gamma \sim 1$ eV. This enhanced tunneling will result in a large current density increase and structure in the energy distribution not predicted by the Fowler-Nordheim (F-N) model of field emission.

Gadzuk[17] has extended the work of Duke and Alferieff to a three-dimensional model using time-dependent perturbation theory. It was noted that the interaction of a metal with an alkali atom caused both a shift and broadening of the valence level of the alkali atom. The first-order ns energy-level shift ΔE and the valence level broadening Γ were $\sim +0.3$ eV and $\leqslant 1$ eV respectively. It was also found that the position of the shifted and broadened level relative to the conduction band of the metal is such that the ionic bonds are formed between adsorbate and substrate at low coverage. This theory is able to predict dipole moments in good agreement with experimental values for alkali metals adsorbed on Ni.[18]

In a series of papers, Lang and Kohn[19-21] presented a "jellium" model of a metal surface and treated work function changes from first principles. Using the theory of an inhomogeneous electron gas, with local exchange and correlation energies, self-consistent electron density distributions were obtained. A self-consistent quantum-mechanical analysis of the model leads to a work function vs coverage curve with a minimum at a coverage below that of a single full adsorbed layer, and a maximum at completion of the layer. The ionic lattice of the substrate was replaced by a semi-infinite

homogeneous distribution of positive charge of density $\bar{n}_{sub}$ filling the half space $x < 0$, as shown in Figure 4. The sheet of ions of the adsorbate layer is replaced by a homogeneous positive slab of density $\bar{n}_{ads}$ and thickness d, adjoining the substrate background. The density distribution of positive charge is denoted by $n_+(x)$, and the density distribution of negative charge is denoted n(x), where

$$n(x) = \begin{cases} 0 & x > d \\ \bar{n}_{ads} & 0 < x < d \\ \bar{n}_{sub} & x < 0 \end{cases} \qquad (1)$$

Metals are characterized by a mean electron density $\bar{n}$ and atomic radius r_s where $4/3\pi\, r_s^3 \equiv n^{-1}$. The adsorbate density $\bar{n}_{ads}$ satisfies the relation $\bar{n}_{ads}\, d = N$, where N is the number of adatoms per unit area. It is assumed that the estimate of N for the fully packed first adsorbate layer is obtained simply by taking it to be the number of atoms per unit area in the most densely packed planes of bulk crystal of the alkali. It seems reasonable to take d to be the corresponding interplanar spacing. The work function ϕ is given by $\phi = \Delta\phi - \bar{\mu}$ (1) where $\bar{\mu}$ is the chemical potential in the interior of the system relative to the electrostatic potential, and $\Delta\phi$ is the difference in electrostatic potential for an electron crossing the surface, i.e.,

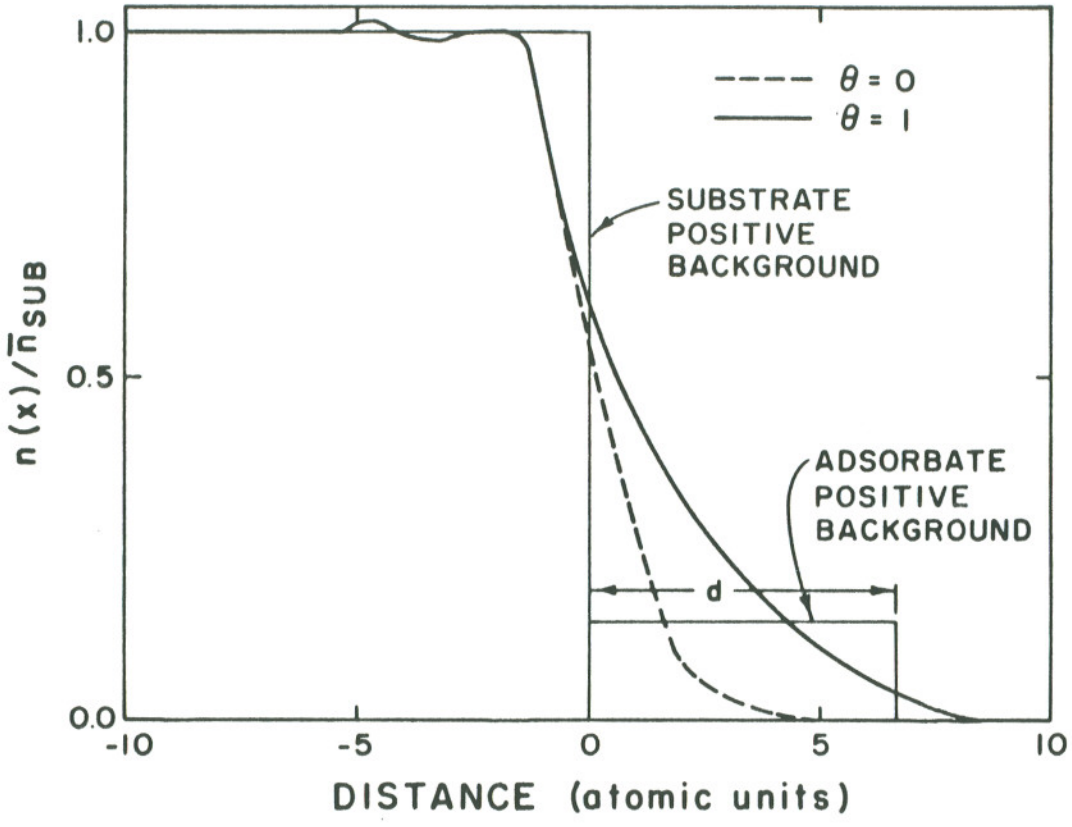

Figure 4. Electron density distributions for the homogeneous background model of alkali adsorption on a high work function substrate.

$$\Delta\phi = 4\pi \int_{-\infty}^{\infty} dx\, x[n(x) - n_{+}(x)] \qquad (2)$$

The $\phi(\theta)$ relation can be obtained by using the computed density distributions in conjunction with equations (1) and (2). Good agreement with the results of recent measurements was obtained for these extremal values and, though not designed to treat very low coverages, the model yields an initial dipole moment in satisfactory agreement with experiment. The computed full layer work function of adatoms A is very nearly equal to that obtained theoretically for the corresponding bulk sample of A.

A different approach is the application of molecular orbital (MO) theory to surface bonding. Gyftopoulos and Levine[22] have derived a semi-quantitative theory to account for the variation of the work function of refractory metals coated by metallic films for all degrees of coverage. This approach is based on an extension of the concept of electronegativity and dipole moment of complex molecules. The model expresses the work function as a simple sum of a dipole barrier $d(\theta)$ and an electronegativity barrier $e(\theta)$:

$$\phi(\theta) = e(\theta) + d(\theta)$$

$$= \phi_f + (\phi_m - \phi_f)\, G(\theta) - \frac{\theta\, G(\theta)\, \sigma_f\, M_o}{\epsilon_o\left(1 + 9a\sigma_f^{3/2}\, \theta^{3/2}/4\pi\epsilon_o\right)} \qquad (3)$$

where θ = coverage in monolayers, ϕ_f = adsorbate work function, ϕ_m = metal substrate work function, $G(\theta) = 1 - 3\theta^2 + 2\theta^3$, σ = number of adsorption sites in one monolayer, α = polarizability of adsorbate-substrate molecules, and M_o = substrate-adsorbate dipole moment. It is shown that the maximum work function change does not necessarily occur either when a full monolayer is reached or at a definite fractional coverage. This model predicts the work function increase observed for adsorption of silicon and boron on a tungsten substrate.[23]

Steiner and Gyftopoulos[24] proposed a novel equation for the computation of the base work functions of metallic surfaces of different crystallographic orientation. This equation is based on the view that the work function can be expressed in terms of properties of atoms as they exist on the metal surface. The neutral-electronegativity X(0) is interpreted as the work required to remove a valence electron from an atom without altering the energy state of the atom, and this type of electron removal occurs at a metal surface. Thus,

$$\phi \equiv X(0) = 0.98 \left(\frac{V_s + 1}{r_m} \right) + 1.57 \qquad (4)$$

where V_s is the number of electrons per surface atom which participate in bonding, and r_m is the effective size of these atoms in Å. Steiner and Gyftopoulos have extended these concepts to surfaces coated by metallic adsorbates. Pauling's rules[25] and

and formulas for the electronegativity and dipole moment of a complex molecule are then applied to calculate the work function and binding energy as a function of alkali metal coverage. These theories are among the few which account for covalent bonding and the overlapping of alkali metal atom orbitals at moderate and high coverages, as well as classical field depolarization effects. Attempts to fit the work function versus surface coverage curves with the Steiner-Gyftopoulos theory for alkali metal adsorption on single crystal Ni surfaces were made,[26] but the fits were generally poor.

CHAPTER 3

EXPERIMENTAL

3.1 System and Sample Preparation

The experiments carried out in this study were performed in an ion-pumped chamber with ultimate pressure of 4×10^{-10} torr (Figure 5). Background gasés were monitored with a quadrupole mass analyzer (QMA) and consisted primarily of CO and H_2 (Figure 6). The F in the QMA spectrum is not a background gas. It is F^+ ESD (electron stimulated desorption) ions from ionizer surfaces. The spectrum also contained CO_2, Cl_2 and Cs as background components. The tungsten crystal used in this study was electropolished so as to form a smooth surface and its orientation was determined to be within 1° of the <100> direction by Laue x-ray diffraction. The crystal was mounted so it could be resistively heated to 1700 K or heated by electron bombardment to 2400 K. Sample temperatures were monitored by a W-5% Re versus W-26% Re thermocouple spot-welded to the crystal and were checked at high temperature with an optical pyrometer. Estimated uncertainty in quoted temperature values is ± 10K.

Zirconium was supplied from a resistively heated W wire onto which Zr was melted. The source could deposit reproducible doses of Zr with less than 1% O and 2.5% C in the adsorbed layer, as

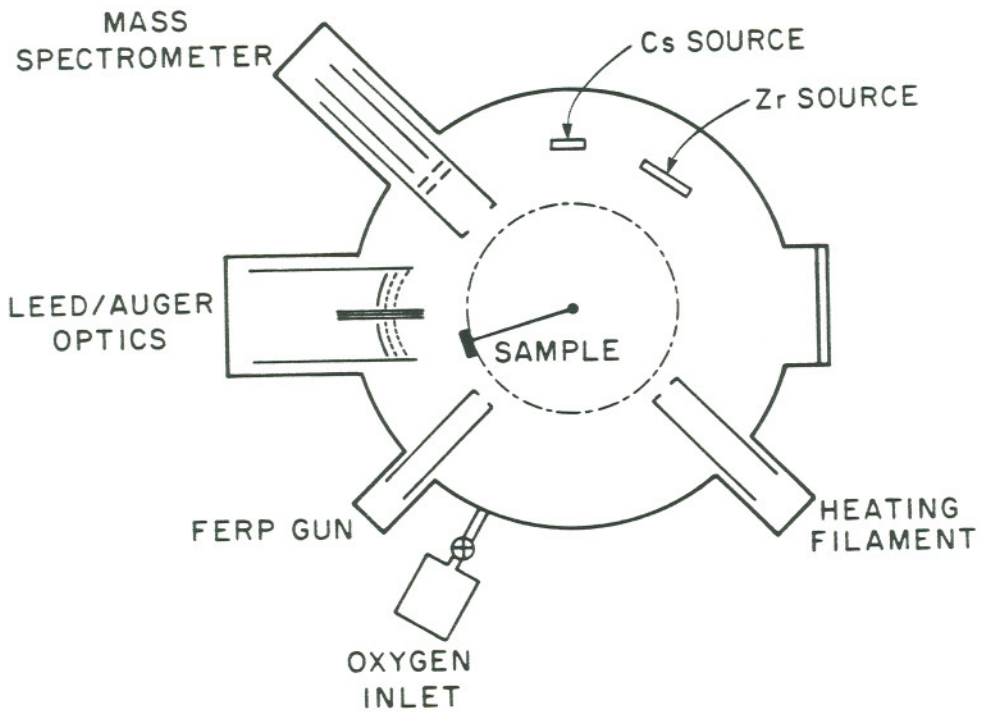

Figure 5. Schematic of the experimental chamber.

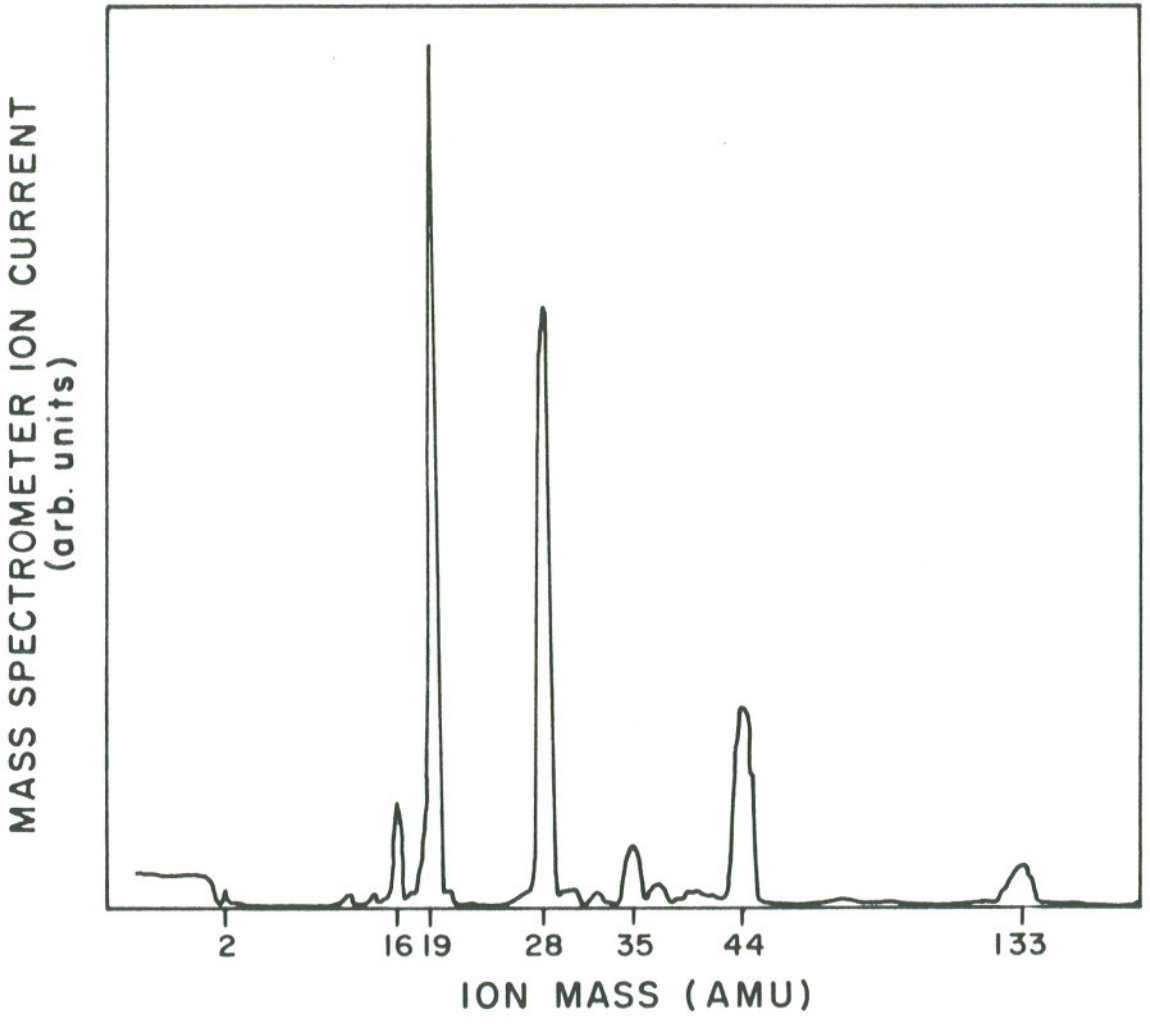

Figure 6. Mass spectrum of the background gases with ultimate pressure of 4×10^{-10} torr.

monitored by AES.[27] Cesium was deposited from a SAES Cs dispenser source, which has been described elsewhere.[28] Oxygen was supplied from a high purity bottle via a Varian leak valve, and the QMA was employed to monitor gas purity and O_2 exposure.

The Zr/O/W(100) low work function surface (2.6 eV) was prepared by the following treatment:

1. The crystal was cleaned of adsorbed residual gas by electron bombardment to 1900 K before each experiment.

2. Several monolayers of zirconium were initially deposited on the W(100) crystal after which it was heated to 1500 K for 2 minutes in 1×10^{-7} torr O_2.

3. The crystal was then heated to 2100 K for 10 sec. in background pressure $< 2 \times 10^{-9}$ torr.

In the latter part of this study, it was found that Zr could not be removed completely from the W surface even after flashing at 2400 K. After repeated cycles of 2 min. O_2 adsorption in 10^{-7} torr, followed by flashing to 2400 K, there was still a slight amount of Zr left even though the work function of this surface was ~ 4.65 eV. The Zr coverage θ_{Zr} in this surface is around 0.10. This result probably implies that there was significant Zr in the bulk due to bulk diffusion. Hill et al.,[7] have observed that the tightly bound pseudomorphic zirconium layer remains until 2300 K where it was removed by a combination of evaporation (vapor pressure of bulk zirconium at 2300 K is 10^{-4} torr), and solution into the tungsten. Danielson and Swanson[1] have shown by ion sputtering and depth profiling a

Zr/O/W(100) crystal after repeated Zr dosings that the zirconium and oxygen are present in the bulk to a depth of at least 8000 monolayers. Zr - O complex diffusion out of the bulk and segregation in the surface region occurs upon heating in vacuum.

3.2 Work Function Measurement

3.2.a General Theory of FERP Analysis

The field emission retarding potential method (FERP)[29] was used to measure the absolute work function of the surface for sample temperatures below 400 K. The potential energy diagram of Figure 7 illustrates the essential features of the FERP method. The high electrostatic field applied to an emitter surface narrows the potential barrier, so that electrons occupying energy levels near the Fermi level can tunnel through the barrier. The emitted electrons are accelerated in the region between the emitter and anode, and are then retarded in the region between the anode and the collector. If the collector is connected electrically to the emitter, the Fermi levels of the two metals are at the same level, and the emitted electrons are stopped by a potential barrier at the collector surface equal to its work function ϕ_c. To collect the field emitted electrons, a voltage V_c with a magnitude (with respect to the emitter) equal to or greater than ϕ_c must be applied to the collector. Thus at 0 K the onset of current at the collector occurs when $V_c = \phi_c$, the collector work function. The shape of the current-voltage curve $I_c\ (V_c)$ is determined primarily by the energy distribution of the

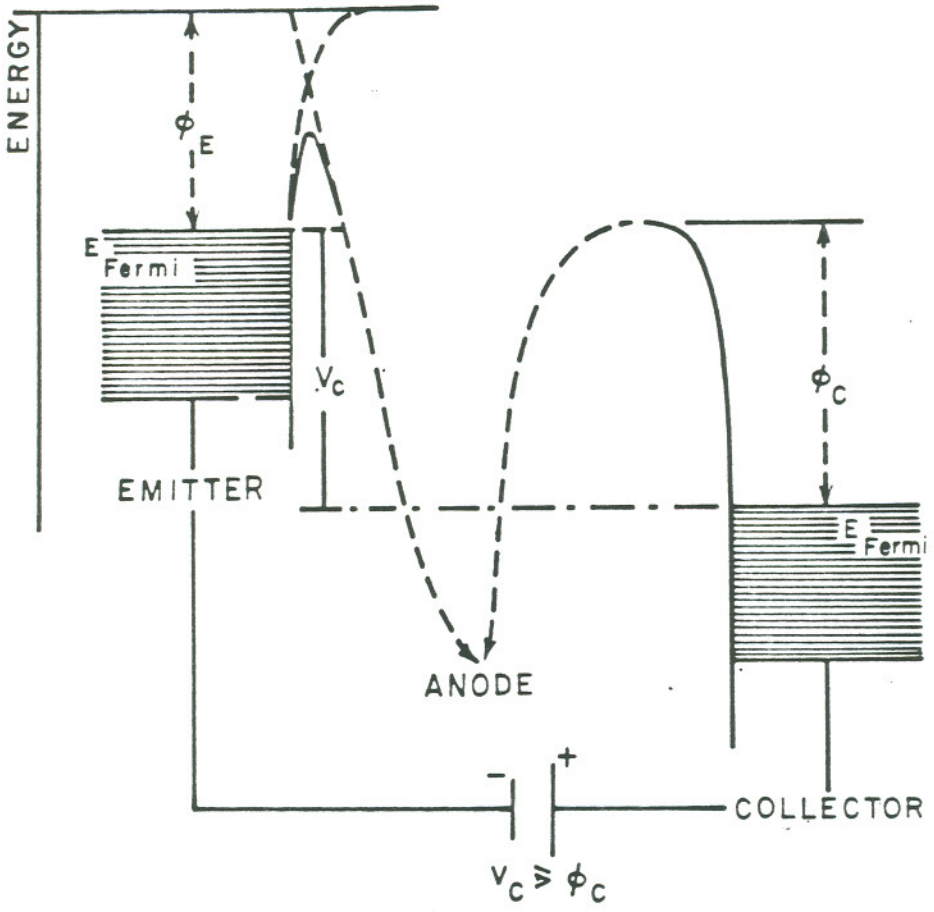

Figure 7. Potential energy diagram for a field electron retarding potential analyzer.

emitted electrons; for an emitter at a temperature T the current density per unit total energy $J(\epsilon)$ is (assuming the Sommerfeld free electron model for the electron distribution among the energy levels within the metal):

$$J(\epsilon) = J_o \, e^{\epsilon/d} \Big/ \left(1 + e^{\epsilon/kT}\right) \qquad (5)$$

where J_o is the total emitted current density at 0 K, ϵ is the energy of an electron relative to the Fermi level ($\epsilon = E - E_f$) and the value of d is given by $d \doteq 9.3 \times 10^{-9} \, F/\phi_e^{\,1/2}$ (eV) where F is the value of electric field in V/cm applied to the emitter surface and ϕ_e is its work function in eV. Equation (5) may be differentiated with respect to the electron energy ϵ to obtain the difference in energy between the peak of the electron energy distribution and the Fermi level $\epsilon_p = kT \, \ell n[kT/(d - kT)]$. This equation is plotted in Figure 8 and it is used as the basis of determining the work function of the collector.

3.2.b Method

The peak position of the differential of the I-V characteristics to is used to determine ϕ_c. From Figure 8 the work function of the collector is given by $\epsilon_p = \phi_c - V_p$. Since V_p (the position of maximum dI_c/dV_c on the energy scale) can be obtained experimentally, the value of ϕ_c can be obtained from the TED curve and Figure 8. In practice, $\epsilon_p \doteq 30$ mV and this method gives ϕ_c easily within 1%

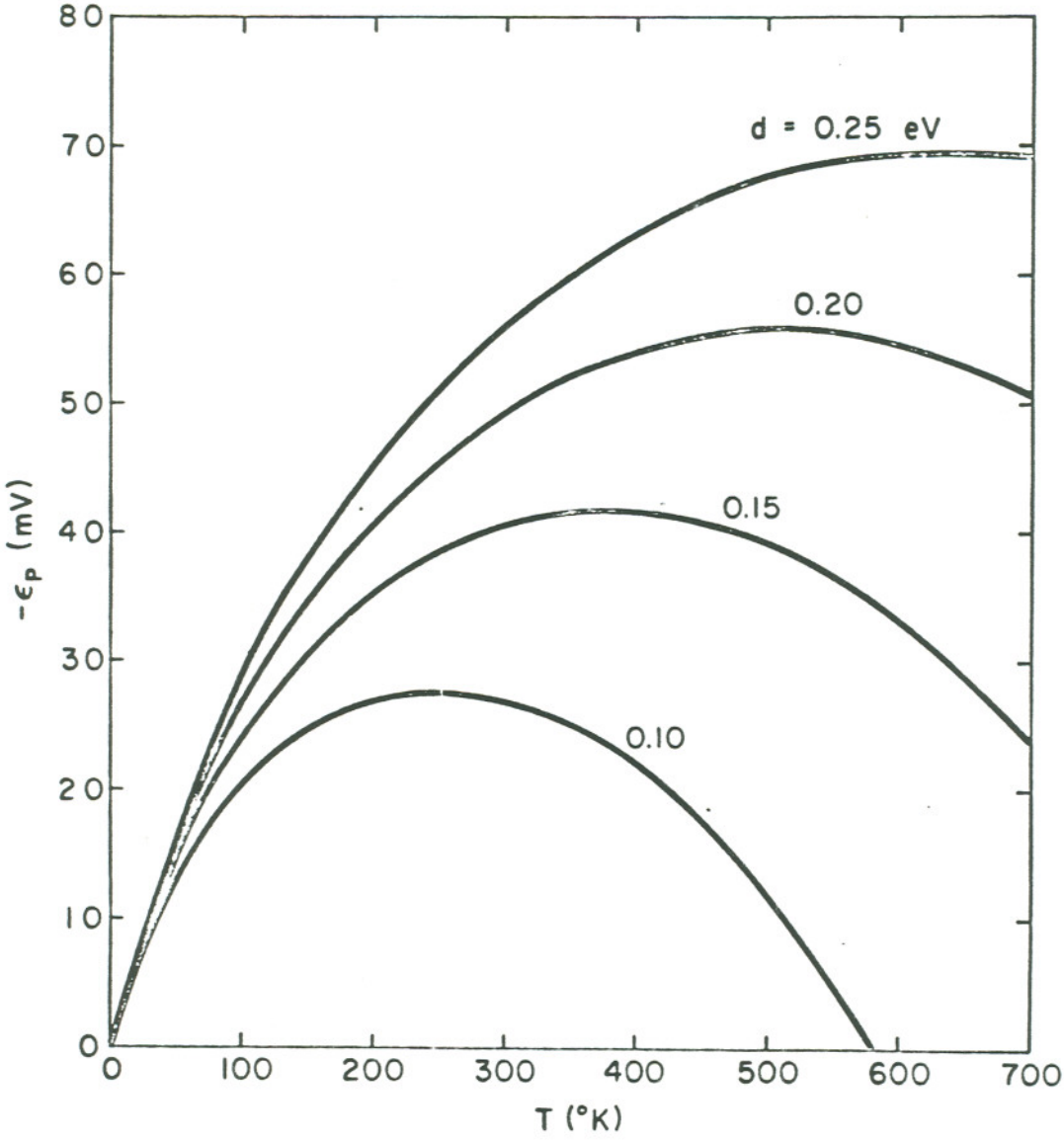

Figure 8. The difference ϵ_p in energy between the peak of the TED curve and the Fermi level as a function of T and energy parameter d.

accuracy. The error in ϕ_c due to this method is the sum of the errors in ϵ_p due to the uncertainty in d, the accuracy of the meter measuring V_c, and the uncertainty in the exact position of the peak of the differential curve.

3.2.c. Experimental Set-up

The diagram of the FERP gun is shown in Figure 9. The electrostatic focusing system used in the analyzer consisted of an anode, two Einzel lenses and a 250 line/in. decelerating mesh electrode which established parallel equipotential surfaces in front of the collector. The FERP measurement circuit diagram is shown in Figure 10. After preamplification the sample current I_c is sent to the input of the PAR lock-in amplifier. A differential curve is obtained by synchronous detection of the modulated collected current, using a 1500 Hz tip modulation of 50 mV peak-to-peak. Thus, the magnitude of the signal detected by the lock-in amplifier was proportional to dI_c/dV. In this study the emitter orientations used for the field electron source were <111> and <310> tungsten. Previous study[30] has shown that electrons field emitted from these orientations exhibit energy distribution curves that agree closely with the Sommerfeld free electron model. Furthermore, the work functions of the crystal planes intersecting these directions are quite low - 4.3 eV for the (310) plane and 4.4 eV for the (111) plane - thereby providing the highest beam transmission values. The

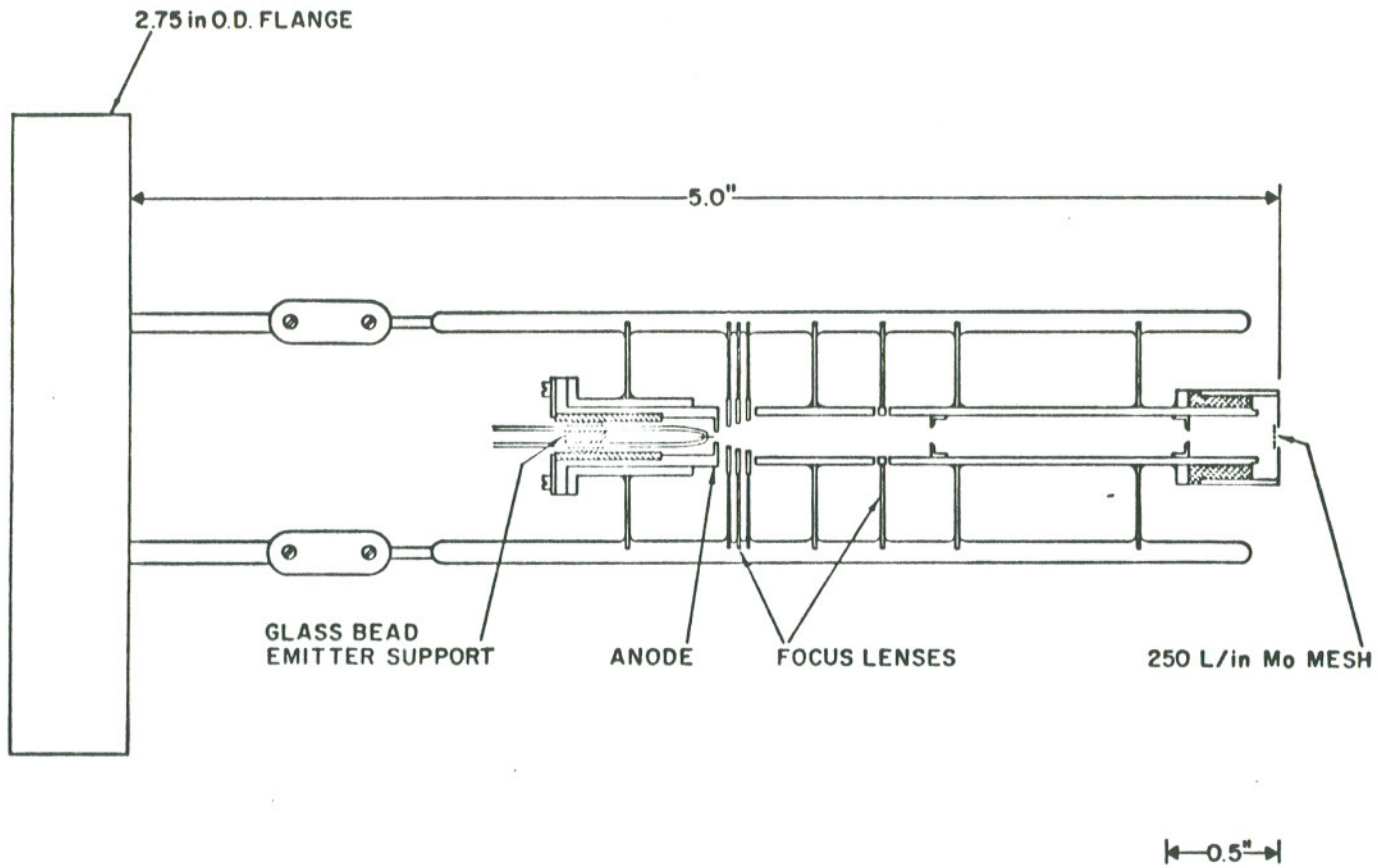

Figure 9. Diagram of the FERP gun.

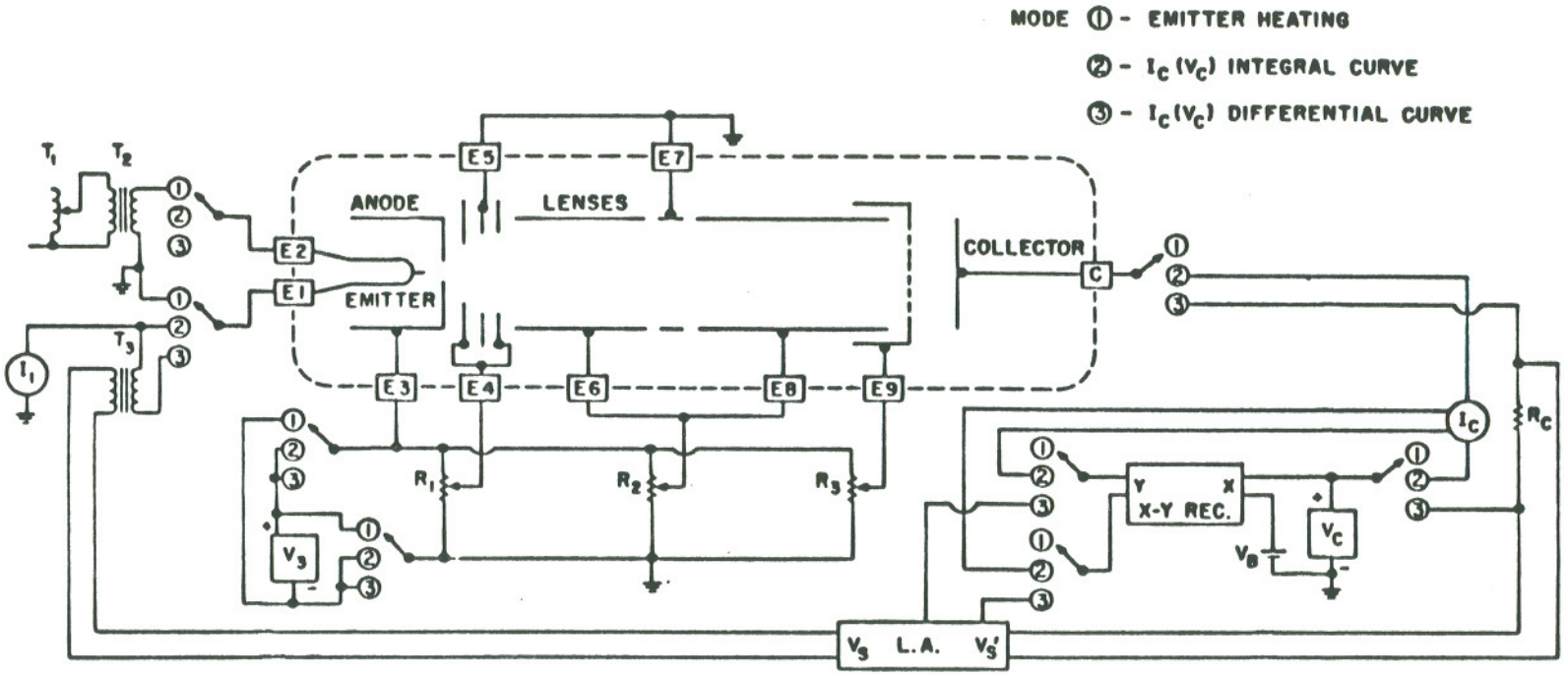

Figure 10. Schematic diagram of FERP measurement circuit.

emitter surface was cleaned by thermal flashing of the emitter at 1800 K to 1900 K. Repeated heating of the emitter tends to dull it somewhat, and thus change its current-voltage characteristics. A total emitter current of ~ 1 μA was used. Focusing was accomplished by adjusting the lens voltages to maximize the slope of the leading edge of the differential $I_c(V_c)$ curve, yielding a minimum voltage difference between 10% and 90% of the peak value of this curve. In this study, a 10-90% difference of less than 125 meV was achieved. This value is close to the theoretical value whereas T = 300 K and a FWHM value of the energy analyzer resolution is 0.05 eV, the 10-90% voltage difference on the E.D. leading edge of the differential curve is 110 meV.

3.2.d. Advantages and Disadvantages of the FERP Technique

The advantages of FERP measurements are the following:

1. The absolute work function is measured.
2. No reference electrode is used.
3. No damage to the sample occurs.
4. No sample heating is required, except for cleaning.
5. FERP I(V) characteristics give the electron reflection coefficient.

The disadvantages are the following:

1. If electron reflection occurs near the threshold of the collection, results of the ϕ determination may be ambiguous.

2. The method is less sensitive than other techniques because of the low collected current.

3. System vacuum must be better than 1×10^{-9} torr during a measurement.

4. Measurement is difficult when the sample is at elevated temperatures.

5. Sample alignment with the FERP gun is critical for minimum 10-90% voltage values on the leading edge of the differential curve.

6. The work function may need to be corrected for patch field effects when various surfaces of a polycrystalline sample are involved.[31] Due to the smooth tungsten single crystal sample used in this study, no such correction was necessary.

3.3. Auger Measurement

3.3.a. General Theory

The Auger electron spectroscopy mechanism can be divided into the following sub-mechanisms:

1. Ionization of core levels

An ionizing radiation is made to impinge on the surface to be studied, with energy sufficient to create electron core holes within the atoms in the surface region.

2. Auger de-excitation

Excited atoms with deep lying core holes undergo internal electronic rearrangement to a state of lower energy. The energy released may be carried away via a radiative photon emission or a non-radiative electron emission process. The latter process leaves the atom doubly ionized, and the ejected electron is known as an Auger electron. In this process, a core hole in the level W is filled by an electron from the level X and the energy change causes emission of an electron from the level Y (see Figure 11).

3. Characteristic Emission

The kinetic energy of an Auger electron is determined by differences in discrete bound states of an atom, with energy levels characteristic of the particular atomic number Z. We shall assume that all binding energies are measured relative to the Fermi level. In principle the kinetic energy of an Auger electron, E, measured relative to the vacuum level at the specimen surface in a WXY de-excitation transition is $E = W - X - Y - \phi$. The emission intensity of a particular Auger transition, WXY, is proportional to the current of ionizing particles traversing the escape volume, the density P_w of atoms within the escape volume having an ionizable bound level, and the probability that an ionizing event will occur in the level W. The escape volume is defined by using the projected area of the incident beam on the specimen surface, $A_p/\cos\beta$, where the cross section area is A_p and β is the angle between the beam direction and the surface normal.

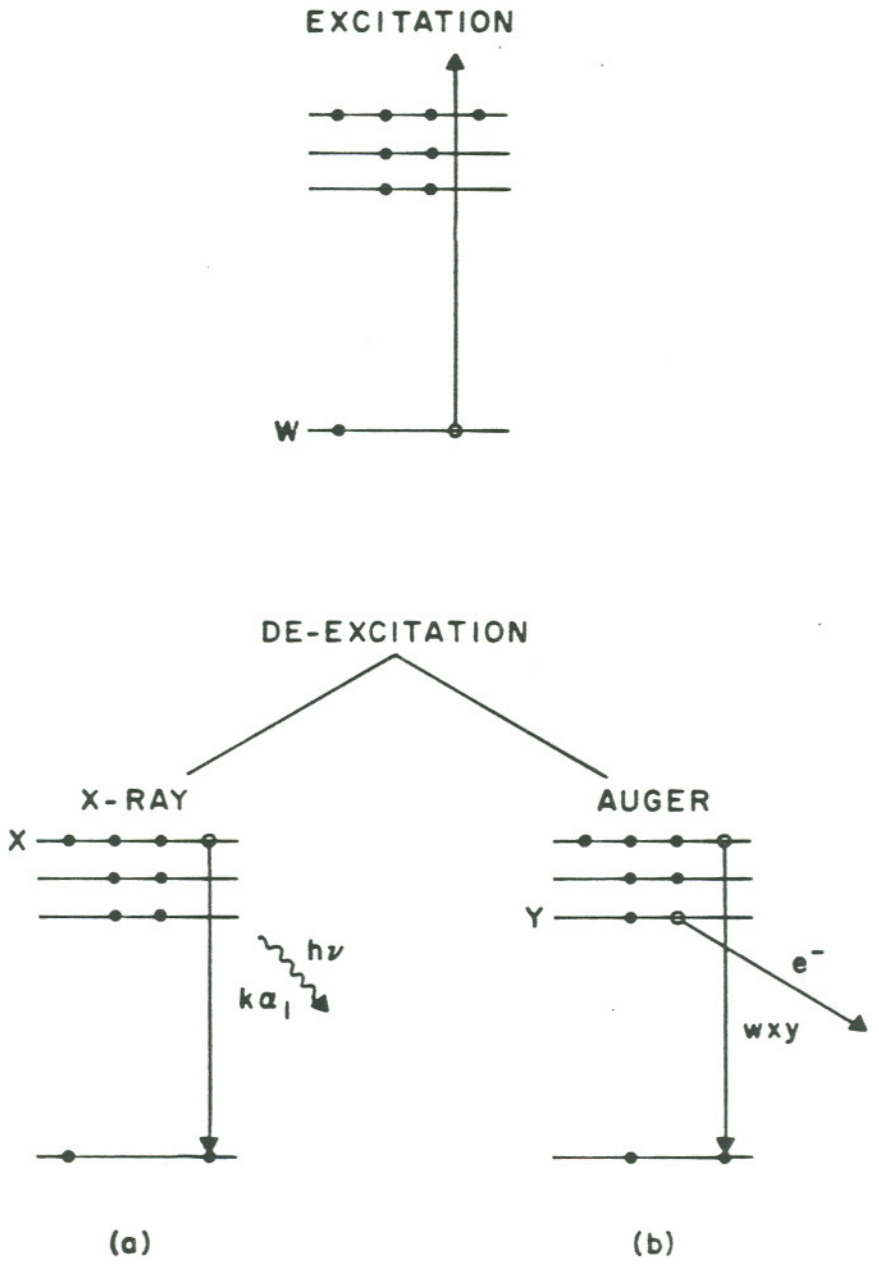

Figure 11. Processes for de-excitation of atomic core holes: a, emission of x-rays; b, emission of an Auger electron.

The primary beam generally has an energy considerably in excess of the binding energy of the level W. Therefore, it penetrates the solid to depths greater than the depth from which the WXY Auger electrons can escape without attenuation due to inelastic scattering. Consequently, it is convenient to define an escape volume $A_p \lambda(E)/\cos\beta$ for an Auger electron having an energy E. Thus the Auger current i(WXY) is proportional to $i_p(1 + r)\rho_W \lambda(E)\sigma(E_p,W)/\cos\beta$. The quantity r, a portion of the incident beam, is subject to elastic scattering and may pass through the volume a second time. Thus, r is a back scattering correction. The probability that a primary electron of energy E_p can cause an ionization event in the bound state W is given by the cross section $\sigma(E_p,W)$.

3.3.b. Experimental Set-Up

The schematic diagram of four grid LEED-Auger device as a retarding field analyzer is shown in Figure 12. The negative potential U_r applied to the repeller grids is varied continuously between $-U_{max}$ and zero. The collector current $i(U_r)$ as a function of the retarding potential U_r is given by

$$i(U_r) \propto \int_{E = eU_r}^{\infty} N(E)dE \qquad (6)$$

where N(E) is the energy distribution of secondary electrons emitted from the sample. The Auger peaks in the N(E) distribution appear as small steps on a slowly varying background in the $i(U_r)$ curves.

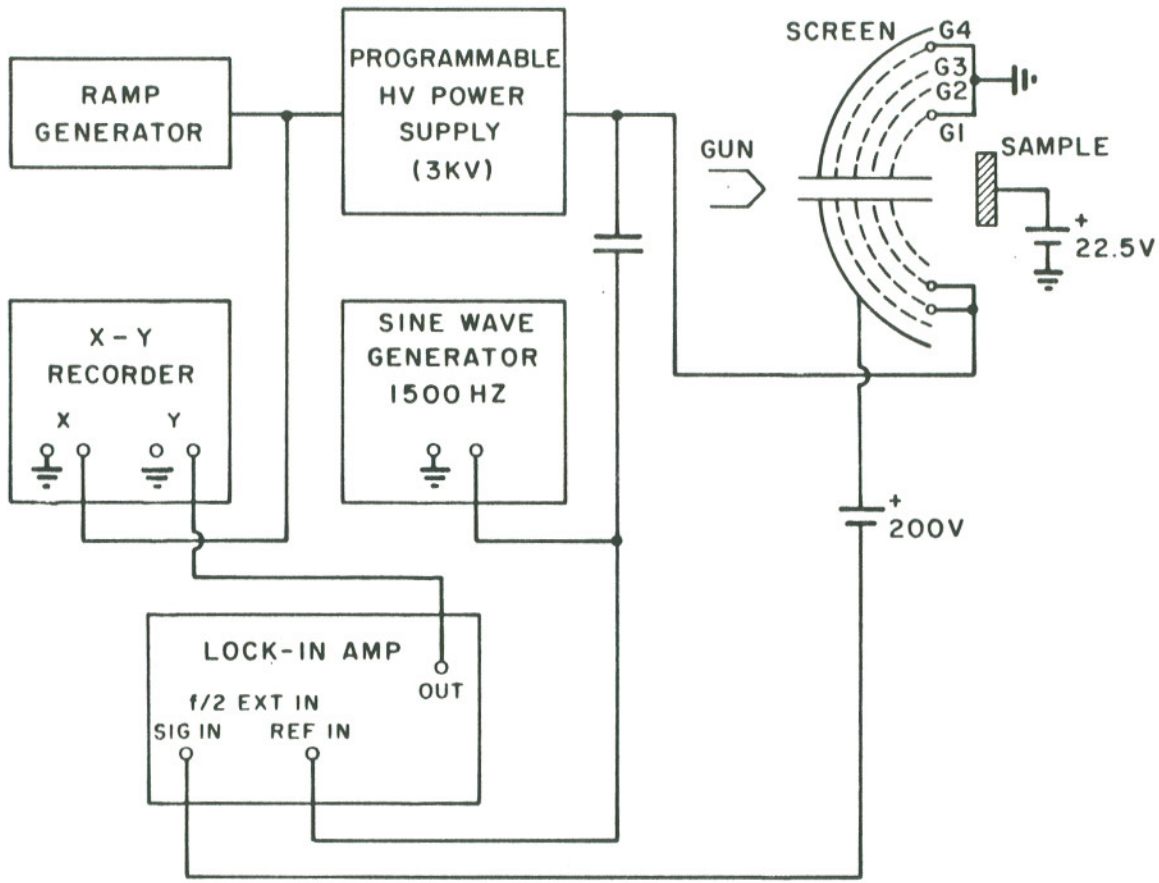

Figure 12. Schematic diagram of Auger measurement circuit for 4 grid Auger-LEED retarding field analyzer.

The energy distribution N(E) is obtained by differentiation, $di(U_r)/dU_r \propto N(E)$. This operation is performed electronically.

An ac voltage $U_m \sin \omega t$ with a small amplitude U_m is superimposed on the retarding potential U_r. The collector current can then be expressed as

$$i(U_r + U_m \sin \omega t) = i(U_r) + i'(U_r)\, U_m \sin \omega t + i''(U_r) U_m^2 \sin^2 \omega t + \ldots \quad (7)$$

The amplitude of the signal appearing with frequency ω is proportional to $i'(U_r)$ and hence proportional to N(E). The component can be selected using a lock-in amplifier. The Auger spectra usually take the form of small relatively sharp peaks on a slowly varying background which can be considerably reduced by a second differentiation.[32] The Taylor expansion of $i(U_r + U_m \sin \omega t)$ contains a component with frequency 2ω whose amplitude is given by

$$A(2\omega) = \frac{U_m}{4}\, i''(U_r) + \frac{U_m}{48}\, i'''' (U_r) + \ldots \quad (8)$$

If U_m is not too large the desired second derivative of $i(U_r)$ is proportional to $A(2\omega)$ and also in turn to $\frac{dN(E)}{dE}$. Experimentally $A(2\omega)$ is recorded by tuning the phase-sensitive detector to 2ω. The complete spectrum can be obtained by applying a ramp-type function to the retarding grid and adjusting the ramp to sweep the desired range of retarding voltage. Flexibility for setting the ramp parameters such as starting point, end point, slope and direction are provided by the function generator. The output of the function generator is used to drive a programmable power supply to produce

appropriate retarding potentials. Typical values are $0 \leq U_r \leq 1500$ volts. In this experiment, the primary beam energy was 2000 eV with 18 μA beam current. Modulation amplitudes U_m of 4V peak-to-peak (Vpp) for the Zr(147 eV), W(169/179 eV) and O(510 eV) and of 5.2 Vpp for the O (510 eV) and Cs (563/575 eV) peaks were used.

3.3.c. Energy Measurement

A retarding potential analyzer establishes a potential energy threshold which separates lower energy electrons, by reflection, from higher energy electrons which are transmitted through the retarding grid. At the threshold energy we may equate the kinetic energy of an electron, E, plus the work function of the specimen, ϕ_s, with the potential of the retarding grid, U_r, plus the work function of the retarding grid, $E + \phi_s = U_r + \phi_R$. Thus the kinetic energy of an electron is obtained from the retarding voltage by adding a correction term consisting of the difference of the two work functions. Most work function values fall in the range $\sim$ 2.5 to 5.5 eV and their difference is a correction that can be ignored.

3.3.d. Limitations

Several errors are inherent in the simple quantitative technique of determining the relationship between the Auger electron signal and atomic concentration by comparing the signal from the specimen with that from a standard. These are:

1. Matrix effects on electron escape depths and backscattering factors;

2. Chemical effects on peak shapes; and

3. Surface topography.

In this study, an electropolished W(100) sample was used, so matrix and topological effects can be ignored. Changes of the Auger peak shapes for the various elements studied here have not been observed. The backscattering factor correction has not been made since only relative coverage of surface monolayers are of main interest.

3.4. LEED

In LEED experiments a monoenergetic beam of electrons is directed towards the surface of a crystal and those electrons which are elastically scattered (and diffracted) in the backward direction are observed. Typically the energy of the primary electrons is in the region 10-300 eV and the corresponding wavelength given by the de Broglie relation $\lambda = h/p \approx \sqrt{150/V}$ Å is of the order of 1 Å. At this energy both the inelastic and elastic scattering cross sections are large; penetration without energy loss is limited to a few atomic layers and as a consequence it is only these layers which provide the elastic component of the back-scattered electrons. Compared to other diffraction methods, LEED is thus ideally suited for surface studies.

3.4.a. Theory

In diffraction experiments the angular distribution of the elastic electrons scattered from the surface is observed. If the surface atoms are arranged in a perfect periodic lattice, the surface will act as a two-dimensional grating and the interaction will produce a set of discrete diffracted beams.[32] The directions of the beams can be found from kinematical diffraction theory, as shown in Figure 13 for a 1D array of identical scatterers. The waves originating on neighboring atoms will interfere constructively if the rays depicted in Figure 13 have path lengths differing by a multiple of the wavelength. Thus, for an angle of incidence ψ_0, diffraction occurs at angles ψ given by

$$a(\sin\psi_0 - \sin\psi) = n\lambda = n\sqrt{150/V} \qquad (9)$$

where a is the distance between the scatterers and n is an integer which determines the order of diffraction. The diffraction from a 2D grating can be treated in the same way, but a more convenient procedure is to make use of the Ewald sphere construction in reciprocal space. As an illustration, consider the (100) surface of a simple cubic crystal with lattice parameter a. Associated with the bulk crystal is a reciprocal lattice which also is a simple cubic crystal but has lattice parameter $a^* = 1/a$. If we now imagine that the distance between (100) planes is gradually increased, the corresponding distances in reciprocal space are decreased and when the (100) planes

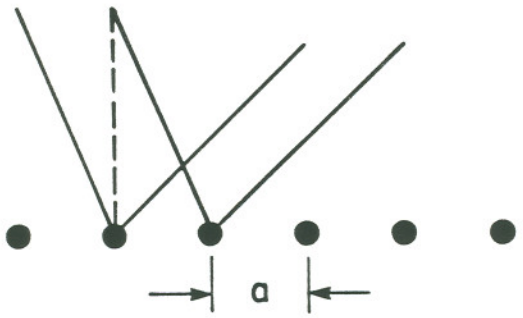

Figure 13. Geometrical construction of the diffraction condition.

are infinitely far apart, so that only a single layer remains, the reciprocal lattice points have merged into a set of parallel "rods" which pass through the lattice points of the reciprocal net (Figure 14). The primary beam is represented by a plane wave exp. $(i\vec{k}^\circ \cdot \vec{r})$ where the propagation vector $\vec{k}^\circ$ has magnitude $|\vec{k}^\circ| = 2\pi/\lambda$ and components $\vec{k}^\circ_{||}$ and $\vec{k}^\circ_{\perp}$ parallel and perpendicular to the surface, respectively. The Ewald sphere is drawn such that $(1/2\ \pi)\vec{k}^\circ$ is a radius-vector which terminates at the origin of the reciprocal net. The intersections of the lattice rods with the sphere determines the possible angles of diffraction; for example $\overrightarrow{AC}$ is equal to $(1/2\ \pi)\vec{k}'$, where $\vec{k}'$ is the propagation vector of one of the diffracted beams. It is seen that, in general,

$$k^\circ = k' \text{ (conservation of energy)} \tag{10}$$

and

$$\vec{k}'_{||} = \vec{k}^\circ_{||} + 2\pi\ \vec{U} \text{ (conservation of parallel momentum)} \tag{11}$$

where $\vec{U}$ is a reciprocal net vector. For the beams shown in Figure 14, equation (11) can be written

$$(1/\lambda)\ \sin\psi = (1/\lambda)\ \sin\psi_0 + h(1/a) \tag{12}$$

which is the same as the plane grating formula. In the diagram of Figure 14, $1/\lambda$ is of the same order of magnitude as $1/a$ and only a few diffracted beams can occur, as is typical in LEED. In a display apparatus the beams will appear as spots on the screen and for normal

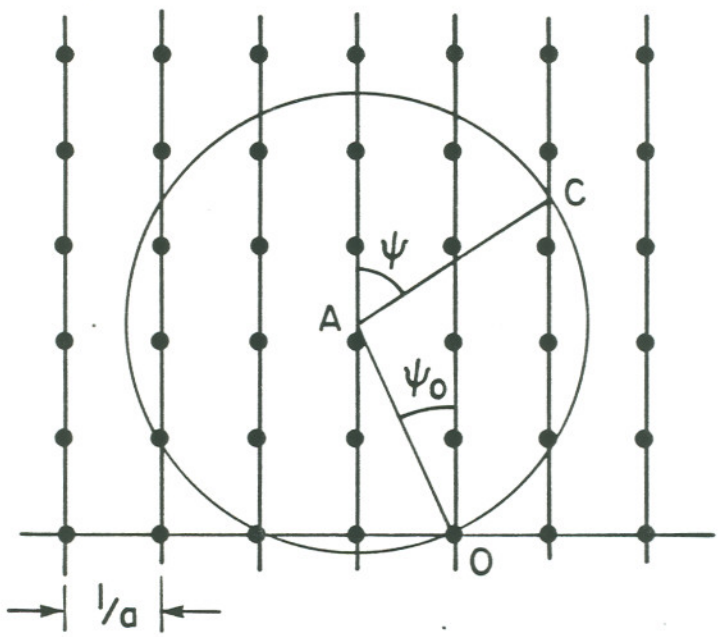

Figure 14. Ewald sphere diagram for a simple cubic lattice. The radius of the sphere is $1/\lambda$. $\vec{AO} = (\frac{1}{2\pi})\ \vec{K}^{\circ}$ represents the primary beam. $\vec{AC} = (\frac{1}{2\pi})\ \vec{K}'$ represents one of the possible diffracted beams.

incidence the resulting diffraction pattern provides an image of the reciprocal net.

3.4.b. Experimental Set-Up

Most of the LEED systems presently in use and all types which are commercially available are of the "display-type" (Figure 15). Electrons leave the drift tube of the electron gun with the desired energy E and strike the sample surface. Normal incidence is employed. The first grid and the crystal are grounded so that scattered electrons are not deflected electrostatically in the field free region between sample and the first grid. The addition of Helmholtz coils around the LEED chamber may be necessary in order to avoid magnetic disturbances, e.g., by the earth's field. The second grid is at a negative potential whose magnitude is slightly smaller than the primary electron energy E and therefore repels the inelastically scattered electrons. The addition of a third grid at the same potential as the second (repeller) grid will reduce field inhomogeneities caused by the finite size of the mesh. A fourth grid is mounted between repeller and collector to reduce the capacitance between them and prevent any AC modulating voltage applied to the repeller from being passed on to the collector directly. After passing the grids the elastically scattered electrons are accelerated onto a fluorescent screen by a positive potential of a few kilovolts. The screen will display diffraction spots at the

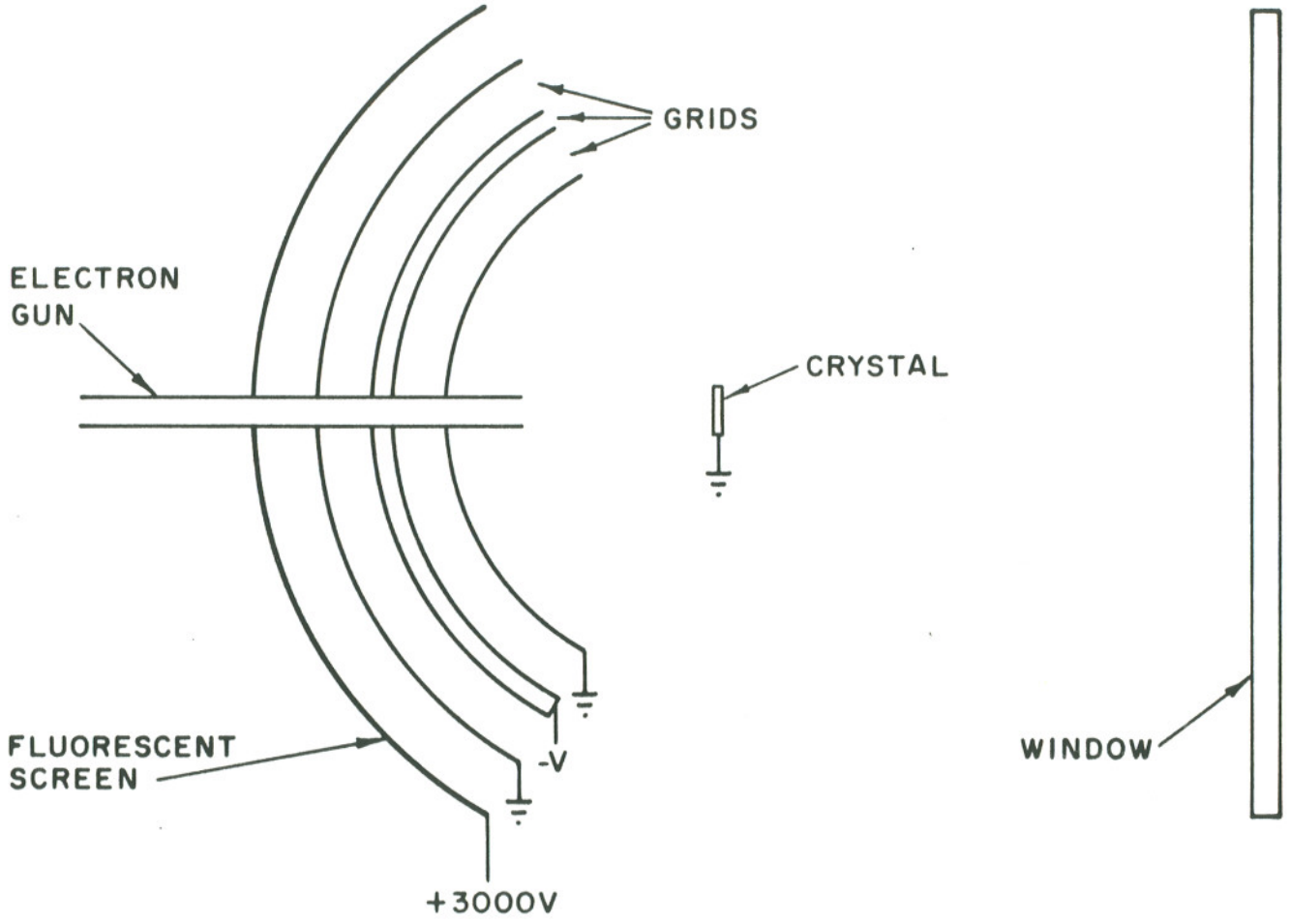

Figure 15. Schematic diagram of the LEED system.

positions of the interference maxima. The diffraction pattern may be observed visually through a window in the vacuum chamber. A permanent record is made by photographing the display.

3.4.c. Analysis of Diffraction Pattern

A sketch of a diffraction pattern for oxygen on W(100) is shown in Figure 16. The "extra spots" caused by the adsorbed surface structure are marked differently.[33] The substrate diffraction spots have been indexed using the common nomenclature which automatically yields the reciprocal substrate unit vectors $\vec{a}_1^*$ and $\vec{a}_2^*$. Every point on the reciprocal lattice of the surface structure can be reached by translation operations in terms of the basis vectors $\vec{b}_1^*$ and $\vec{b}_2^*$. These are inter-related with the reciprocal unit vectors of the substrate by the relations

$$\vec{b}_1^* = 1/2\ \vec{a}_1^* + 1/2\ \vec{a}_2^* = m_{11}^*\ \vec{a}_1^* + m_{12}^*\ \vec{a}_2^* \qquad |\vec{a}_1^*| = |\vec{a}_2^*|$$

$$\vec{b}_2^* = 1/2\ \vec{a}_1^* - 1/2\ \vec{a}_2^* = m_{21}^*\ \vec{a}_1^* + m_{22}^*\ \vec{a}_2^* \qquad (13)$$

Next, the substrate lattice is constructed from the position of the substrate diffraction spots: $\vec{a}_1$ is perpendicular to $\vec{a}_2^*$ and has the length $|\vec{a}_1| = \dfrac{1}{|a_2^*| \sin r^*} = \dfrac{1}{|\vec{a}_1^*|}$ where r^* is the angle between $\vec{a}_1^*$ and $\vec{a}_2^*$. Similarly $\vec{a}_2 \perp \vec{a}_1^*$ and has the length

$$|\vec{a}_2| = \frac{1}{|\vec{a}_2^*|} = \frac{1}{|a_1^*|} = |\vec{a}_1|$$

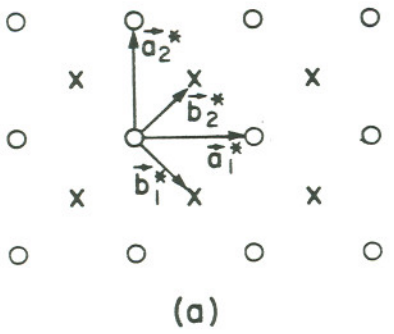

(a)

c(2x2) LEED PATTERN
O on W(100)

O substrate spots

X adsorbate spots

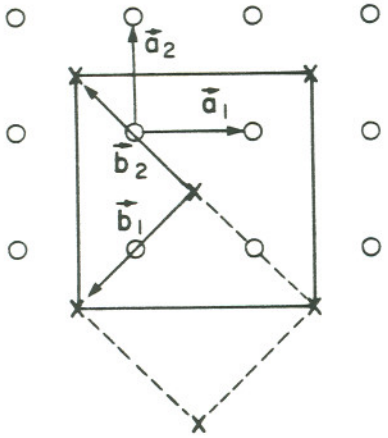

(b)

REAL LATTICE

O substrate atoms

X adsorbate atoms

Figure 16. Analysis of a simple LEED diffraction pattern.

a) Reciprocal lattice (diagram of observed LEED pattern.)

b) Real lattice of the substrate and adsorbate.

The real lattice of the surface structure

$$\vec{b}_1 = m_{11}\,\vec{a}_1 + m_{12}\,\vec{a}_2$$
$$\vec{b}_2 = m_{21}\,\vec{a}_1 + m_{22}\,\vec{a}_2 \qquad (14)$$

is derived using the relations

$$m_{11} = \frac{1}{\det m^*}\, m_{22}^* = -1$$
$$m_{12} = -\frac{1}{\det m^*}\, m_{21}^* = -1 \qquad (15)$$
$$m_{21} = -\frac{1}{\det m^*}\, m_{21}^* = -1$$
$$m_{22} = \frac{1}{\det m^*}\, m_{11}^* = 1$$

yielding $\vec{b}_1 = -\vec{a}_1 - \vec{a}_2$

$\vec{b}_2 = -\vec{a}_1 - \vec{a}_2$

3.5. Thermal Desorption Mass Spectrometry (TDS)

3.5.a. Theory

Methods of analyzing the desorption spectra have been described by Smith,[34] Ehrlich[35] and Redhead[36] and others. Here only one heating schedule is considered: a linear variation of sample temperature with time ($T = T_o + \beta t$). The rate of desorption from unit surface area may be written as

$$N(t) = -\frac{d\sigma}{dt} = \upsilon_n \sigma^n \exp(-E/kT) \tag{16}$$

where n is the order of the desorption reaction, σ is the surface coverage (molecules/cm) υ_n is the rate constant, and E is the activation energy of desorption (eV/atom), which is assumed to be independent of σ. If equation (16) is solved to find the temperature (T_p) at which the desorption rate is a maximum, then

$$E/kT_p^2 = (\upsilon_1/\beta) \exp(-E/kT_p) \text{ for } n = 1. \tag{17}$$

$$E/kT_p^2 = (2\sigma_p \upsilon_2/\beta) \exp(-E/kT_p) \quad \text{for } n = 2 \tag{18}$$
$$= \sigma_o \upsilon_2/\beta \exp(-E/kT_p)$$

where σ_o is the initial surface coverage and σ_p is the coverage at $T = T_p$.

Equation (17) shows that T_p is independent of coverage for a first order reaction and, thus, E can be found directly from a measurement of T_p provided a value of υ_1 is assumed. The relation between E and T_p is very nearly linear and, for $10^{13} > \upsilon_1/\beta > 10^8$ K^{-1} is given to ± 1.5 percent by[36]

$$E/kT_p = \ln(\upsilon_1 T_p/\beta) - 3.64. \tag{19}$$

For the second-order case, it can be shown from equation (18) that T_p depends on the initial surface coverage

$$\ln^k \frac{\upsilon_2}{E\beta} + \ln \sigma_o T_p^2 = E/kT_p . \tag{20}$$

From the area under the curve of desorption rate as a function of time one may obtain σ_o . When $\ell n(\sigma_o T_p^2)$ is plotted against $1/T_p$, a straight line is obtained of slope E/k. Thus, the order of the desorption reaction can be determined from the behavior of the maximum in the desorption rate curves with coverage. A first-order reaction gives rise to a peak in the desorption rate curve where T_p is independent of σ_o. If T_p decreases with increasing coverage, the reaction may be either second-order, or first-order with an activation energy dependent on coverage. These two cases can be distinguished by plotting $\ell n(\sigma_o T_p^2)$ against $1/T_p$; as noted above, a second order reaction with fixed activation energy yields a straight line.

3.5.b. Experimental Set-Up

An EAI Quad 160 Mass Analyzer (QMA) was used in this study. Its performance is based upon the quadrupole theory of ion analysis. The analyzer consists of a filter rod assembly, ionizer, and an electron multiplier detector (Figure 17). The ionizer filament produces a beam of electrons which can be precisely controlled. Molecules or atoms of gases which pass through the electron beam undergo electron bombardment. If the energy of the bombarding electrons is sufficient, some of the molecules or atoms will lose an electron to form positively charged ions. Also, some of the molecules will undergo dissociation or fragmentation resulting in the formation of positive

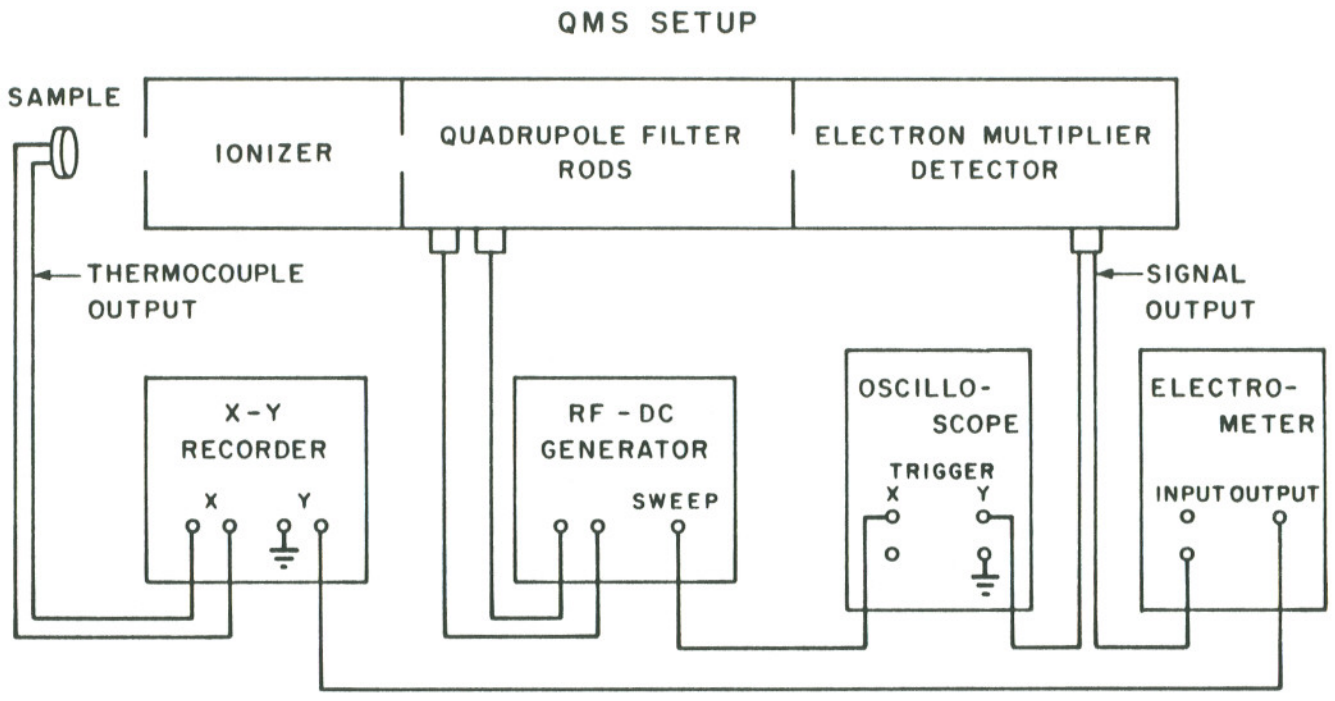

Figure 17. Thermal desorption mass spectrometry schematic diagram. For simplicity, the sample heater is not shown. The oscilloscope was used primarily for leak checking with He; measurements were made using the electrometer/ recorder.

ions. Direction and velocity of the positive ions are controlled by the focus and exit lenses which guide the ions into the quadrupole filter rod assembly.

The quadrupole filter rod assembly functions as an ion selector or mass filter by allowing only ions of a certain m/e ratio to traverse the entire length of the rods. A DC voltage with superimposed RF voltage is applied to opposite pairs of the rods, one pair being at a negative potential and the other pair at a positive potential. The voltage is applied in a sawtooth sweep and ions pass through the filter in order of increasing mass number as the voltage is swept from low to high potentials. Ions which are successful in passing through the filter impinge upon the first dynode of the electron multiplier. The proper channeling of this signal will produce a mass spectrum on an oscilloscope or recorder.

3.5.c. Method

In this study, the QMA was used to monitor the background gases and to measure neutral Cs and Cs^+ ion desorption. The typical laboratory set-up for these measurements is shown in Figure 17. For background gas analysis, the sweep output of the QMA was connected to the oscilloscope external horizontal input, so the full spectrum of the system residual gases are displayed. In the neutral Cs desorption spectrum, the output of the electron multiplier detector was amplified and fed to the vertical axis of the X-Y recorder, and

the Cs peak is monitored continuously (no sweep). A retarding field of ~ 20 V/cm was used to prevent Cs^+ ion emission from the sample, so that only neutral desorbed Cs entered the QMA.

The sample was heated to 1300 K in 35 sec. Due to nonlinear heating, the heating rate dropped from 51 K/sec to 20 K/sec during this heating interval. This nonlinear heating rate was considered in Cs desorption versus coverage and binding energy determinations by dividing the desorption rate at each instant by its corresponding heating rate. In TDS, the thermocouple reading of the sample temperature during heating was displayed on the horizontal input of the X-Y recorder, yielding the full Cs desorption spectrum. For Cs^+ ion desorption, the TDS was measured by turning off the filament in the ionizer so that only the Cs^+ ions desorbed from the surface could reach the detector.

3.6. Electron Reflection

3.6.a. Theory

The low energy electron reflections (LEER) caused by Bragg interference effects of electrons incident on the sample surface was used in this study.[37] The kinematic model is the simplest approximation model for electron interactions with a lattice and gives rise to the Bragg reflection conditions. Figure 19 is a simplified energy-level diagram of a metal surface which is used as a target for incident low energy electrons, with the work function ϕ_c as shown.

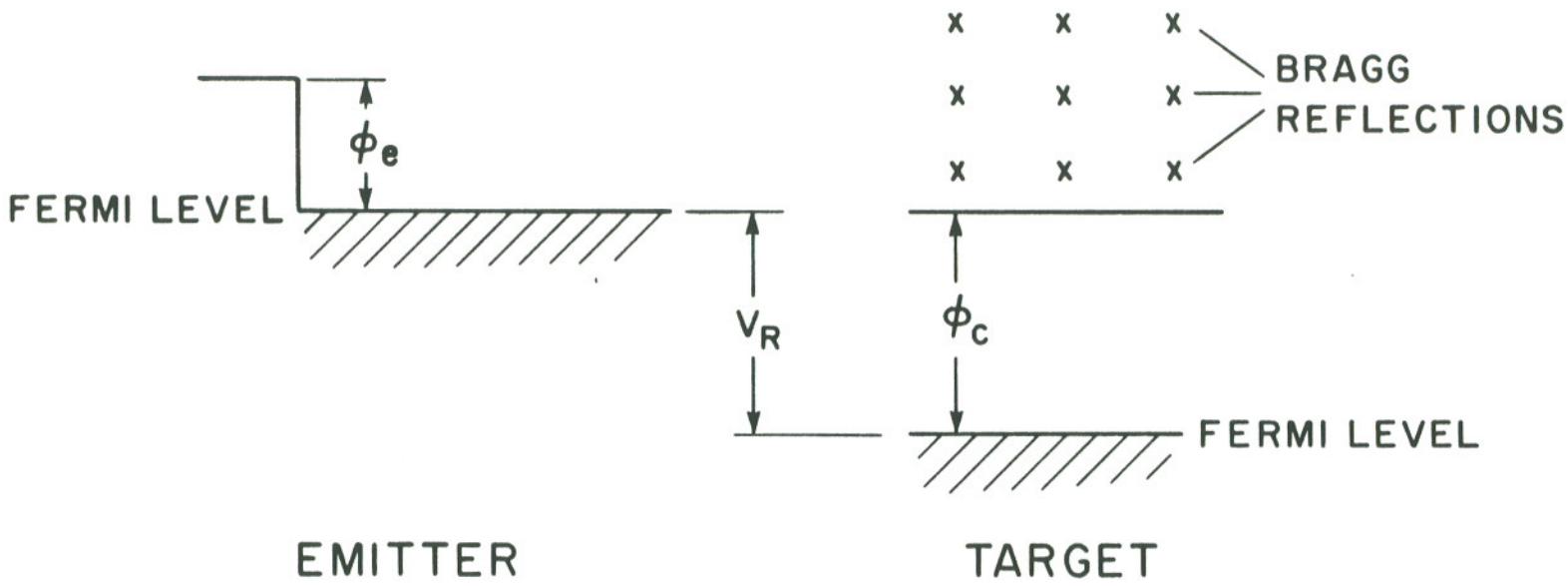

Figure 18. Simplified energy-level diagram of a metal surface which is used as a target for incident low energy electrons.

If the metal is a single crystal of lattice spacing d, then unallowed energy states will exist above the Fermi level where the Bragg condition $n\lambda = 2d$ exists. If this condition can be expressed in terms of the free-electron kinetic energy, then this results in the well-known simplified relation for the energies of the Bragg reflections

$$\epsilon = (37/d^2)n^2 \ , \tag{21}$$

where ϵ is the kinetic energy of the electrons in eV and d is the lattice spacing in Å. These reflections should be visible as minima in the current collected by the collector (target) for incident electron energies corresponding to the unallowed energy states. Such incident electrons can be provided from an emitter whose vacuum level is changed with respect to the target by means of applying a voltage V_R between the emitter and target. Figure 19 shows the collected current which might be expected when plotted as a function of the energy above the Fermi level of the metal target. The minima in the deviations (E↓) correspond to the position of the reflections given in Eq. (21). The deviation maxima (E↑) are similarly expressed.

$$\begin{aligned} E\downarrow &= (37/d^2)n^2 \\ E\uparrow &= (37/d^2)(n-1/2)^2 \end{aligned} \tag{22}$$

One property of the collector that can detract in the accuracy of determining ϕ_c is electron reflection near the threshold of

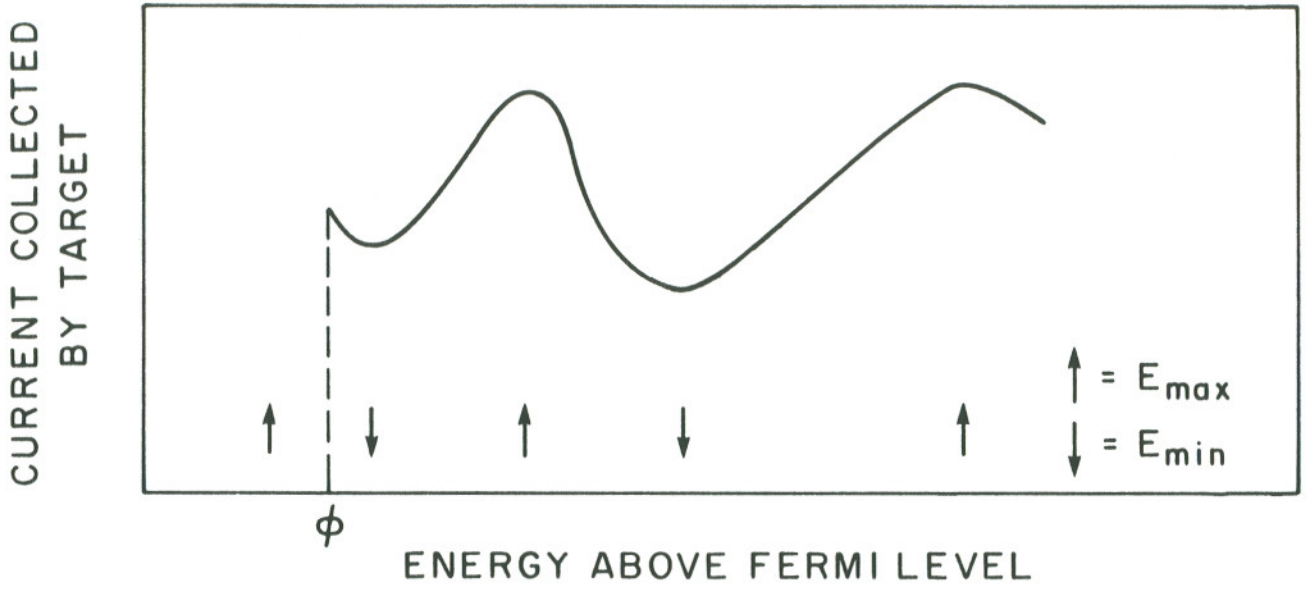

Figure 19. Plot of collected current in the retarding-to-accelerating region, showing the appearance of maxima ($E_{max} = \frac{37}{d^2} (n - 1/2)^2$ and minima ($E_{min} = \frac{37}{d^2} n^2$) caused by Braff reflections.

collection. The effect of reflection can be shown as $I_c = I_p(1 - R)$, where I_p is the primary beam current impinging on the collector, and by defining the energy dependent reflection coefficient $R(\epsilon)$ as

$$R(\epsilon) = I_r/I_p \tag{23}$$

where I_r is the reflected current.

3.6.b. Experimental

The measurement is done by the FERP gun. The I-V data are taken from the collector voltage $V_c = 0$ to $V_c = 20$ V. Figure 20 is a diagram showing the set-up for the electron reflection measurement. I_p' is the emitter current arriving at the mesh. Noting that the transmission is given by $I_p/I_p' = T$ and R is given by $R=I_r/I_p = (I_p - I_c)/I_p = 1 - I_c/I_p$ one can show that

$$R = 1 - I_c/T(I_s + I_c) \tag{24}$$

A higher I_c collected at the sample means the electron reflection is lower. I_s is the screen current.

The total reflected current may be further subdivided into an elastic and an inelastic part $I_r = I_{elastic} + I_{inelastic}$. The magnitude of I_r will depend on V_s (s refers to the screen mesh electrode). In this experimental set-up when $V_c \pm \phi_c > V_s \pm \phi_s$ those reflected electrons which lose a small amount of energy through inelastic processes will not be collected at the screen but instead will be returned to the collector, so mainly specularly reflected

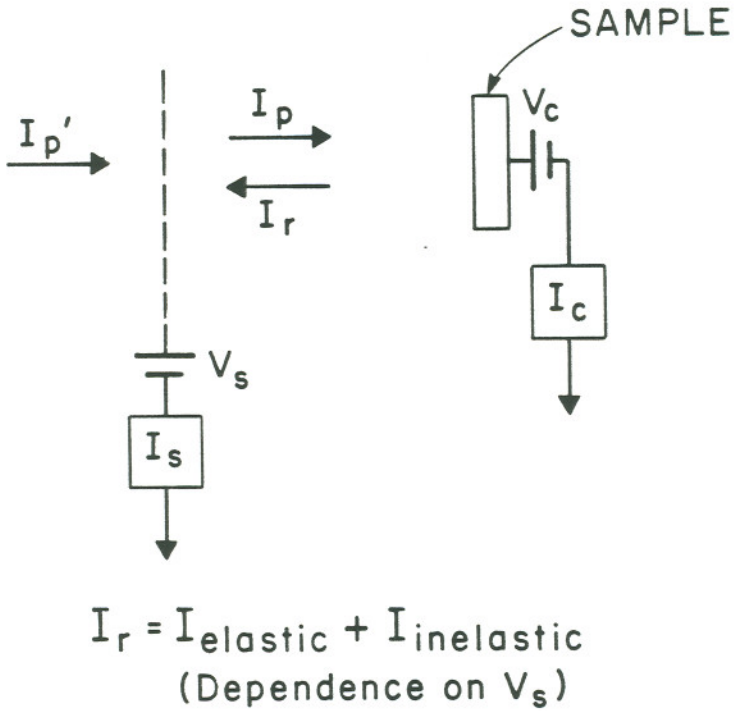

Figure 20. Schematic of electron reflection measurement setup. $I_r = I_{elastic} + I_{inelastic}$ (depends on V_s); I_p = incident current at sample; I_s = screen current; I_c = collected sample current.

elastically scattered electrons will escape from the collector crystal. The elastically reflected electron coefficient R_e can thus be measured. On the other hand, when $V_c \pm \phi_c < V_s \pm \phi_s$, all reflected electrons in the energy range investigated return to the screen and the total reflection R_e curve is obtained. Hence, it is possible by this technique to measure the inelastically reflected electron coefficient R_{in} by noting that $R_{in} = R_t - R_e$.[29] The screen voltage in the FERP gun was biased around + 20 eV in this study, thus allowing R_t to be determined from Eq. (23).

CHAPTER 4

RESULTS

4.1. Z/O/W(100) Low Work Function Surface

4.1.a. Auger Measurements

During the period of this project, the Zr/O/W(100) low work function surface was prepared and measured many times. The various Zr/W and Zr/O Auger amplitude ratios and corresponding work functions of these surfaces are listed in Table II and plotted in Figure 21. From the points on the graph, the following con clusions can be drawn:

1. The lowest work function is 2.6 eV.

2. The majority of low work function measurements fall between 2.7 and 2.75 eV.

3. The Zr/W and Zr/O Auger amplitude ratios are in the ranges 0.7-0.9 and 0.88-1.2 respectively, for most of the low work function surfaces measured.

4. The higher work function surfaces exhibited higher oxygen concentrations relative to the lower work function surfaces.

5. The Zr/W and Zr/O ratios were measured some time after a high temperature flash for cases C and F. The residual gases in the system caused the work function to increase, in agreement with conclusion 4.

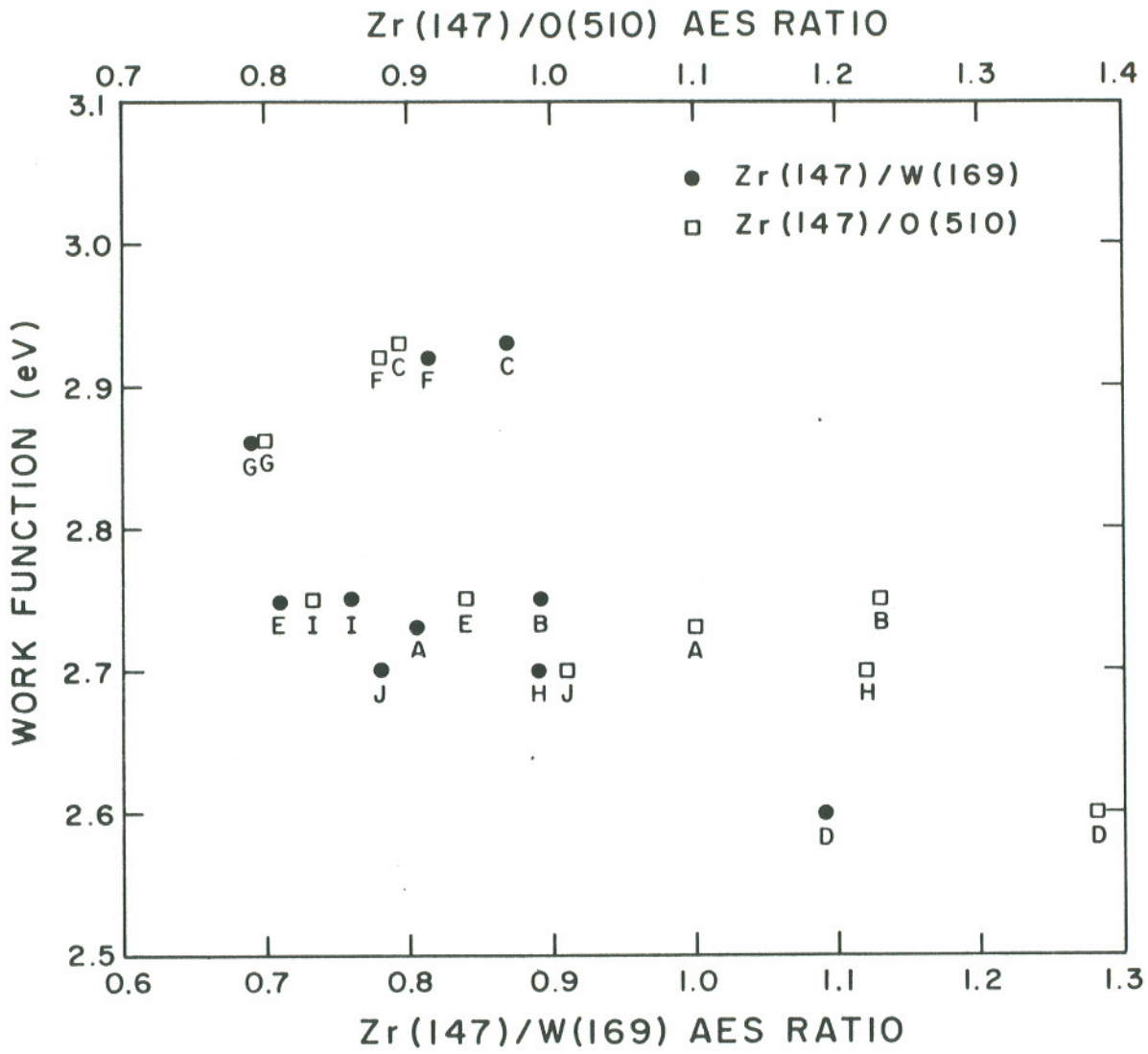

Figure 21. Zr/W and Zr/O Auger amplitude ratios observed on the Zr/O/W(100) surface at various times during the period of this project.

TABLE II

THE VARIOUS Zr/W(100) AND Zr/O AUGER AMPLITUDE RATIOS ON THE Zr/O/W(100) LOW WORK FUNCTION SURFACES WHICH WERE PREPARED DURING THIS PROJECT

	Work Function (eV)	Zr(147)/W(169) AES RATIO	Zr(147)/O(510) AES RATIO
A	2.73	0.805	1.10
B	2.75	0.892	1.23
C	2.93	0.870	0.893
D	2.60	1.09	1.38
E	2.75	0.712	0.939
F	2.92	0.815	0.877
G	2.86	0.688	0.793
H	2.70	0.887	1.218
I	2.75	0.867	0.822
J	2.70	0.78	1.01

The reason for the variation in the Zr/O/W(100) work functions is mainly due to slightly different Zr doses in the initial sample preparation. The subsequent Cs adsorption experiments were performed on these low work function surfaces where $2.6 \leqslant \phi \leqslant 2.75$, therefore, the Zr, O, and W concentrations of these surfaces were slightly different.

L.R. Danielson[38] has done a more detailed study of the low work function Zr/O/W(100) surface by varying the O and Zr coverages systematically. He showed that the work function varies between 2.9 and 2.7 eV when the Zr/W Auger ratios are in the range 0.65-1.0 (Figure 22). This result is in good agreement with Figure 21. Figure 22 also shows that Zr/O Auger ratios are in the range 0.32-0.5 when the work function varies between 2.9 and 2.7 eV, but in Figure 21, the Zr/O ratio is between 0.79 ~ 1.23. The difference is probably due to the different measurement apparatus, one being a cylindrical mirror analyzer (CMA) and the other a retarding field analyzer (RFA). In the RFA, the sensitivity to higher energy Auger electrons (oxygen) is very low, which explains the higher Zr/O ratio in Figure 21.

4.1.b. LEED

The (1 x 1), (4/3 x 2) and $(\sqrt{5} \times \sqrt{5})$ R $\tan^{-1}$ 0.5 LEED patterns previously observed by Danielson and Swanson[1] were also observed during this study. These LEED patterns, shown in Figure 23, all correspond to Zr-O-W structures at or near the minimum work function.

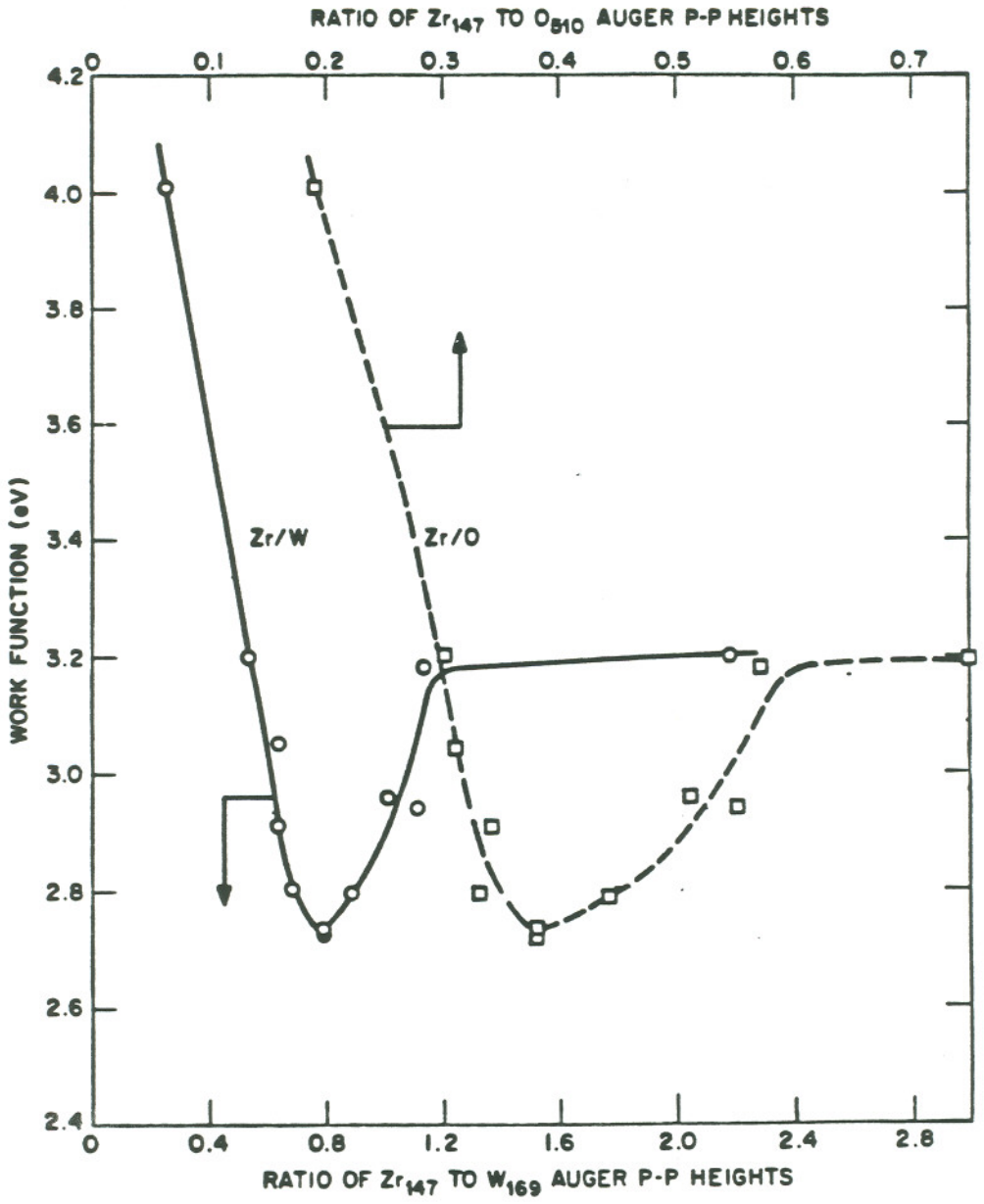

Figure 22. Work function of Zr/O/W(100) versus Zr/W and Zr/O for single crystal W(100) (Ref. 38).

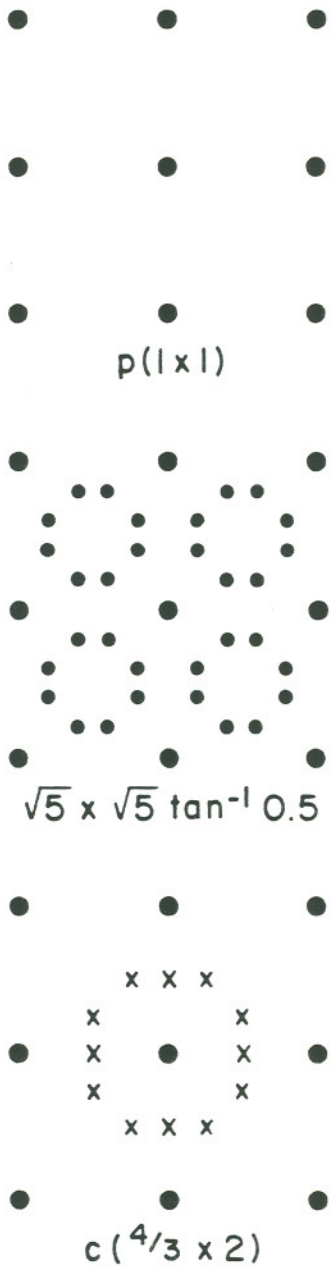

Figure 23. Three LEED patterns observed near minimum ϕ for the system Zr/O/W(100).

4.2. Cs Adsorption on Zr/O/W(100)

4.2.a. Work Function versus Cs Dose Time

The work function change with Cs adsorption on the low work function Zr/O/W(100) surface with zero excess oxygen coverage is shown in Figure 24. The minimum work function obtained is ϕ_m = 2.12 eV. This curve has a shallow minimum, reaching a saturation value 2.16 eV around 24 min. The heating current for the Cs flux was 3.8 A.

4.2.b. Work Function versus Heating Temperature

The change in work function with heating temperature of an initially Cs-saturated surface of Zr/O/W(100) is shown in Figure 25. The sample was heated for 1 min intervals to successively higher temperatures ranging from 350 K to 1000 K. The FERP work function was measured after the sample cooled below 400 K. Gradual desorption of Cs from the saturated Cs layer caused an initial lowering of work function to 2.12 eV, which is the same minimum observed from Cs adsorption on Zr/O/W(100). Further desorption of Cs increased the work function. Heating to $>$ 900 K yielded the work function of the original Zr/O/W(100) surface. These results suggest a reversible adsorption/desorption process.

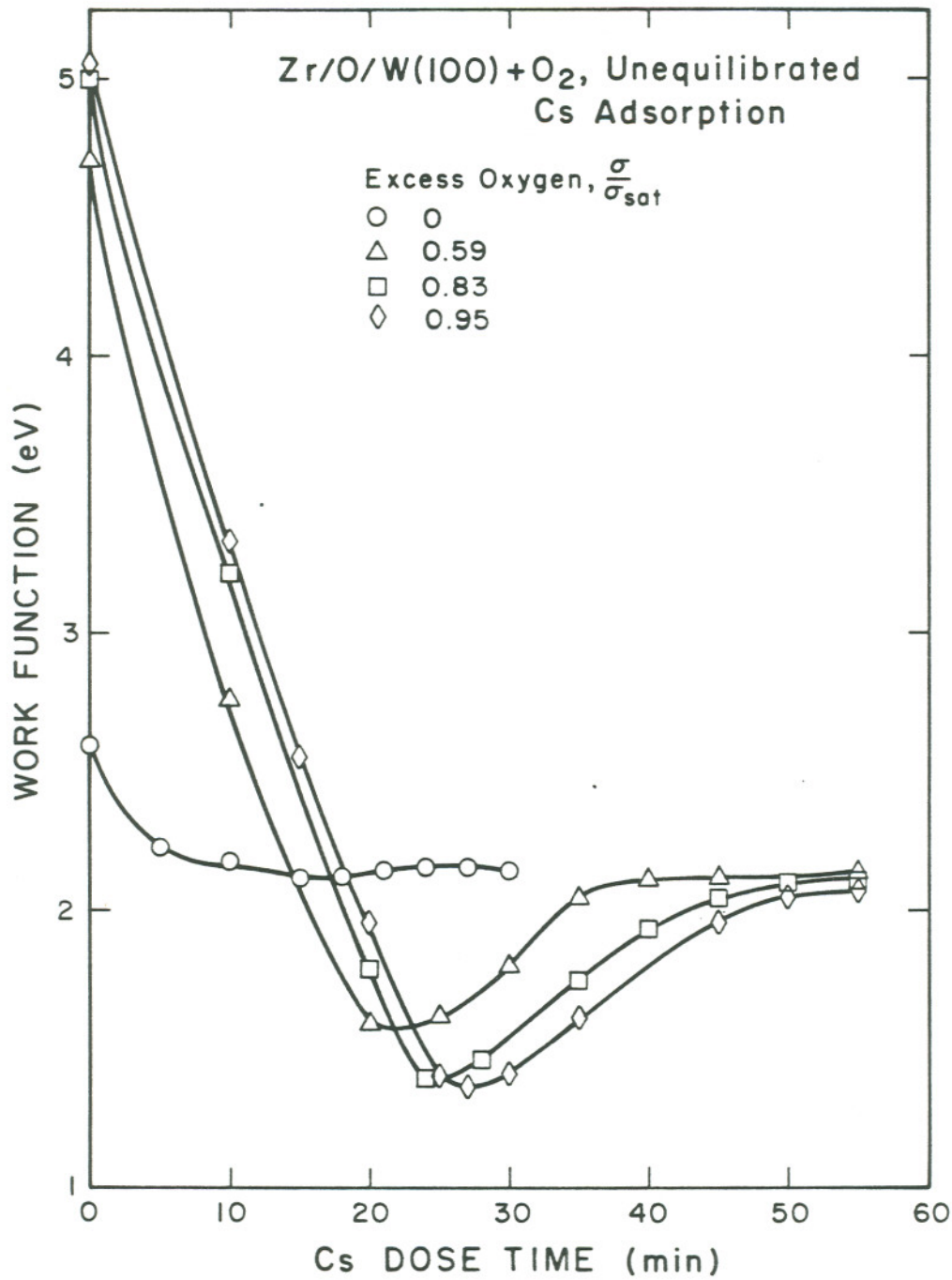

Figure 24. Work function versus dose time for Cs adsorption on Zr/O/W(100) with various unequilibrated excess O coverages. Excess O coverage based upon Auger measurements.

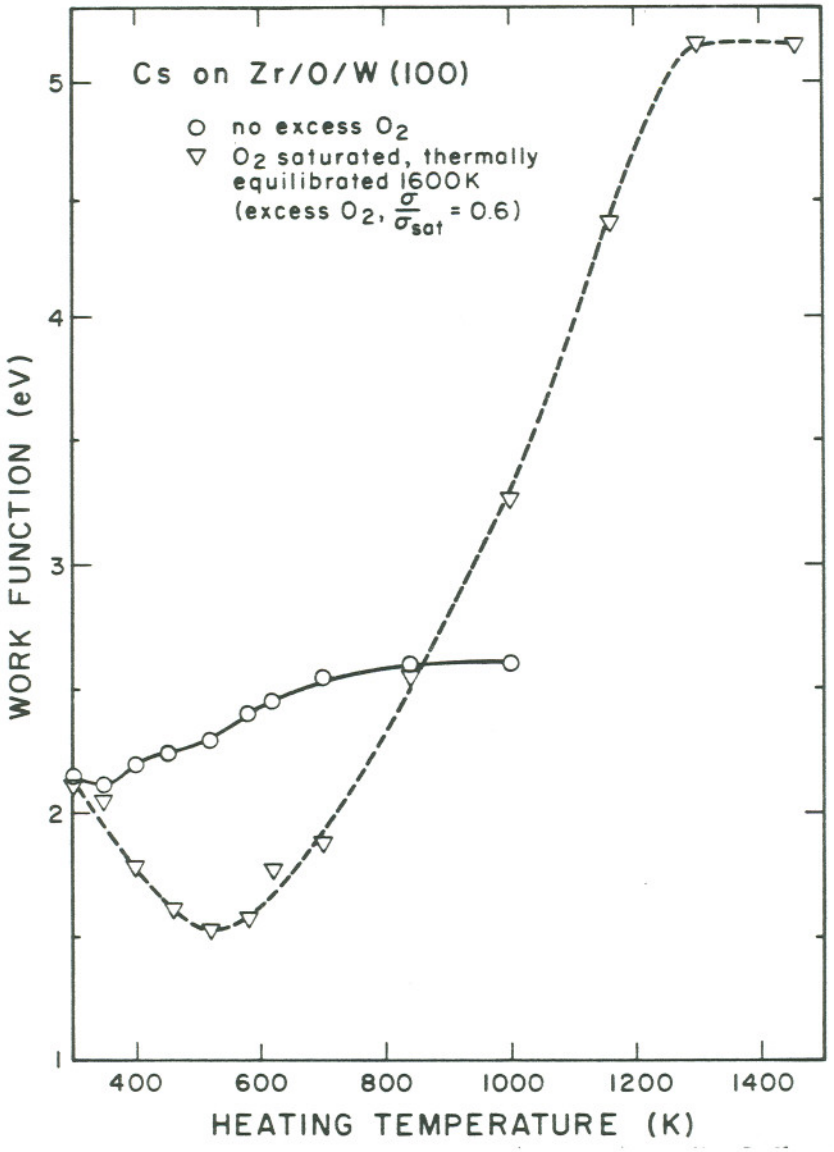

Figure 25. Work function versus desorption temperature for an initially saturated Cs layer on Zr/O/W(100) with and without a preadsorbed, thermally equilibrated O layer. FERP measurements were made at T ≤ 400 K after 1 min. heating at each indicated temperature.

4.2.c. Cs Auger Amplitude versus Cs Dose Time

Figure 26 shows the Cs and O Auger peak-to-peak amplitudes vs. Cs adsorption time. The Cs curve is linear with a break in slope around 24 min indicating, if unity sticking coefficient is assumed, that it takes 24 min to develop one monolayer Cs coverage on Zr/O/W(100) at the dose rate used in agreement with the FERP measurements of Section 4.2.a. Interestingly, the O Auger amplitude is unchanged during Cs adsorption.

4.2.d. Thermal Desorption Spectrometry of Cs

Neutral Cs desorption spectra are presented in Figure 27 as a function of the fractional Cs coverage $\theta_{Cs} = \sigma/\sigma_{sat}$. σ_{sat} is the integrated Cs TDS desorption flux for saturated Cs coverage. The amplitudes of these curves have been corrected for the nonlinear sample heating rate. The curves show that as θ_{cs} increases, the high energy desorption peak shifts slightly to lower temperature, implying that the binding energy of Cs in this state is weakly coverage dependent. Nevertheless, the desorption energies were calculated assuming first order desorption using equation 19, with the preexponential factor assumed to be $\nu_1 = 10^{13}$ sec^{-1}. The two major desorption peaks occur at 445 K and 522 K, correspond to binding energies of 1.08 eV and 1.28 eV respectively. Figure 27 also shows that Cs desorption is complete at 900 K which is consistent with the behavior of work function vs heating temperature

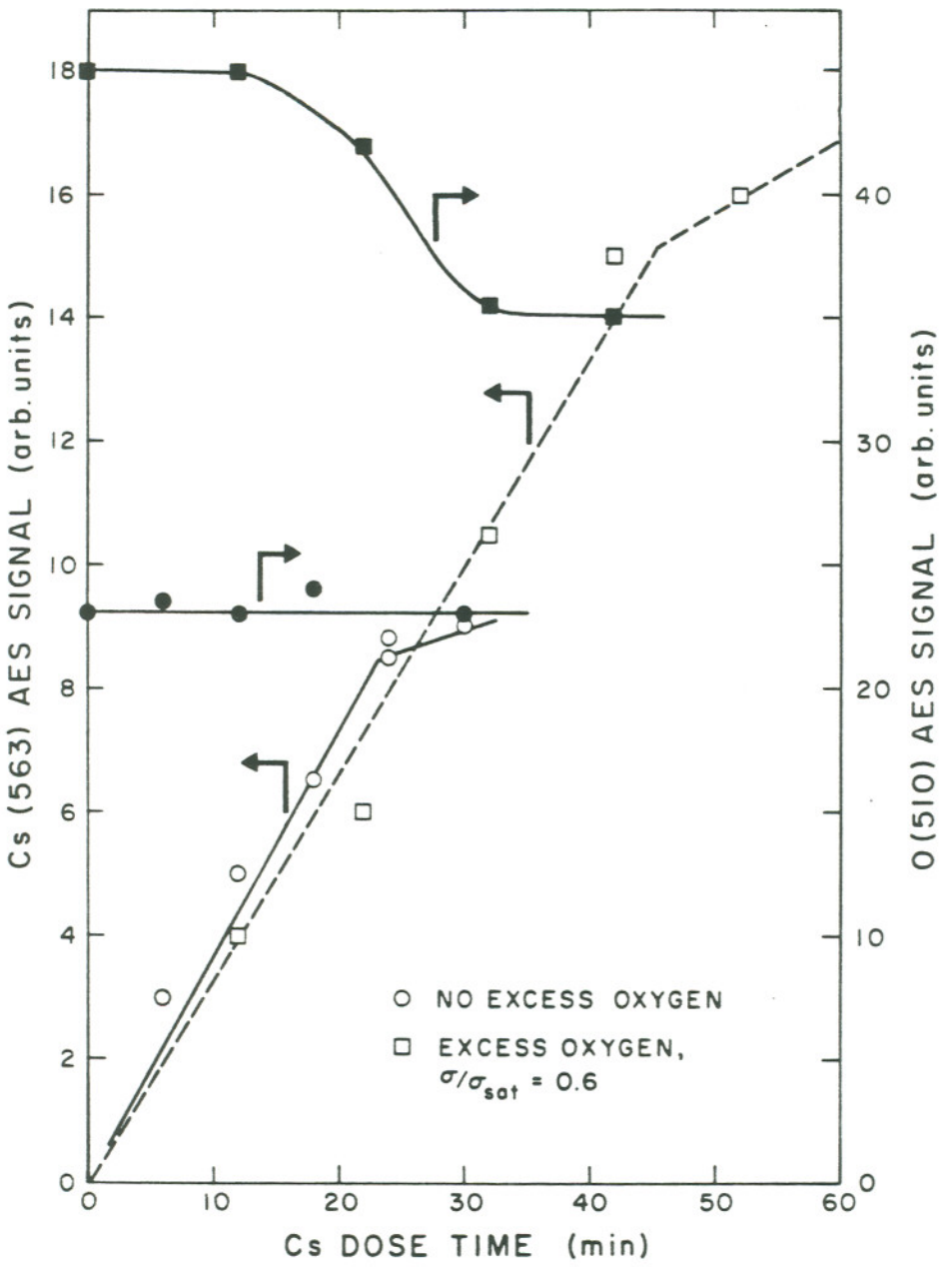

Figure 26. Cs and O Auger peak-to-peak amplitudes versus dose time for Cs adsorption on Zr/O/W(100) with and without a thermally equilibrated, preadsorbed excess O layer.

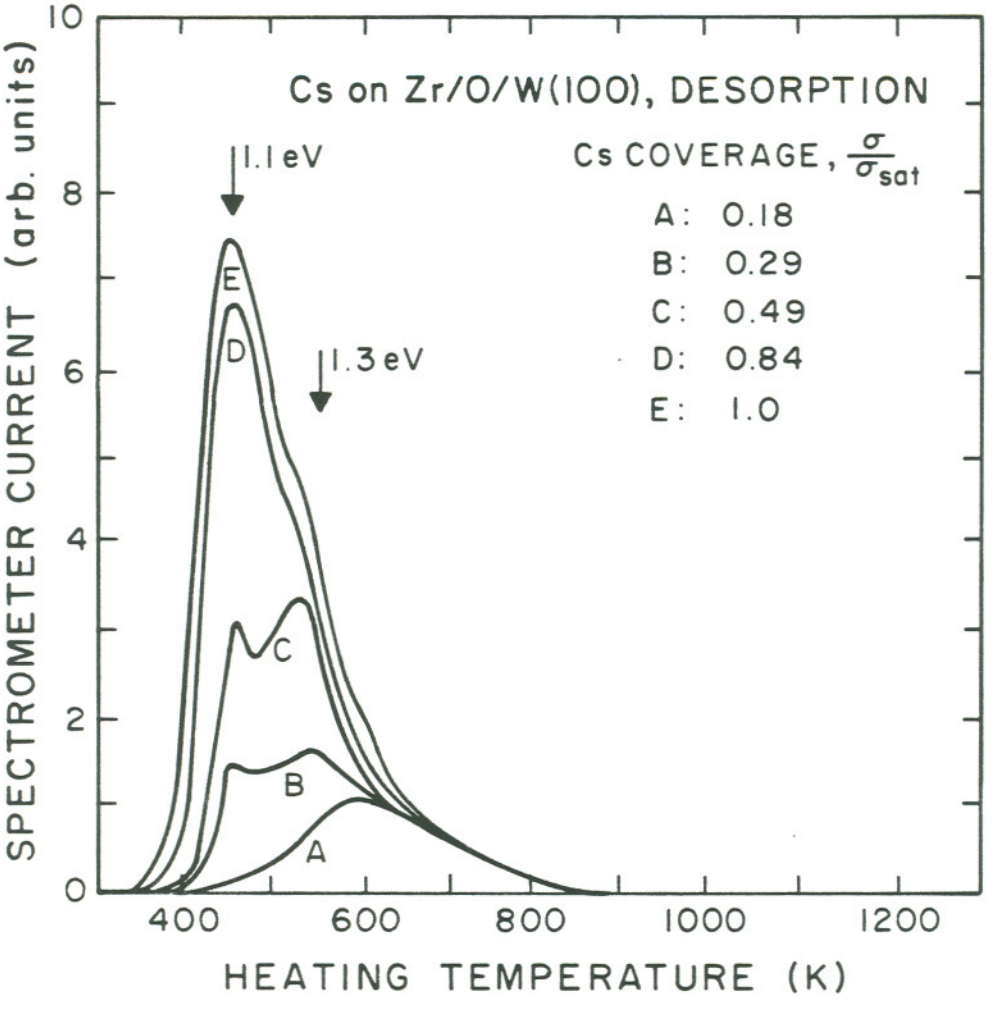

Figure 27. Thermal desorption of Cs from Zr/O/W(100) for various initial coverages.

of the initially saturated Zr/O/W(100) surface (Figure 25).

4.2.e. Low Energy Electron Reflection Measurement

The collected electron current vs electron energy for an electron beam incident upon the Zr/O/W(100) surface, with and without a saturated Cs layer, is shown in Figure 28. For the Zr/O/W(100) surface without Cs, the maxima peaks at 6.8 and 9.7 eV. For the Cs/Zr/O/W(100) surface, the absolute maximum peak occurs at 3 eV and the whole I-V curve becomes flat at higher electron energies.

4.2.f. LEED

For saturated Cs coverage on the Zr/O/W(100) surface, the LEED pattern did not change from that at zero Cs coverage except for an increase in background intensity

4.3. Adsorption of O_2 on Zr/O/W(100)

4.3.a. Work Function and O Auger Amplitude versus O_2 Dose Time

Figure 29(a) illustrates the work function and O Auger signal changes for adsorption by exposure of the Zr/O/W(100) surface to 1×10^{-8} torr O_2 at room temperature. The work function increases rapidly with O_2 exposure up to 0.6 L (1L = 1×10^{-6} torr-sec), then levels out and reaches a final value around 5.2 eV. The O Auger signal increases rapidly in the initial exposure range

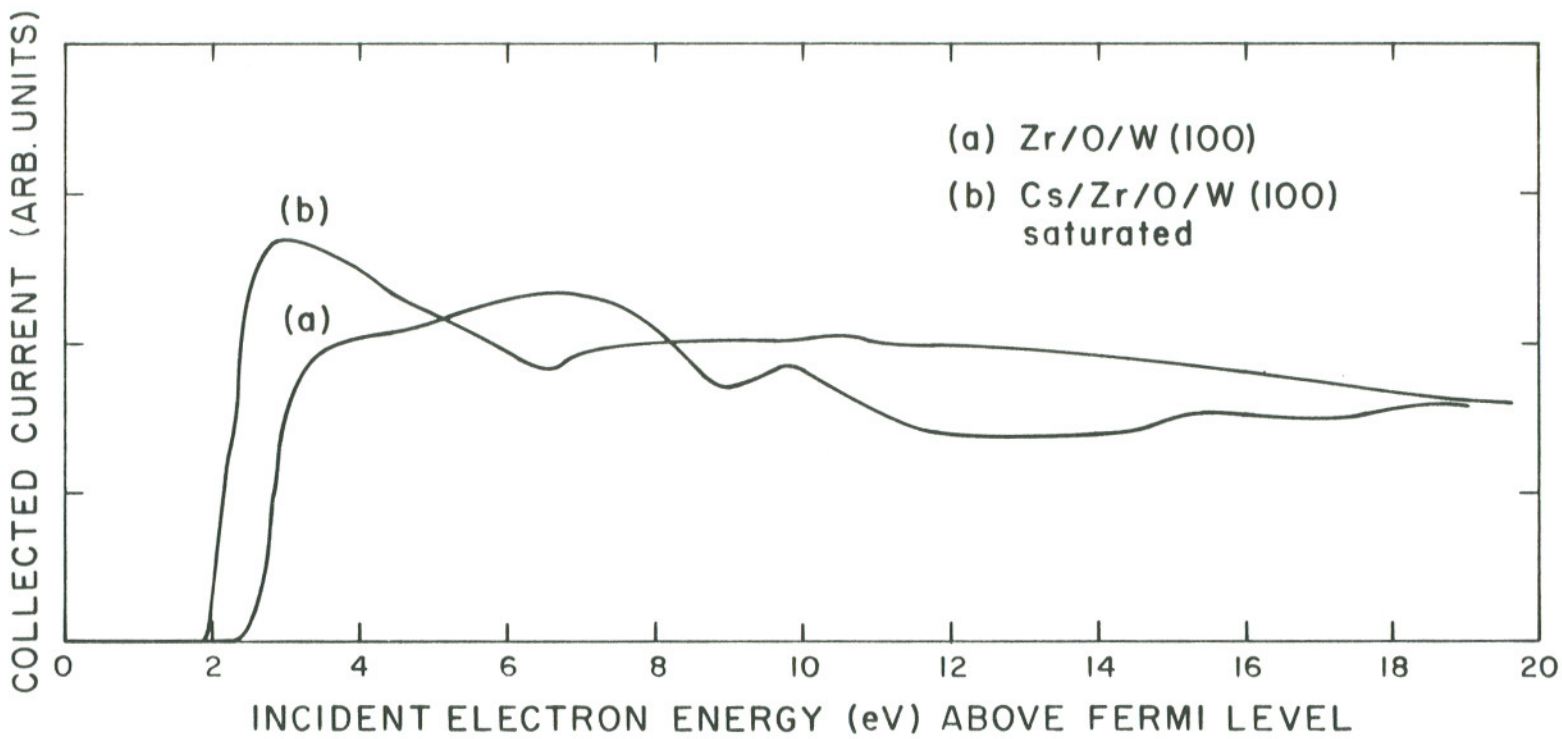

Figure 28. Experimental I(V) curves obtained for a) Zr/O/W(100) and b) Cs/Zr/O/W(100) - saturated.

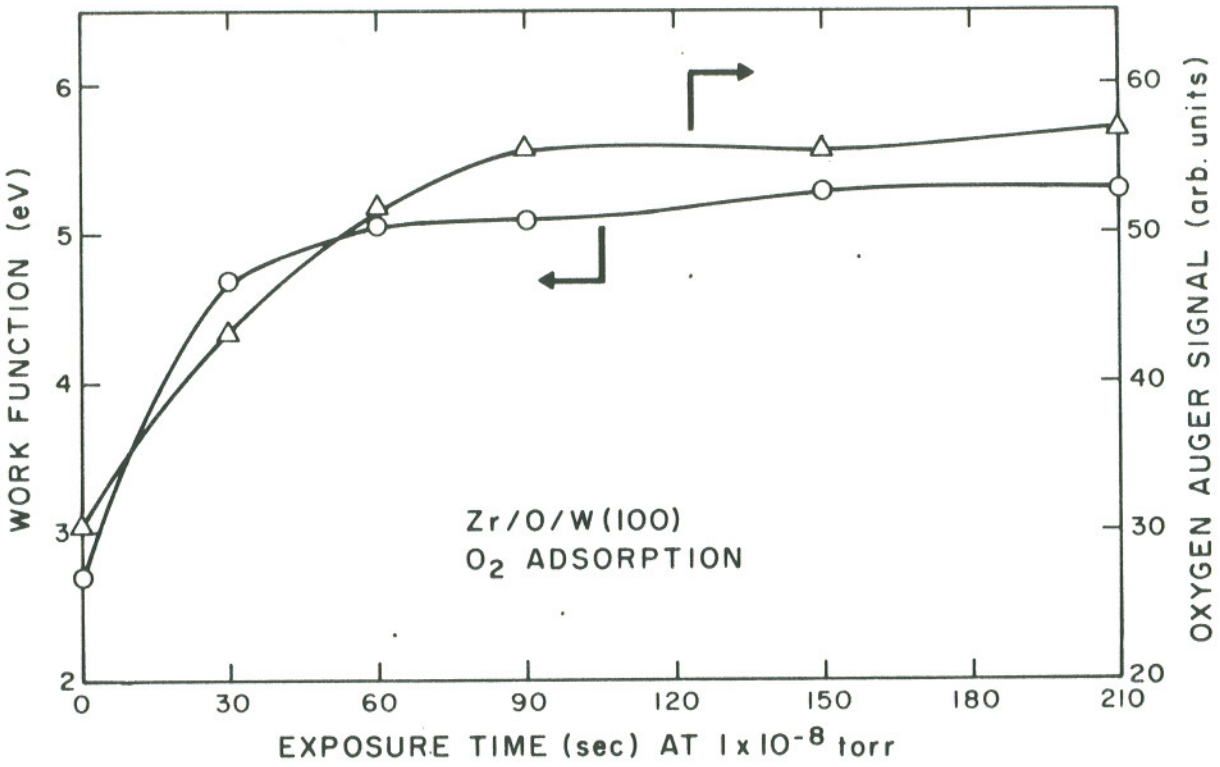

Figure 29. a) Work function and O Auger peak-to-peak amplitude increase during room temperature O adsorption on Zr/O/W(100).

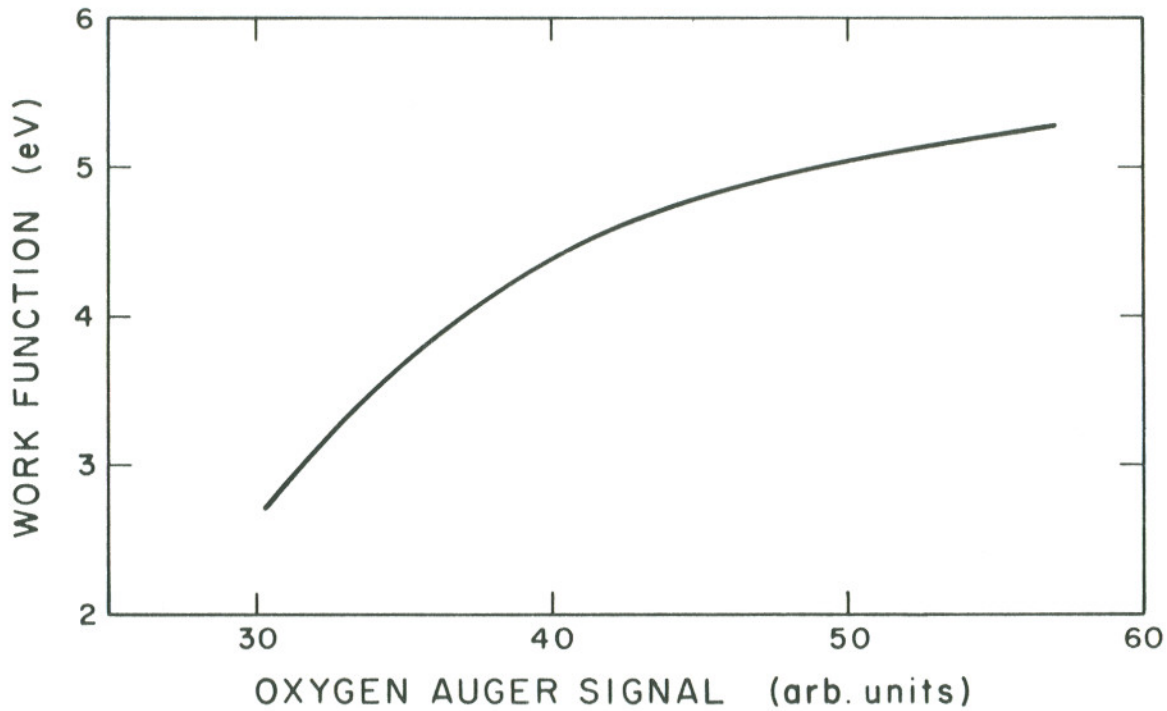

Figure 29. b) Data from a) plotted as work function vs. O Auger amplitude as a measure of coverage.

from 0.3 L to 0.9 L and levels out at higher O_2 coverages. After 0.9 L O_2 exposure, the sticking coefficient of O_2 drops significantly, and the surface is essentially saturated. These data are recast in Figure 29(b) to show the explicit variation of ϕ with O coverage, using the Auger peak-to-peak O signal as a measure of coverage.

The Zr/O/W(100) surface with "excess" O_2 is produced by the above O_2 dosing procedure. The surface may then be heated to 1600 K for 2 min in vacuum. The O_2 treated Zr/O/W(100) surfaces before heating and after heating are designated as thermally unequilibrated and equilibrated, respectively. The adsorption of Cs onto the Zr/O/W(100) surface covered with various amounts of excess O_2, both thermally equilibrated and unequilibrated, has been studied.

Adsorption of oxygen on the low work function Zr/O/W(100) surface shows that the rate of oxygen uptake decreases quite rapidly for room temperature adsorption, with saturation occurring at $\sim$ 0.9 L exposure. In contrast, E. Bauer et al.[39] have observed room temperature oxygen adsorption even after 4 L exposure with 0.66 L required to adsorb half a monolayer on an initially clean W(100) surface as shown in Figure 30. Desplat[40] has obtained the work function change vs oxygen exposure up to 70 L on a W(100) surface (Figure 31). The difference in adsorption behavior of the clean W(100) and Zr/O/W(100) is apparently caused by the presence of a significant amount of oxygen and Zr in the low work function Zr/O/W(100) layer, making fewer sites available for subsequent

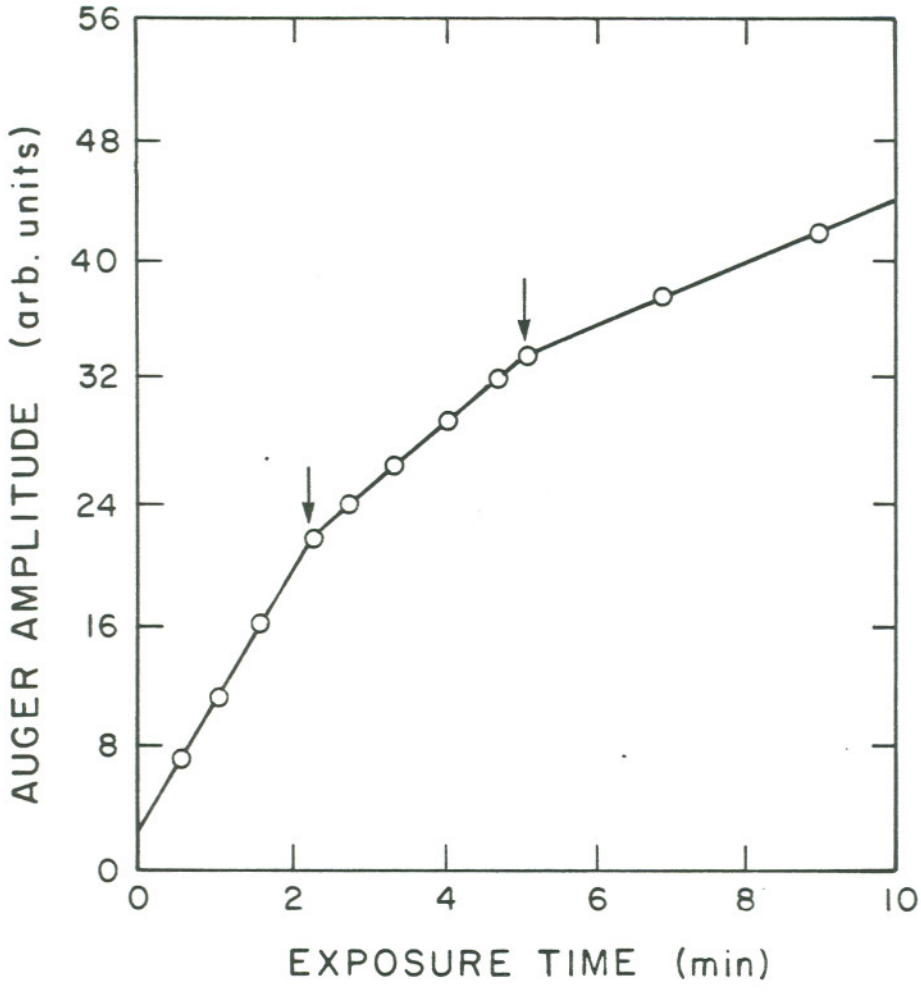

Figure 30. Oxygen Auger amplitude increase during room temperature O adsorption on W(100) with exposure to 5 x 10^{-9} torr oxygen (Ref. 39).

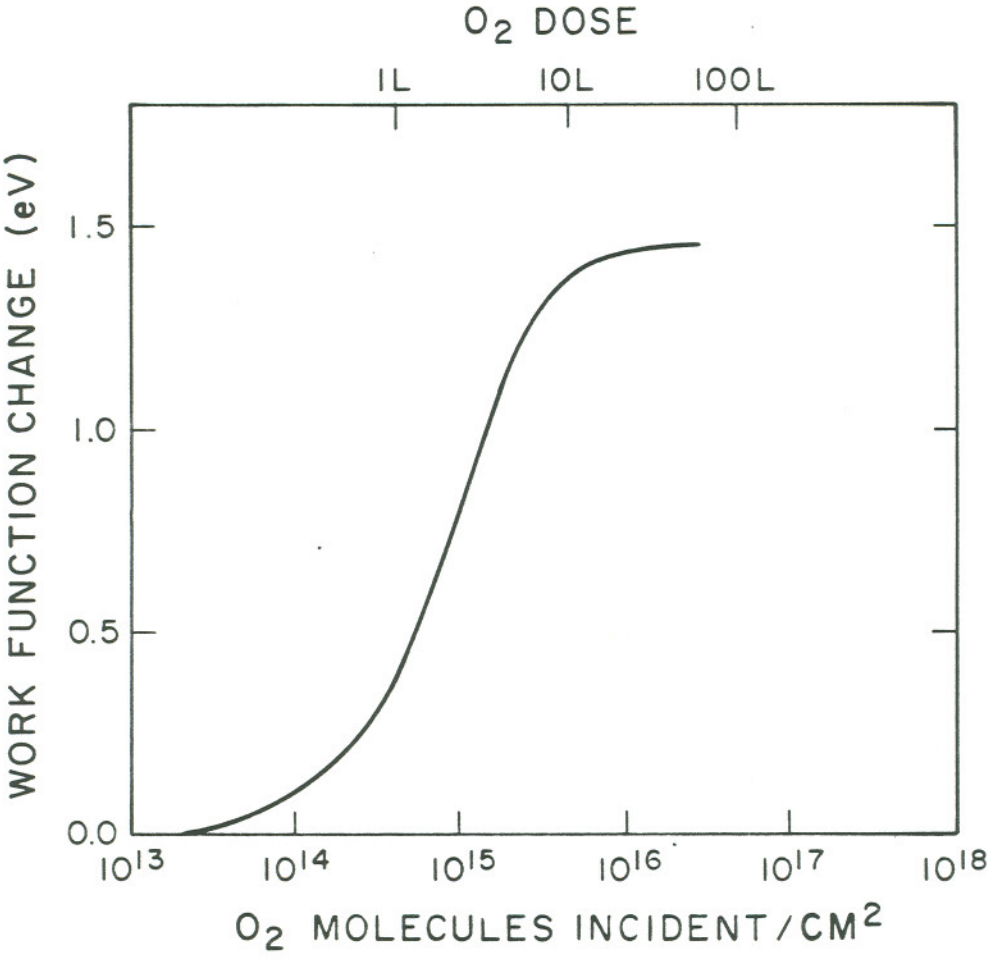

Figure 31. Work function change versus O_2 arrival rate for O adsorption on W(100) (Ref. 40).

oxygen adsorption. The oxygen initiallly present in the low work function layer is very tightly bound and intimately associated with the Zr atoms, as indicated by both the observed bulk co-diffusion of Zr and O and the extreme thermal stability of the low work function surface.[1]

4.3.b. ESD and Auger Measurement

The AES measurement for oxygen adsorption on the Zr/O/W(100) surface indicates that the oxygen Auger amplitude slowly decreased while AES primary beam was incident on the surface as shown in Figure 32. The explanation for this behavior is that electron stimulated desorption of oxygen occurred during exposure to the beam current. T. E. Madey has observed that a high-ion yield ESD state appears ($\sim 10^{-6}$ O^+ ions/electron) at oxygen coverage $\geqslant 8 \times 10^{14}$ atoms cm^{-2} on W(100) (Figure 33). Previous investigators of the O_2/W system have reported that the O^+ ion yields following low exposures to oxygen ($\leqslant 10^{14}$ to 10^{15} molecules cm^{-2}) are negligibly small, and have termed this "electronically inactive" state the β_2 oxygen state. The high ion-yield ESD state is called the β_1 state. T.E. Madey[41] also shows both the work function change and the absolute ESD O^+ ion yield as a function of average O_2 exposure (Figure 34). It shows the threshold exposure for appreciable O^+ liberation is $\sim 8 \times 10^{14}$ molecules cm^{-2} and at this exposure the work function change for the O_2 layer is about 1.0 eV.

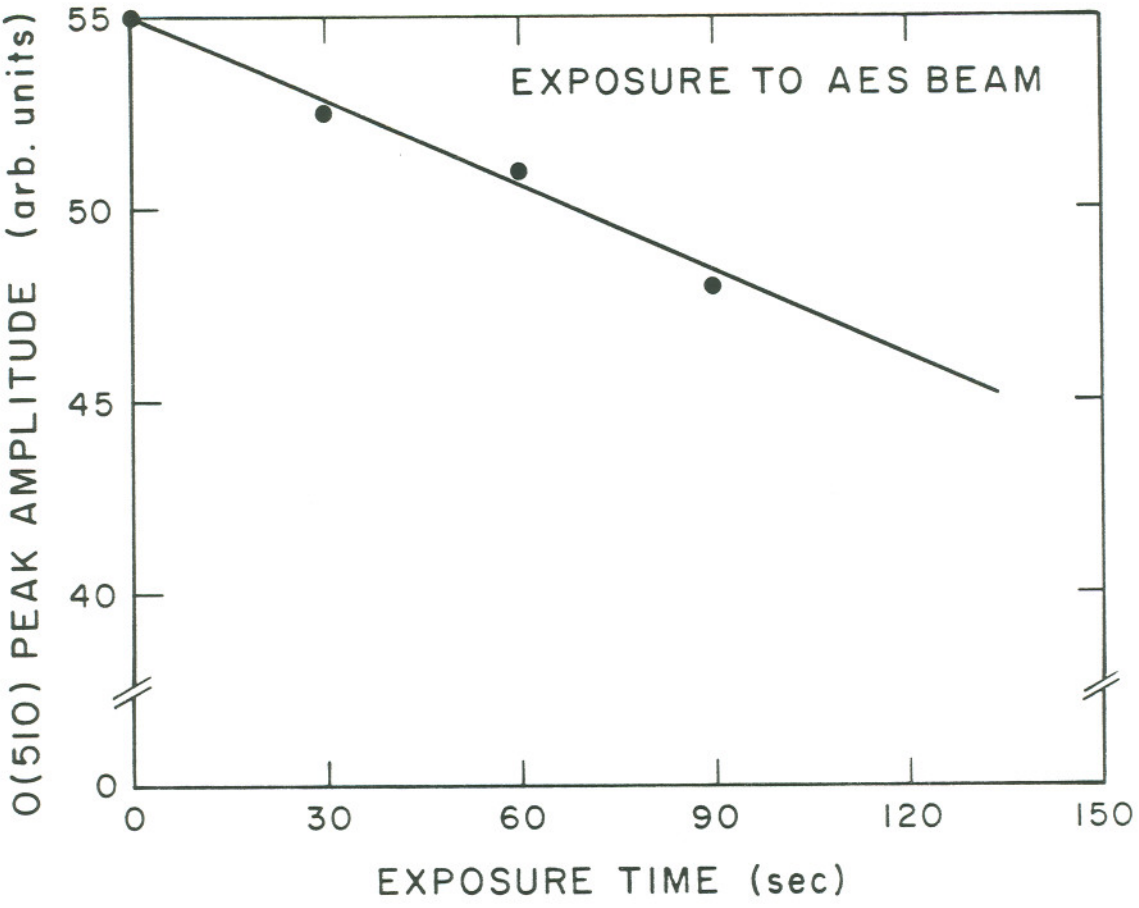

Figure 32. Oxygen Auger amplitude decrease during continuous primary electron beam impingement on the O/Zr/O/W(100) surface after a 2.1×10^{-6} torr - sec excess O dose.

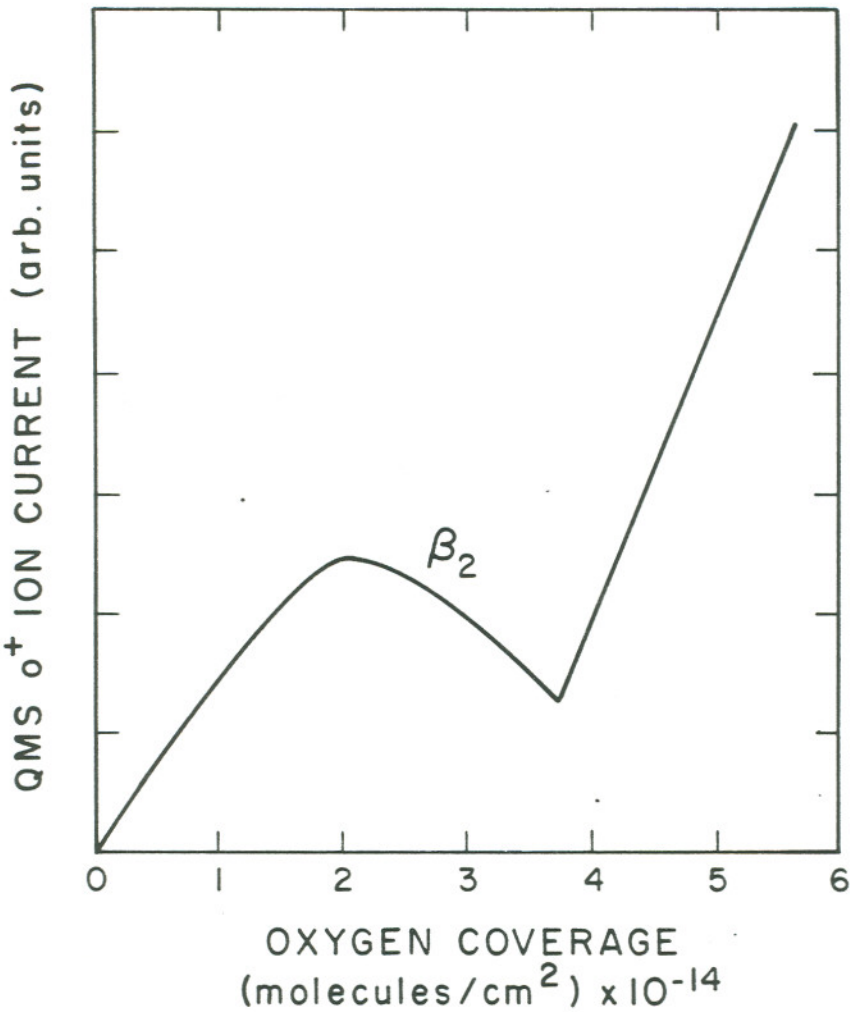

Figure 33. O^+ QMS ion current versus average O coverage during ESD of O/W(100) (Ref. 41).

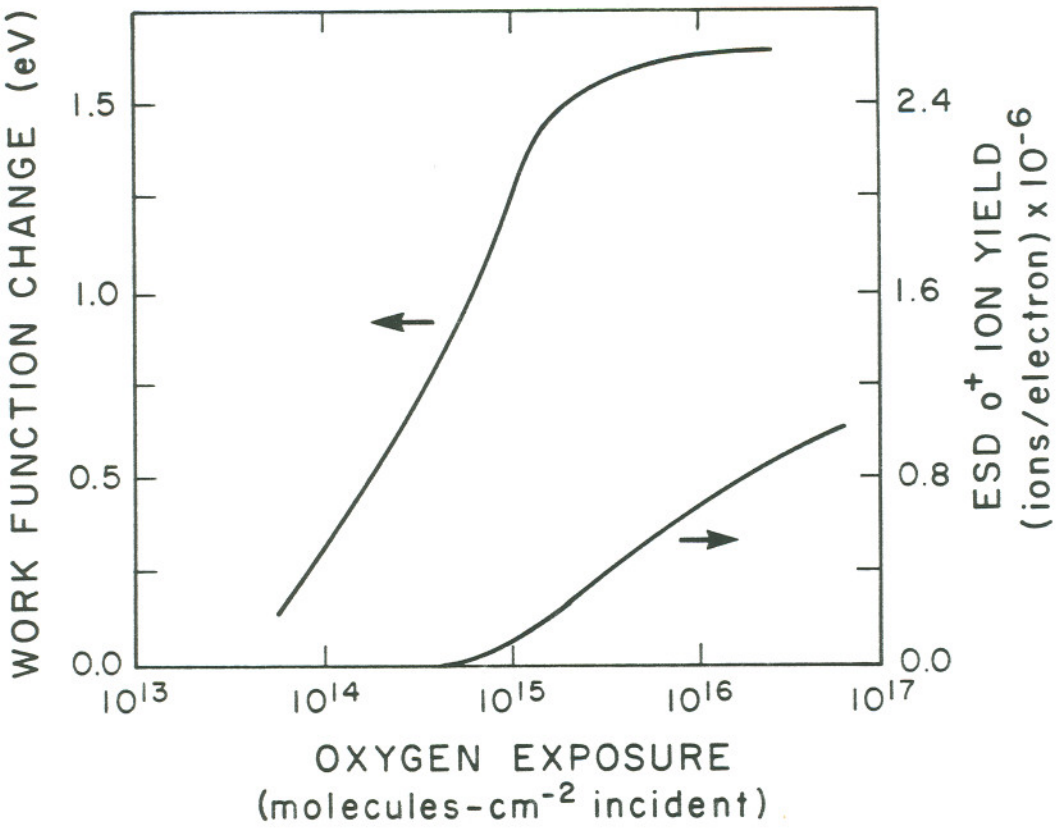

Figure 34. Work function change and absolute ESD ion yield as a function of average O exposure for O/W(100) (Ref. 41).

The maximum increase in the ion yield occurs at high exposures where the sticking probability (s) drops below ~ 0.01, and this continued increase in O^+ signal was noted in the work function plateau region. This observation was interpreted to mean that two states of adsorbed oxygen exist on W(100), the first causing the work function to increase 1.5 eV to the plateau region and the second causing an ion current upon electron impact.

The results of this study of O_2/Zr/O/W(100) can be compared with those obtained by Madey for O_2/W(100) based upon the observed similar behavior. In the O_2/Zr/O/W(100) system, the oxygen Auger amplitude decreases during electron bombardment as indicated in Figure 32, and Figure 29(a) shows that the work function remains the same for these oxygen Auger amplitudes (From 55 to 49). This implies the formation of a β_1-type state for high exposures of O_2 on Zr/O/W(100), as was observed under similar conditions for O_2 on W(100).

4.3.c. LEED - Unequilibrated Surface

Exposure of the low work function Zr/O/W(100) surface at room temperature to as much as 2.1 L of oxygen resulted in no extra features appearing in the LEED pattern which remained the same as that of the original Zr/O/W(100) apart from a strong increase in background intensity which suppresses the $\sqrt{5} \times \sqrt{5}$ spots. This implies that the adsorbed oxygen is disordered on Zr/O/W(100) surface. E. Bauer et al.[39] have carried out an extensive study for O_2 on W(100) systems. They observed the p(4 x 1) structure at oxygen

coverage θ_o = 0.5 and the streaked p(4 x 1) pattern with oxygen coverage $\theta_o > 1$ for adsorption at 300 K; simultaneously, the background intensities increased. Probably, above θ_o = 0.5 additional oxygen is adsorbed in a random manner.[42] In this study, there is a significant amount of oxygen already present in the low work function Zr/O/W(100) surface.

4.3.d. LEED - Thermally Equilibrated Surface

Heating the unequilibrated O_2 saturated Zr/O/W(100) surface to 1600 K produced a p(2 x 1) pattern as shown in Figure 35. The p(2 x 1) pattern has been observed during many O_2/W(100) studies.[39,43,44] Hopkins et al. also show that heating of a disordered W(100)-O surface produced a structure designated W(100) - (2 x 1)O when this surface was annealed to 1300 K. C.A. Papageorgopoulos et al.[44] have proposed the model for the p(2 x 1)-O structure as shown in Figure 36. The O_2 are assumed to dissociate into atoms and occupy positions underneath the W surface. The oxygen coverage is θ_o = 0.5 for the p(2 x 1)-O surface. E. Bauer et al.[39] have suggested two models for the p(2 x 1)-O structure associated with θ_o = 1 as shown in Figure 37. This model supports the previous interpretation in terms of reconstruction, but here the oxygen atoms are not assumed to be under the W atoms. A more elaborate structure analysis for O/Zr/O/W(100) system will be given later.

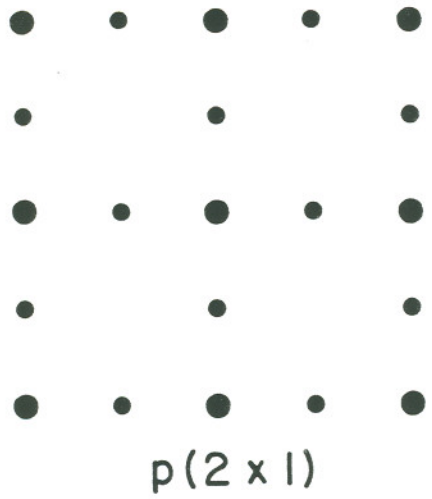

Figure 35. LEED pattern of thermally equilibrated surface of 0/Zr/0/W(100) with excess 0 coverage $\sigma/\sigma_{sat} = 0.6$.

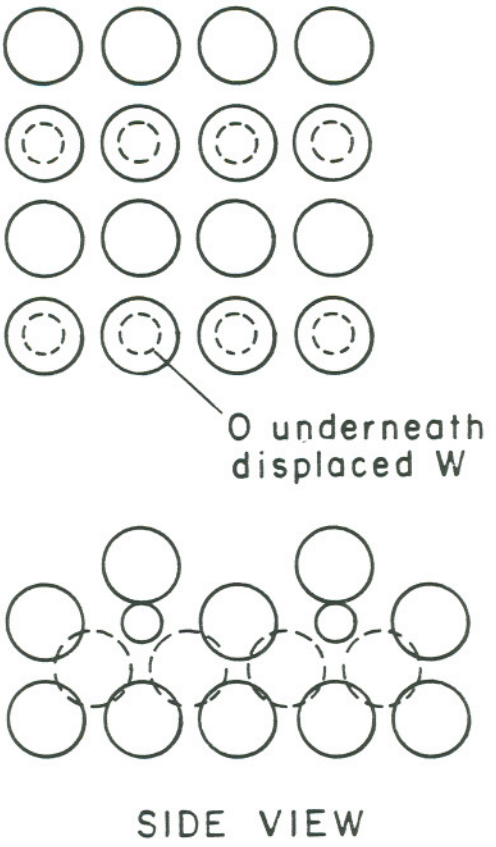

Figure 36. Surface model for O on W(100). Views of the reconstructed (2 x 1) - O surface, θ_O = 0.5 (Ref. 44).

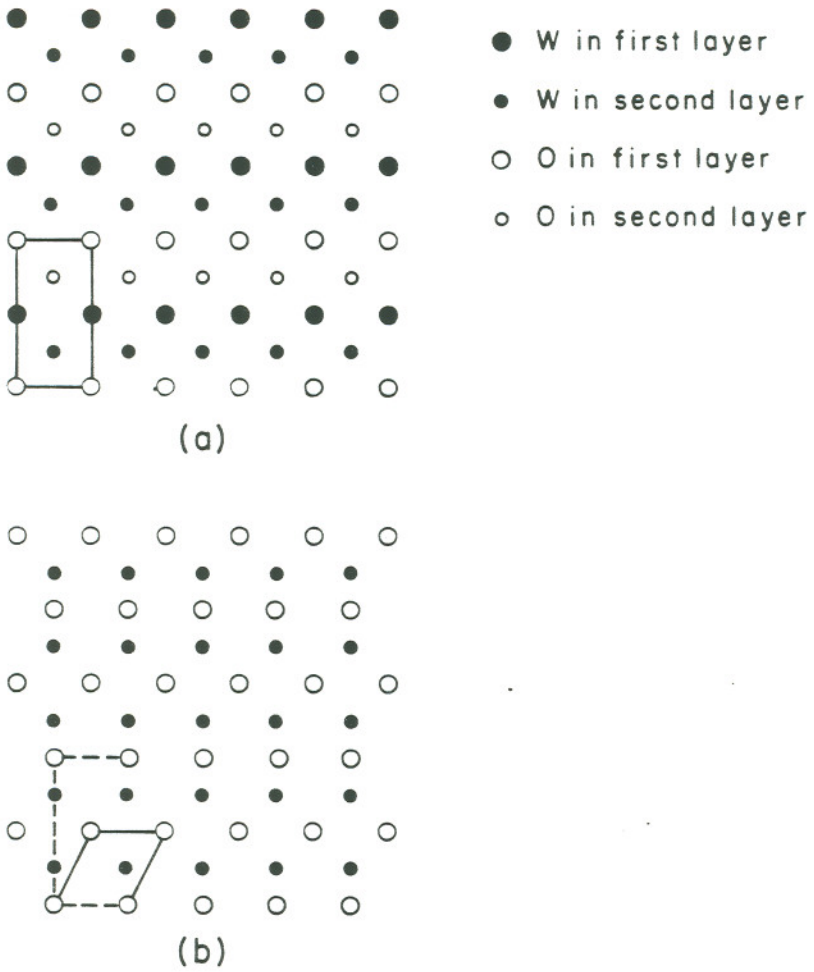

Figure 37. Possible models of surface structures corresponding to the O/W(100) p(2 x 1) LEED, θ_O = 1. (Ref. 39).

4.4. Cs - O_2 Coadsorption in Zr/O/W(100)

4.4.a. Work Function Versus Cs Dose Time - Unequilibrated Surface

The change of work function with Cs adsorption for a unequilibrated excess O_2 layer on the Zr/O/W(100) surface is also shown in Figure 24. Excess oxygen coverages (σ/σ_{sat}) are based upon Auger data, relative to the saturated oxygen Auger amplitude of 26.5 units. Oxygen coverages of 0.59, 0.83, 0.95 correspond to oxygen exposures of 0.3, 0.6, 0.9 L. These curves show four features at the higher oxygen coverages. First, the work function minima are lower. Second, the work function minima are shifted to higher Cs coverages. Third, the surfaces have lower work functions at saturated Cs coverage. Fourth, the surfaces have higher saturated Cs coverages. Compared with Cs on Zr/O/W(100), the work function minimum is reduced from 2.12 eV to 1.37 eV.

4.4.b. Work Function Versus Cs Dose Time - Thermally Equilibrated Surface

The work function changes with Cs adsorption on thermally equilibrated excess O_2 layers on the Zr/O/W(100) surface are shown in Figure 38. Oxygen coverages of 0.19, 0.55, 0.58 correspond to oxygen exposures of 0.3, 0.6 and 0.9 L. These curves show the same features as the unequilibrated case for higher oxygen coverages. The initial work functions for the three oxygen coverages following

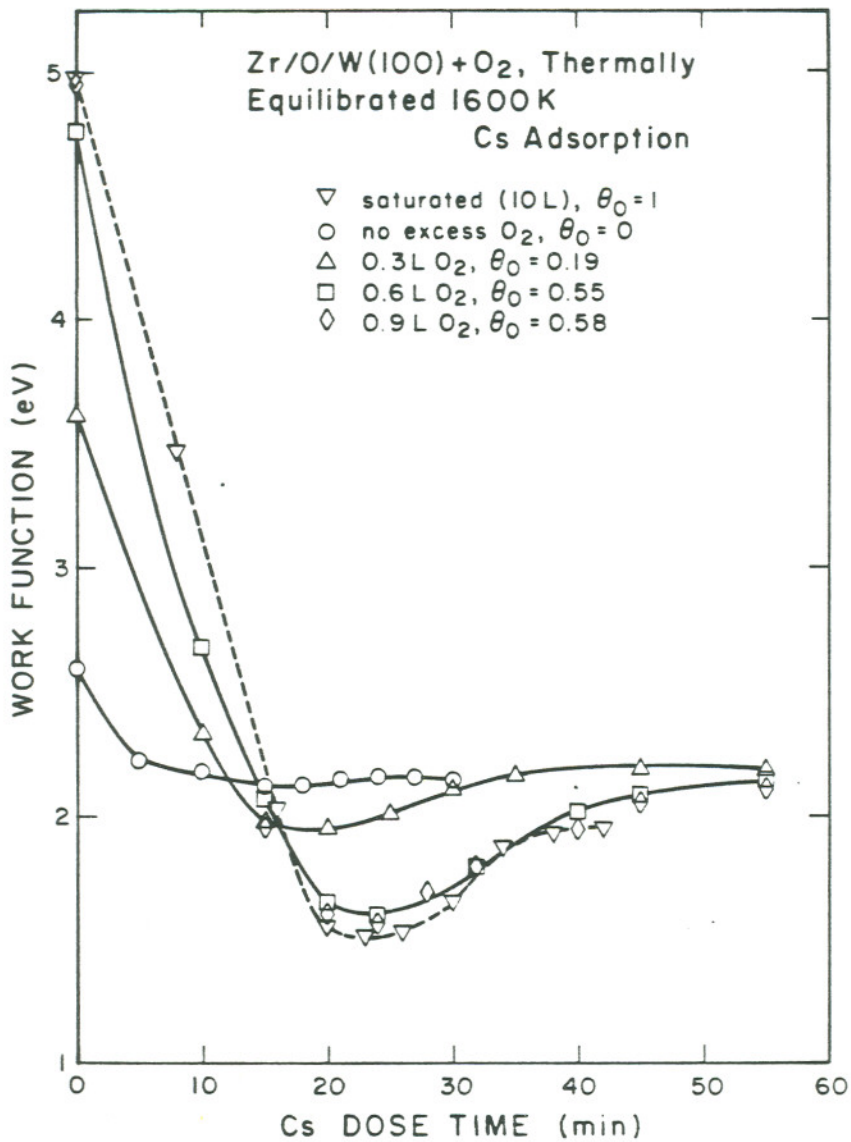

Figure 38. Work function versus dose time for Cs adsorption on Zr/O/W(100) with and without thermally equilibrated excess O layers. Excess oxygen coverages ($\theta_o = \frac{\sigma}{\sigma_{sat}}$) based upon Auger data.

thermal equilibration are 3.62, 4.76 and 4.96 eV, respectively. The adsorbed Cs work function minima for equilibrated 0.3, 0.6 and 0.9L oxygen doses are 0.2 ~ 0.35 eV higher than the corresponding unequilibrated cases, and the Cs saturation work functions are slightly higher. Saturated, thermally equilibrated oxygen layers (exposure of 10 L) on the Zr/O/W(100) surface have also been studied. The change of work function versus Cs dose time for this case is also shown in Figure 38. The work function minimum on the saturated, equilibrated surface is 1.51 eV, near the work function minima of the equilibrated surfaces that initially had lower oxygen coverages. The work function of higher Cs coverage on this surface, however, is slightly lower than the work functions of the other surfaces.

4.4.c. Work Function Versus Heating Temperature

Figure 25 shows the change in work function with heating temperature of an oxygen saturated, thermally equilibrated Zr/O/W(100) surface which was subsequently saturated with Cs at room temperature. This desorption curve shows a work function minimum ϕ_m 1.54 eV, by heating to 520 K, which is close to the work function minimum obtained during Cs adsorption on this surface. Complete Cs desorption occurs at about 1300 K. The final work function is slightly higher than the initial work function, because, during this prolonged heating, the excess oxygen causes some diffusion of the Zr - O complex into the bulk. As determined by

these desorption/work function experiments, the Cs adsorption/desorption process is approximately reversible on thermally equilibrated oxygen layers.

4.4.d. Cs Auger Amplitude Versus Cs Dose Time - Thermally Equilibrated Surface

A plot of Cs Auger amplitude versus Cs dose time on the oxygen saturated, thermally equilibrated surface ($\sigma/\sigma_{sat} = 0.6$) which is shown in Figure 26, is linear, and shows a sharp break in slope (corresponding to saturation coverage) at around 45 min. The corresponding Auger amplitude is twice as large as that of a saturated surface with no excess O. This surface thus requires approximately twice as much Cs to develop saturation coverage as does the Zr/O/W(100) surface without excess O_2, assuming unity sticking coefficient in both cases. In contrast to the constant O Auger signal observed during Cs adsorption on the low work function Zr/O/W(100) surface, the excess O Auger amplitude decreases as Cs coverage increases. This result implies that Cs adsorbs on top of excess O, thereby attenuating the O Auger signal.

4.4.e. Thermal Desorption Spectrometry of Cs

Cs thermal desorption from the thermally equilibrated and unequilibrated surfaces is strongly affected by excess O coverage. Figure 39 presents several flash desorption spectra for several

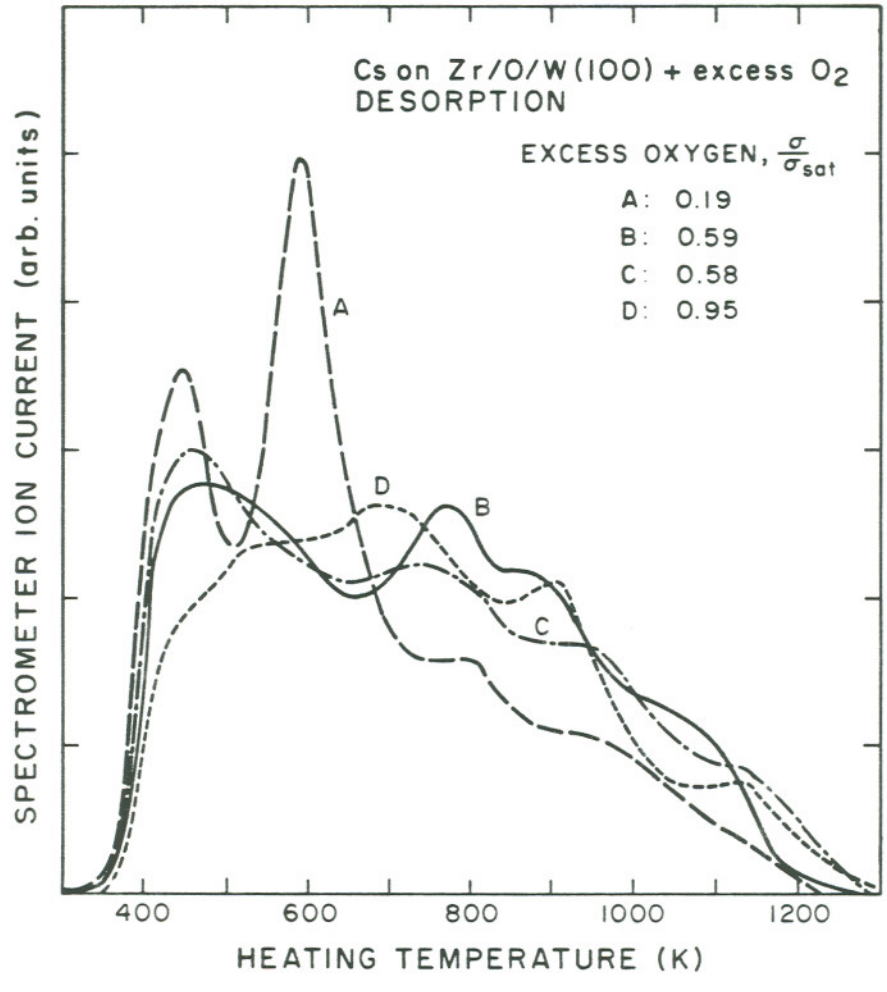

Figure 39. Thermal desorption of saturated Cs layers from Zr/O/W(100) with various amounts of preadsorbed excess O. The relative O coverages,

$\frac{\sigma}{\sigma_{sat}} = \theta_o$ are A: 0.19, B: 0.59, C: 0.58, D: 0.95.

excess oxygen coverages. A coverage of θ_o = 0.59 yields states with binding energies of 1.17, 1.95, 2.33 and 2.82 eV, while θ_o = 0.19 yields binding energies of 1.07, 1.48, 2.03 and 2.52 eV. For the unequilibrated O_2/Zr/O/W(100) surface with θ_o = 0.95, binding energies of 1.28, 1.72, 2.35 and 2.96 eV are observed, while the thermally equilibrated surface (θ_o = 0.58) has binding energies of 1.12, 1.85, 2.46 and 2.99 eV. Compared to the low work function ZrO/W(100) surface, these surfaces with excess oxygen show increased (higher temperature) binding energy states. The terminal desorption temperature for Cs adsorbed on an almost saturated layer of excess oxygen is around 1300 K. Note that curve A of Figure 39, corresponding to lowest oxygen coverage, exhibits the lowest terminal desorption temperature and predominance of low energy binding states.

4.4.f. LEED - Cs Adsorption

For saturated Cs coverage on the unequilibrated Zr/O/W(100) surface, the initial LEED pattern did not change but a high background was formed. The thermally equilibrated surface, however, exhibits a p(2 x 2) structure at saturated Cs coverage. This LEED pattern is shown in Figure 40.

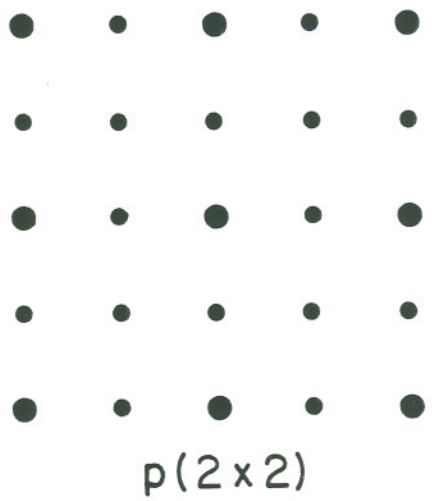

Figure 40. LEED pattern of saturated Cs layer on thermally equilibrated Zr/O/W(100) + excess O.

4.5. Summary of Auger Amplitudes

The Auger amplitude of Zr, W and O for two oxygen doses in the unequilibrated and thermally equilibrated cases are given in Table III.

TABLE III

THE AUGER AMPLITUDES OF Zr, W, O OF THE UNEQUILIBRATED AND THERMALLY EQUILIBRATED $Zr/O/W(100)+O_2$ SURFACES WITH TWO DIFFERENT OXYGEN DOSES

A. 0.3 L O_2 Dose

	Zr(147)	W(169)	O(510)	Zr/O	W/O	Zr/W
Flash ∿ 2000 K	21	24	31.5	0.66	0.76	0.875
Dose 30 sec. 10^{-8} Torr O_2	17.5	22	47	0.37	0.47	0.795
Heat to 1600 K	15.7	24.2	36.5	0.43	0.66	0.640

B. 0.6 L O_2 Dose

	Zr(147)	W(169)	O(510)	Zr/O	W/O	Zr/W
Flash ∿ 2000 K	19	21.1	24	0.79	0.879	0.90
Dose 60 sec 10^{-8} Torr O_2	17	19.7	46	0.37	0.428	0.862
Heat to 1600 K	15.5	19.8	38.5	0.40	0.51	0.782

The experimental values in Table III offer background for analyzing the results of Cs adsorption on the Zr/O/W(100) surface with various oxygen coverages. These Auger data were not easily obtained for a variety of experimental reasons, e.g.

1. it took quite a long time to scan the full spectrum,
2. ESD occurred and,
3. two different modulating voltages and recorder Y axis scales had to be used.

Nevertheless, from Table III, several observations can be made:

1. The oxygen dose level has little effect on the Zr/W Auger ratio; however heating to 1600 K reduces the Zr/W ratio in both cases.
2. The O and Zr Auger amplitudes both decrease (relative to W) during thermal equilibration at 1600 K.
3. The Zr/O ratio of the thermally equilibrated surface shows smaller increase than the W/O ratio, however both are affected by O_2 adsorption.

From these observations we may conclude that both Zr and W act as sites for O_2 adsorption, but that after thermal equilibration O on the W sites are less populated. In addition both Zr and O are reduced in concentration when the excess oxygen surface is heated to 1600 K.

4.6. Cs Adsorption on W(100)

4.6.a. Work Function Versus Cs Dose Time

The change of work function with Cs adsorption on the clean W(100) surface is shown in Figure 41. The Cs flux was different from that of previous experiments, since a new Cs dispenser source was used. The minimum work function is ϕ_m = 1.72 eV and the saturated work function for 6 min Cs dose is ϕ_s = 1.95 eV.

4.6.b. Cs Auger Amplitude Versus Cs Dose Time

Figure 42 shows the Cs Auger peak-to peak amplitude vs Cs adsorption time on W(100). This curve is linear with a break in slope around 6 min dose, indicating that it takes 6 min to form one monolayer Cs coverage on W(100) surface, if unity sticking coefficient is assumed. The W(169) Auger peak amplitude decreases 30% when the surface is fully covered with Cs at room temperature.

4.6.c. Work Function Versus Heating Temperature

The change in work function with Cs desorption from a Cs covered surface of W(100) is shown in Figure 43. Heating to 480 K caused an initial lowering of work function to 1.70 eV, which is close to the minimum observed from Cs adsorption on the W(100)

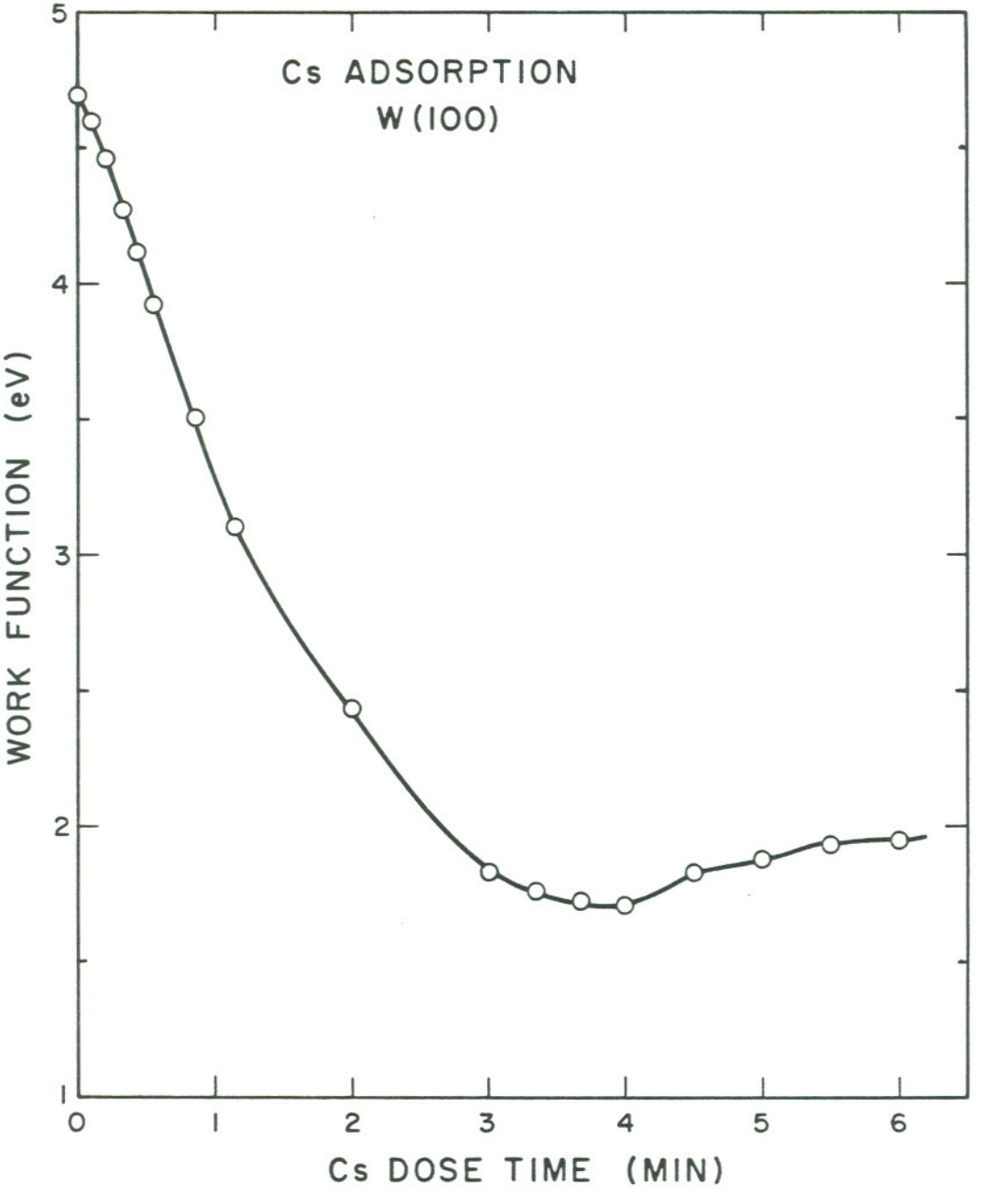

Figure 41. Work function versus dose time for Cs adsorption on W(100).

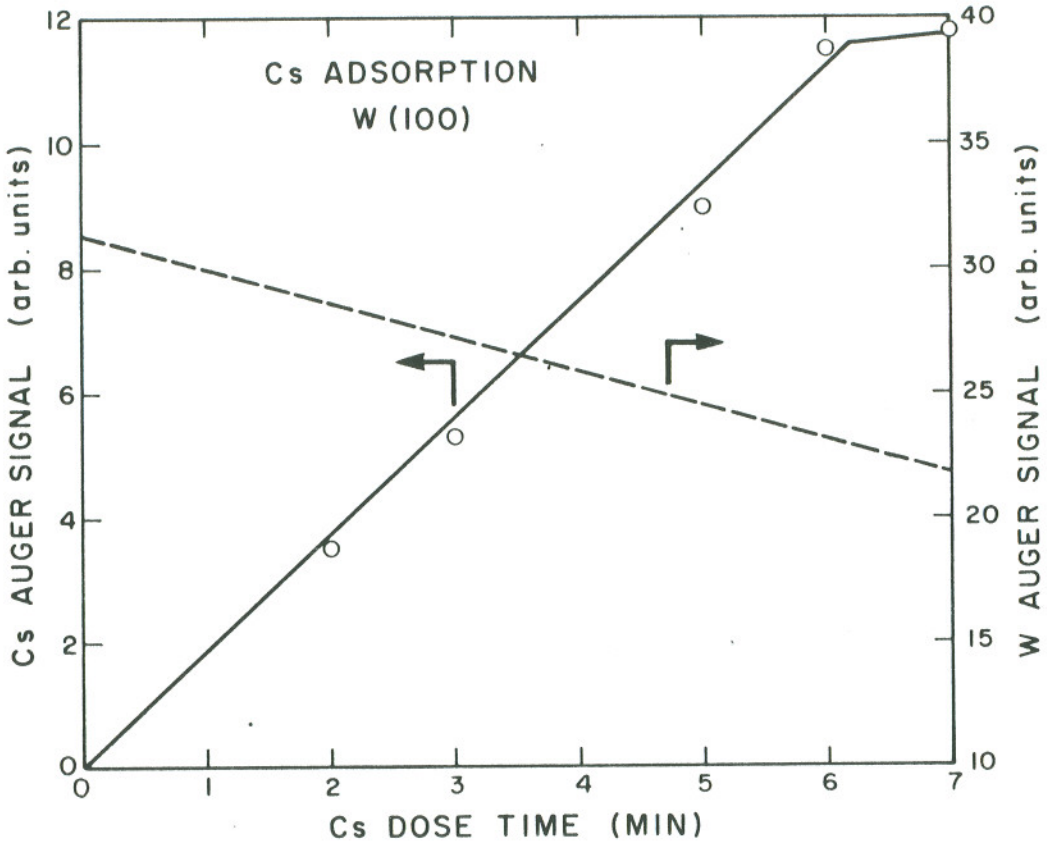

Figure 42. Cs(563 eV) and W(169 eV) Auger peak-to-peak amplitudes versus dose time for Cs adsorption on W(100).

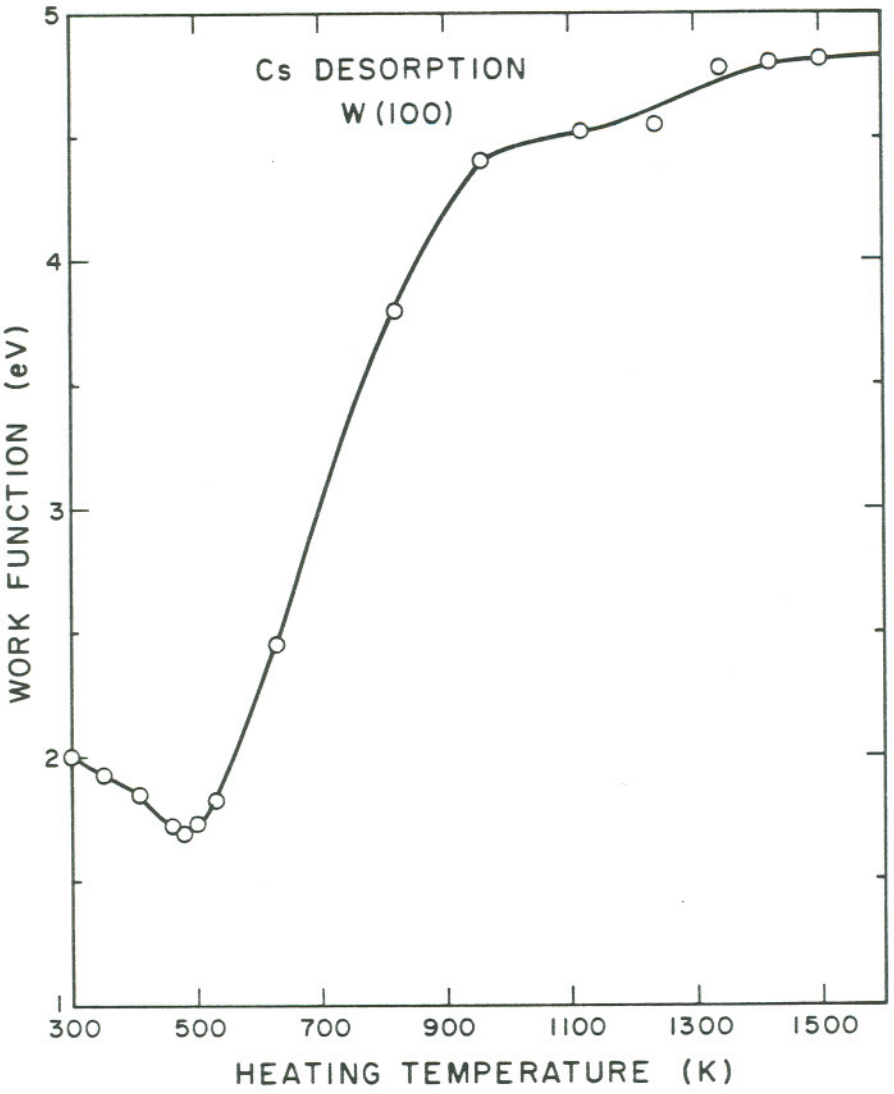

Figure 43. Work function versus desorption temperature for an initially saturated Cs layer on W(100).

surface. Heating to the range of 1240 - 1340 K yielded the work function of the clean W(100) surface.

4.6.d. Thermal Desorption Spectrometry of Cs

Neutral Cs desorption spectra are presented in Figure 44, as functions of the fractional Cs coverage $\theta_{Cs} = \sigma/\sigma_{sat}$. The amplitudes of these curves have been corrected for the non linear sample heating rate. The curves show that as θ_{Cs} increases, the high energy desorption peak shifts slightly to lower temperature, then saturates around $\theta_{Cs} = 0.46$. For higher Cs coverage, another low energy desorption peak appears, which shifts to lower temperature for much higher Cs coverage. The temperature at which the high energy desorption peak occurs does not change with coverage, thus indicating that desorption from this chemisorbed phase is first-order with a fixed activation energy. For the low energy desorption peak, the temperature of the peak decreases with increasing coverage, so the reaction may be second-order with fixed activation energy, or first-order with an activation energy dependent on coverage. It is possible to distinguish between these two cases. The desorption rate curve for $\theta_{Cs} = 0.30$ was chosen as a reference for the high energy chemisorbed phase. The desorption rate curves for $\theta_{Cs} = 0.46, 0.65, 0.75$ and 1 were subtracted from the adjusted amplitudes for the high energy phase. The resultant amplitudes

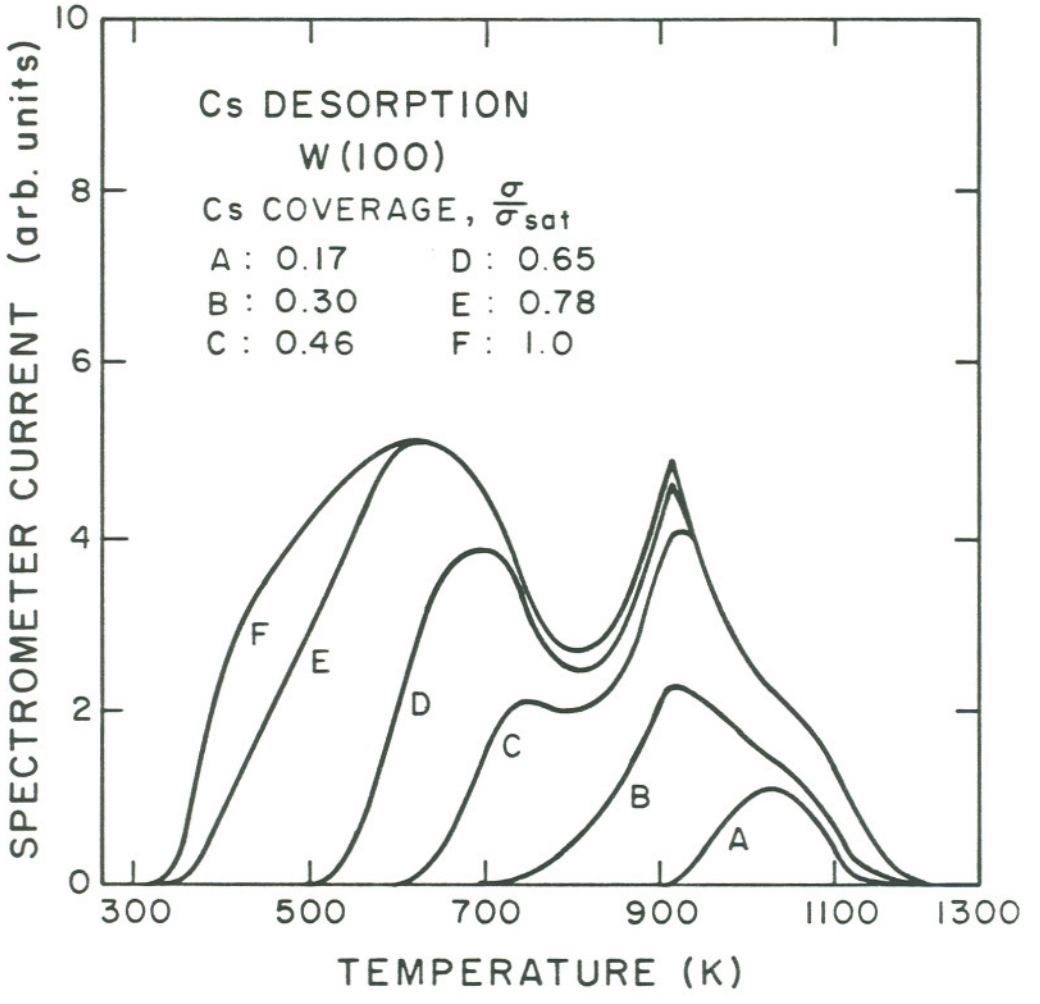

Figure 44. Thermal desorption of Cs from W(100) for various initial coverages.

versus temperature which are shown in Figure 45 represent the desorption rate curves for the low energy chemisorbed phase. The initial surface coverage σ_o can be found from the area under the curve of desorption rate against temperature. A plot of log $\sigma_o T_p^2$ against $1/T_p$ is shown in Figure 46. This curve is not a straight line as would be observed for second-order desorption with fixed activation energy. Therefore, desorption of the low energy chemisorbed phase is a first-order reaction with an activation energy dependent on coverage. The desorption energy of the high energy chemisorbed phase was calculated, using the Redhead equation, to be 2.27 eV. The Cs^+ ion desorption spectra are shown in Figure 47.

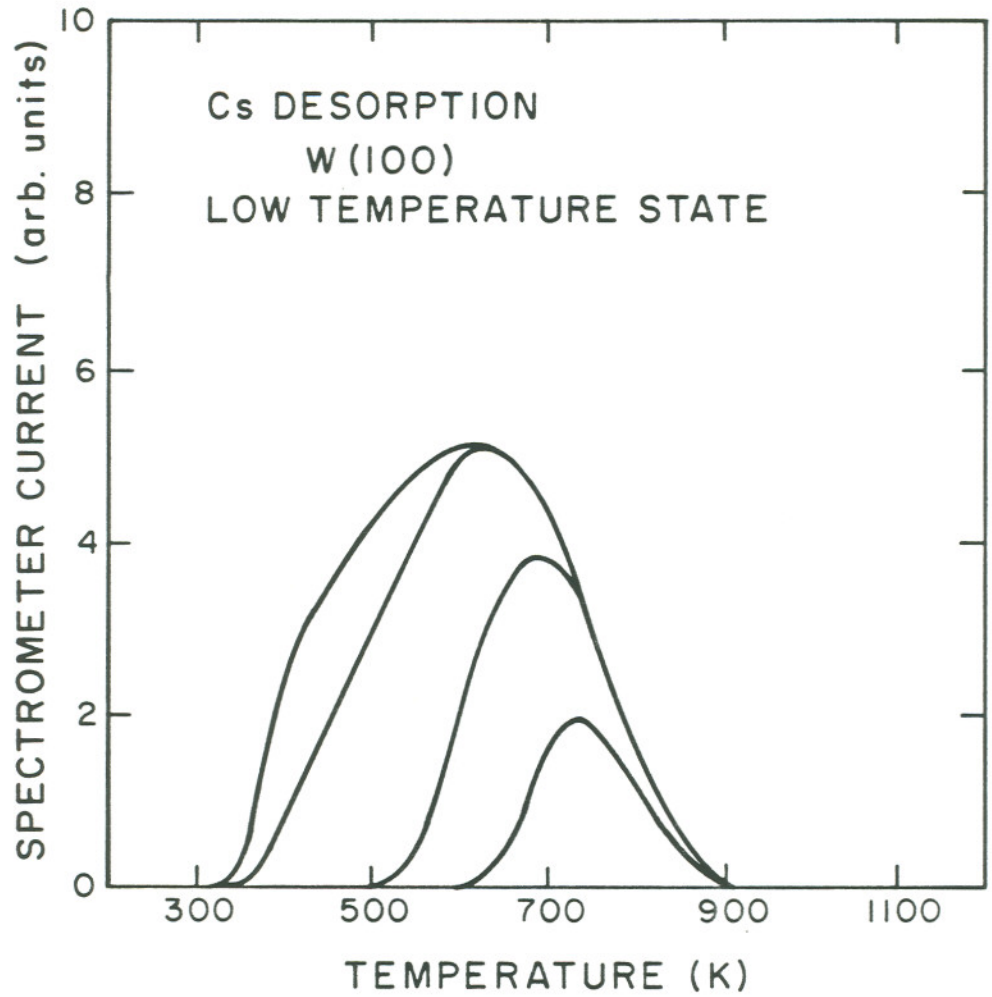

Figure 45. Thermal desorption of Cs from W(100): the low temperature state.

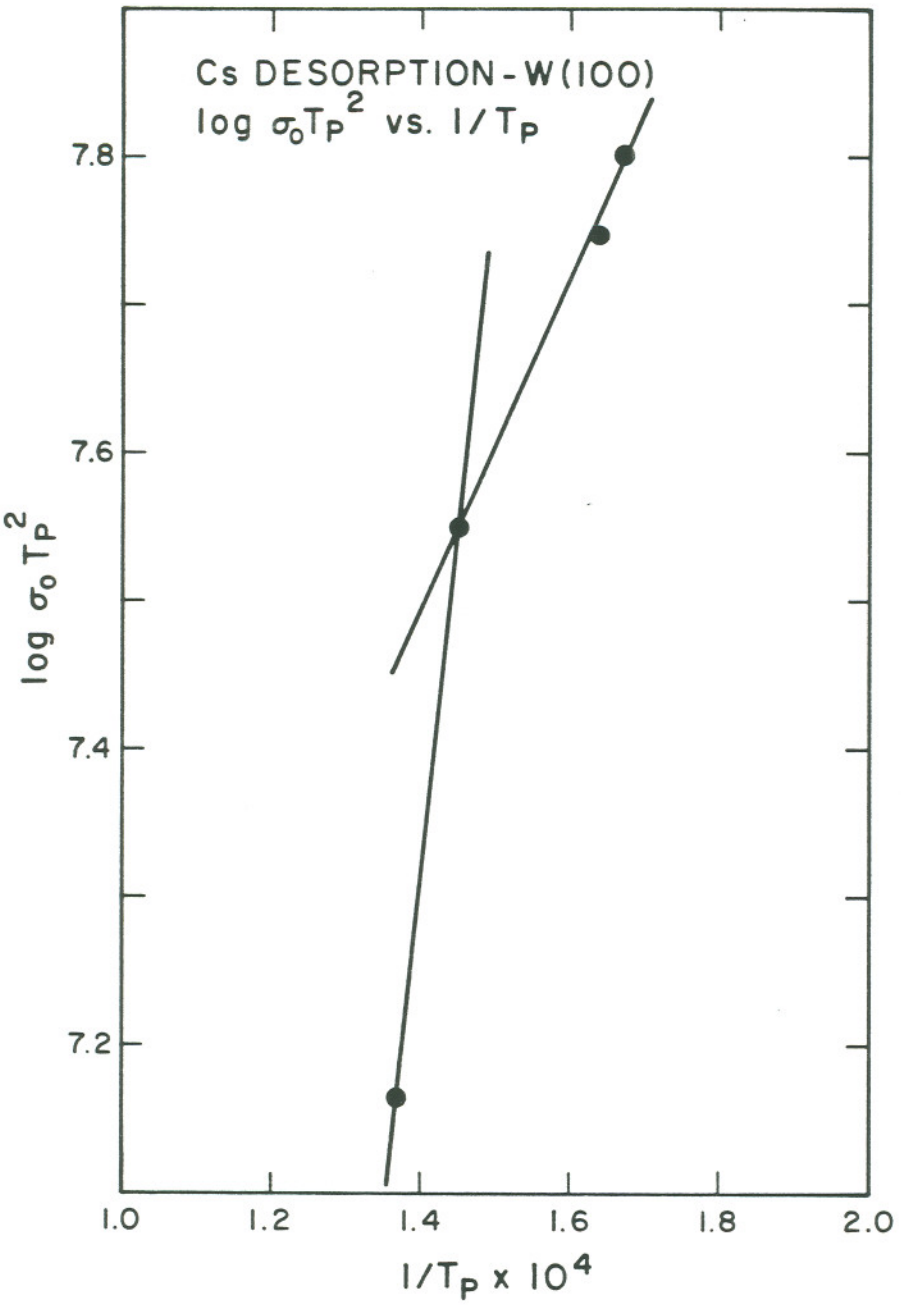

Figure 46. Log $\sigma_o T_p^2$ versus $1/T_p$ for Cs desorption from W(100).

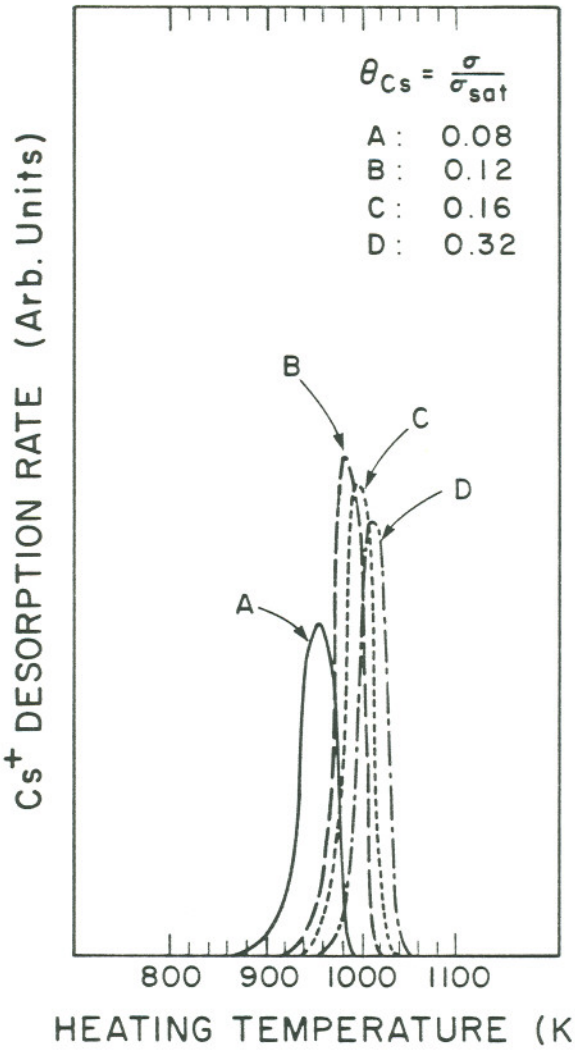

Figure 47. Thermal desorption rate of Cs^+ from W(100) for various initial coverages, $\frac{\sigma}{\sigma_{sat}} = \theta_{Cs}$. A: $\theta_{Cs} = 0.08$, B: $\theta_{Cs} = 0.12$, C: $\theta_{Cs} = 0.16$, D: $\theta_{Cs} = 0.32$.

CHAPTER 5

DISCUSSION

5.1. Cs Adsorption on Zr/O/W(100) and O/Zr/O/W(100)

5.1.a. Structure of Zr/O/W(100)

LEED patterns showing (1 x 1), (4/3 x 2) and ($\sqrt{5}$ x $\sqrt{5}$) $\tan^{-1}$ 0.5 structures (Figure 23) have all been observed for the low work function Zr/O/W(100) surface. The real lattice structure for each pattern is shown in Figure 48. The (1 x 1) structure model for Zr/O/W(100) has been suggested by L.R. Danielson and L.W. Swanson.[1] The Zr-O complex can form a dipole (positive end outward), normal to the surface without severe distortion of the tungsten lattice. The (1 x 1) pattern indicates the formation of a well-ordered overlayer of Zr-O dipoles in registry with the tungsten lattice. In a previous LEED study by Hill et al.,[7] the "W(100), c(4/3 x 2) - Zr" pattern was reported and attributed to 3/4 monolayer Zr on clean W(100), with supposedly oxygen-free zirconium adsorption. P. R. Davis observed the same pattern but only after annealing to T $\hat{=}$ 1900 K a layer consisting of O adsorbed onto preadsorbed Zr.[10] The Zr and O coverages corresponding to this structure were $\theta_{Zr} \hat{=} 1$ and $\theta_{O} \hat{=} 3/4$ as determined by AES, however, the work function of this surface was not measured. The ($\sqrt{5}$ x $\sqrt{5}$) $\tan^{-1}$ 0.5 pattern was also observed by P.R. Davis in the experiment of coadsorption of Zr and O on

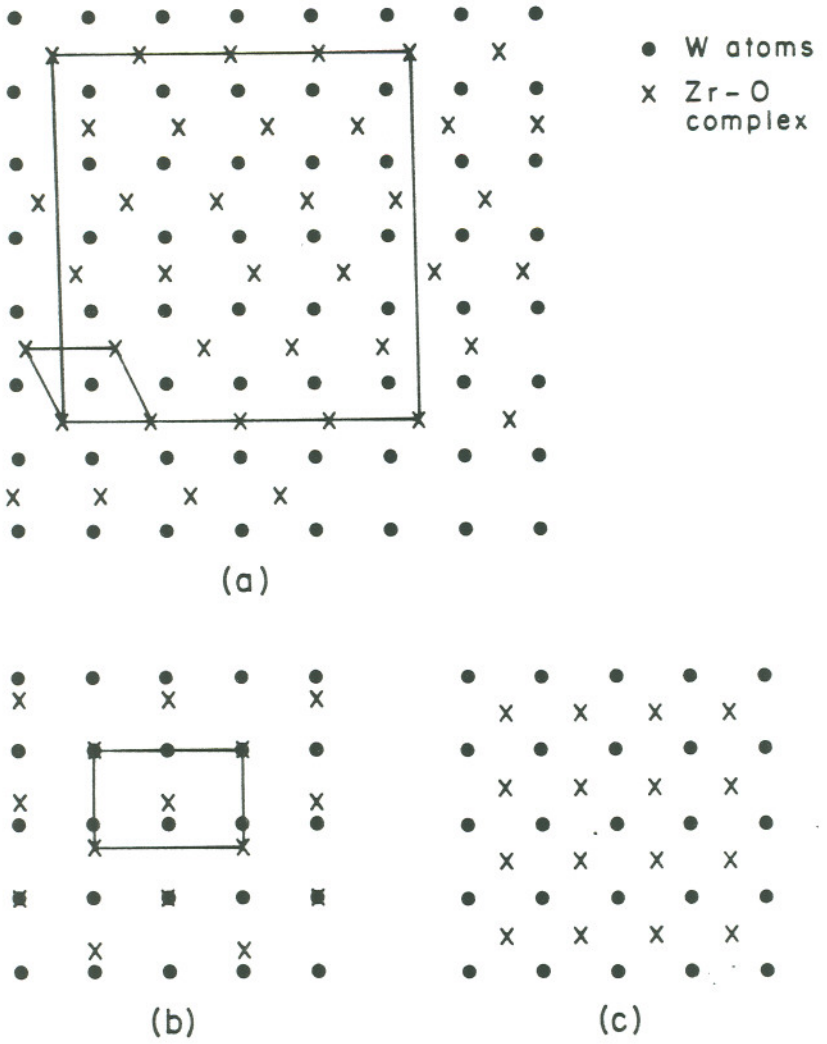

Figure 48. Possible surface structures corresponding to LEED patterns observed for the system Zr/O/W(100) near minimum work function. a) $\sqrt{5} \times \sqrt{5}$ $\tan^{-1} 0.5$; b) c(4/3 x 2); c) (1 x 1).

W(100).[45] This pattern occurred at the work function minimum, for initial O coverage in the range $0.25 \leqslant \theta_o \leqslant 1$. For the lowest work function of 2.6 eV, $\theta_o \doteq 0.85$ and $\theta_{Zr} \doteq 0.95$. It is quite difficult to choose a structure model for the low work function Zr/O/W(100) surface since it has three LEED patterns. Slightly different concentrations of Zr and O on the W surface which cause a small change in the work function minimum may also create slightly different structures. The Zr concentrations corresponding to different patterns are the following: For the (1 x 1) pattern, every tungsten site on the surface has a nearby zirconium atom (Zr/W=1). In the (4/3 x 2) pattern, for every four tungsten sites on the surface there are three zirconium atoms (Zr/W = 0.75). The $(\sqrt{5} \times \sqrt{5})$ $\tan^{-1} 0.5$ pattern implies that for every five tungsten sites on the surface, there are four zirconium atoms (Zr/W = 0.8). In principle, then, only slightly different amounts of Zr on the surface, could produce the observed different LEED patterns.

In view of the extreme thermodynamic stability of ZrO_2 (ΔH = -1105 KJ $mole^{-1}$) in comparison with WO_2 (ΔH = -647 KJ $mole^{-1}$) we anticipate that the ZrO complex exists on the surface and that the outermost layer is Zr atoms. The exact arrangement of the ZrO complex on the W(100) surface is not established except that the LEED data suggest that the lateral spacing of the adsorbed ZrO is almost identical to the W lattice constant.

5.1.b. Auger

In the case of the Cs/Zr/O/W(100) Auger results (see Figure 26) the oxygen Auger amplitude does not decrease as the Cs coverage increases, which might imply that the Cs atoms are situated above the open W rather than the protruding Zr-O sites. If the Cs atoms were situated above the Zr atoms, the Auger amplitude of the underlying oxygen should decrease in contrast to the Figure 26 results.

For the O/Zr/O/W(100) system, the adsorbed oxygen appears to be located at both the Zr and W sites. Thus, the Auger amplitude of W and Zr decrease simultaneously with excess O_2 adsorption according to Table 3. In section 4.5, it was shown that the oxygen atoms may prefer the protruding Zr-O sites rather than the W sites. We propose an arrangement as shown in Figure 49 where we designate the O-Zr (excess O) bond as the A bond, and the O-W (excess O) bond as the B bond, as shown in Figure 49. The primary effect of thermal equilibration of excess oxygen layers at 1600 K for two minutes is a reduction in the total amount of oxygen and slight reduction in the amount of zirconium at the surface as determined by AES (section 4.5.).

Adsorption of Cs on the O/Zr/O/W(100) surface leads to a decrease of the oxygen Auger amplitude as the Cs coverage increases. This result implies that the large Cs atoms adsorb at the excess oxygen sites, thereby attenuating the oxygen Auger signal as shown in Figure 26.

In the Cs/W(100) system, the W(169) Auger amplitude decreases linearly as the Cs coverage increases as shown in Figure 42.

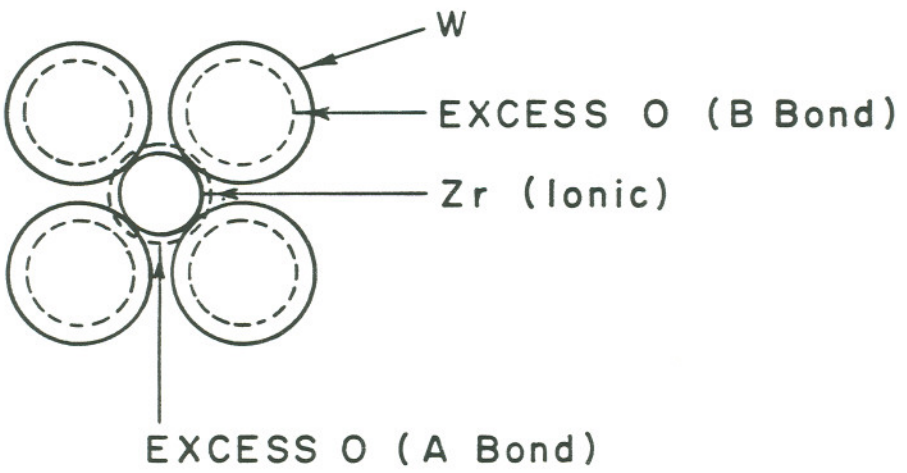

Figure 49. Possible excess 0 adsorption sites on Zr/0/W.

5.1.c. LEED

In the Cs/Zr/O/W(100) system, the lack of an ordered saturated Cs structure is probably due to surface mobility of Cs at room temperature. Thus, the LEED pattern does not change significantly, but only the background intensity increases.

Unequilibrated excess oxygen on the Zr/O/W(100) surface is also disordered. However, thermal equilibration of the surface produces an ordered p(2 x 1). From Section 5.1.a. the low work function Zr/O/W(100) surface occurs at an oxygen coverage θ_o = 0.85. The p(2 x 1) structure observed for the equilibrated O/Zr/O/W(100) surface may be similar to that described by Bauer shown in Figure 37.

For the unequilibrated Cs/O /Zr/O/W(100) surface, the LEED pattern is incoherent. This is reasonable, because the starting O /Zr/O/W(100) surface is already disordered. However, for Cs adsorption on the thermally equilibrated surface the p(2 x 2) pattern has been observed. The p(2 x 2) pattern can be formed by superposition of the p(2 x 1) and c(2 x 2) patterns. (see Figure 50). A c(2 x 2) pattern may be formed by the excess oxygen in the presence of a Cs overlayer, due to the strong Cs-O interaction. The electronegativities of Cs and O are 0.7 and 3.5 respectively. Due to this large electronegativity difference, the Cs-O interaction is quite strong even though the underlying oxygen is tightly bound to the Zr/O/W(100) surface. The combination of

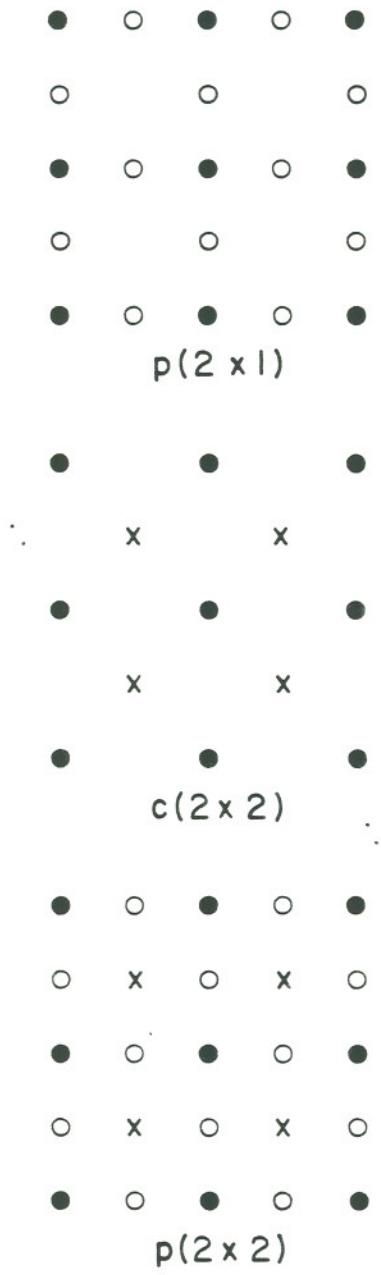

Figure 50. Demonstration of superposition of p(2 x 1) and c(2 x 2) LEED patterns to produce p(2 x 2).

the latter c(2 x 2) and the former p(2 x 1) structures may form the observed p(2 x 2) pattern. The LEED analysis in this case is very tentative, since we have a highly complex surface in which four components are involved.

5.1.d. Work Function

In the Cs/Zr/O/W(100) experiment, the minimum work function achieved is 2.12 eV. Due to protrusion of the Zr atoms, it is unlikely that the adsorbed Cs forms a direct bond with underlying oxygen atoms, thus, there is no significant increase of dipole moment due to Cs adsorption. The work function minimum is therefore not as low as Cs/O/W or Cs/W. Also, the saturation plateau for the Cs/Zr/W(100) work function is higher for the same reason.

An empirical relationship between the maximum work function change $\Delta\phi_m$ and substrate work function ϕ_s has been shown by L. W. Swanson et al.[46] in FEM studies of Cs layers on various refractory metal. This relationship is $\Delta\phi_m = 1.09\ (1.78 - \phi_s)$ eV and is believed to be associated with the degree of ionic character in the bond. If $\phi_s = 2.6$ eV is used for the Zr/O/W(100) surface, the calculated $\Delta\phi_m$ is -0.89 eV, and $\phi_m = 2.6 - 1.89 = 1.71$ eV. The experimental finding is $\phi_m = 2.12$ eV, yielding a difference of 0.4 eV. We conclude, from this that ϕ_s is not the only fundamental substrate parameter governing ϕ_m for Cs adsorption on the Zr/O/W(100) surface. Figure 51 is a plot of the minimum work function ϕ_m attained by Cs adsorption versus the initial surface

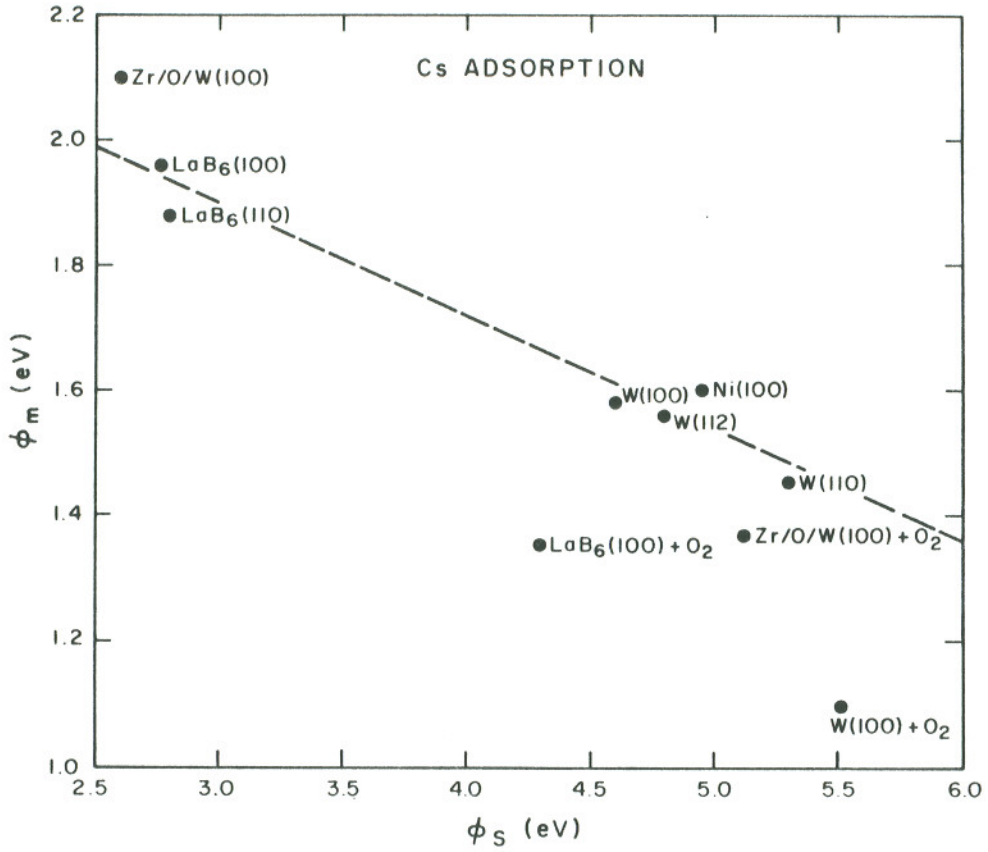

Figure 51. Minimum work function ϕ_m with Cs adsorption versus substrate work function ϕ_s. $LaB_6(100)$, $LaB_6(100 + O_2$: Ref. 47; Zr/O/W(100), Zr/O/W(100) + O_2: this study; $LaB_6(110)$: Ref. 48; W(100): Ref. 49; W(112): Ref. 50; Ni(100): Ref. 51; W(110): Ref. 52.

work function ϕ_s for various metallic single crystal substrates[47-51]. The oxygen-containing Zr/O/W(100) and oxygen-covered LaB_6(100) surfaces have been included for comparison. The work function of clean LaB_6(100) is $\sim$ 2.7 eV, rather close to the work function of the Zr/O/W(100) surface. Yet the minimum work functions of the two surfaces with Cs adsorption are in poor agreement, suggesting that ϕ_s is not the fundamental substrate parameter governing $\Delta\phi_m$ for the Cs/Zr/O/W(100) systems. A possible explanation for the Zr/O/W(100) deviation from the line in Figure 52 is because the latter is a three component system and the effect of O_2 on the surface dipole moment is different from that of the bare surface. It appears that there may be a line of different slope in Figure 51 passing through the points where O is coadsorbed.

For the O/Zr/O/W(100) studies, the work function increases from 2.7 eV to $\sim$ 5.0 eV, by dosing the surface with only 0.6 L of oxygen. On the other hand, a 0.6 L dose of oxygen on the W(100) surface changes the substrate work function by only 0.5 eV.[39] This difference is shown in Figure 52. The possible explanation for this sharp increase in work function is as follows: The excess oxygen adsorbs mainly on W sites located between the ZrO sites. Due to the Zr-O sticking out in the O/Zr/O/W(100) surface, fewer W sites are available than on the clean W surface, thus saturation occurs at a much lower oxygen dose if the same sticking coefficient is assumed on both surfaces. The larger $\Delta\phi$ associated with the

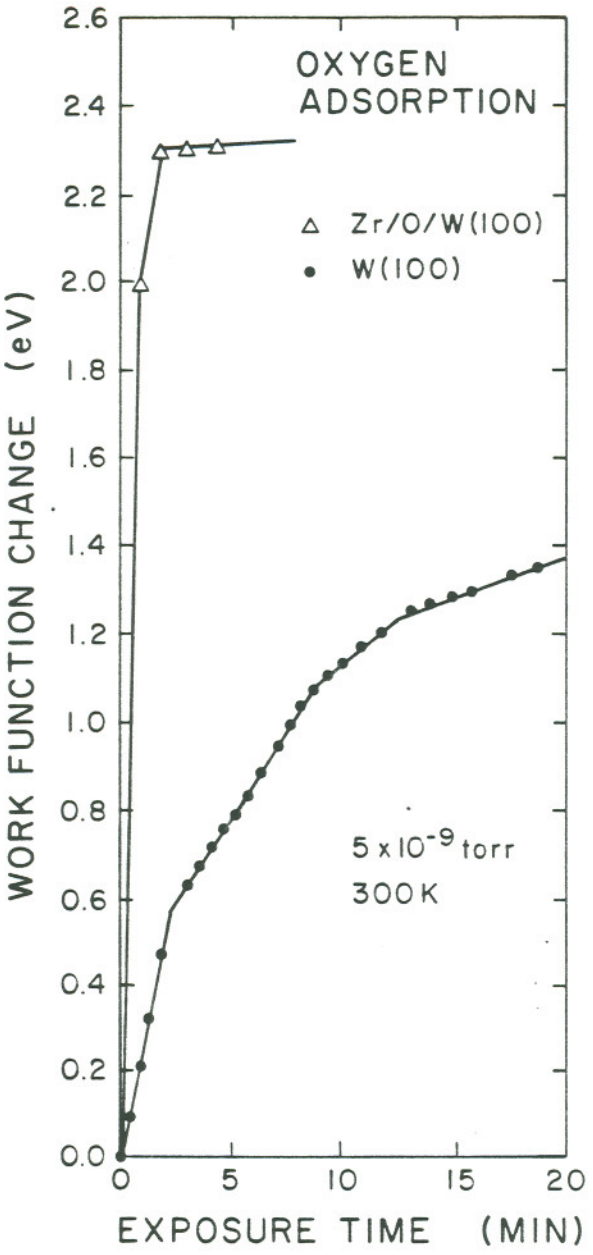

Figure 52. Work function change of W(100) as a function of time during exposure to 5 x 10^{-9} torr O_2. (Ref. 39) O_2 adsorption on Zr/O/W(100) shown for comparison.

Zr/O/W surface with excess oxygen adsorption must be due to a considerably larger dipole moment μ_{OW}. This is likely due to the polarization of the O-W sites by neighboring ZrO sites.

Heating this unequilibrated surface to 1600 K decreases the oxygen concentration on the surface, either through desorption or diffusion into the bulk as a Zr-O complex, thereby causing the work function to decrease. In the above case (θ_o = 0.19), the work function changes from 4.7 eV to 3.6 eV.

For the O/Zr/O/W(100) surface, the minimum work function attained with Cs adsorption for different excess O coverages is shown in Figure 53. This curve is linear, illustrating the strong effect of excess O coverage on the minimum work function. It should be noted that the data for both thermally equilibrated and unequilibrated O layers fall on the same curve, suggesting that the net effect of thermal equilibration of excess oxygen layers at 1600 K is the same as adsorbing less oxygen initially. This means that the transition from disordered to ordered O/Zr/O/W(100) must have little effect upon the electronic properties of the surface at least with respect to subsequent Cs adsorption. The relative Cs coverage at ϕ_m for Cs adsorption on the unequilibrated and thermally equilibrated surfaces are shown in Figure 54. This value is a rather smooth function of the amount of excess oxygen. No Cs Auger data are available for these cases, so unity sticking coefficient was assumed.

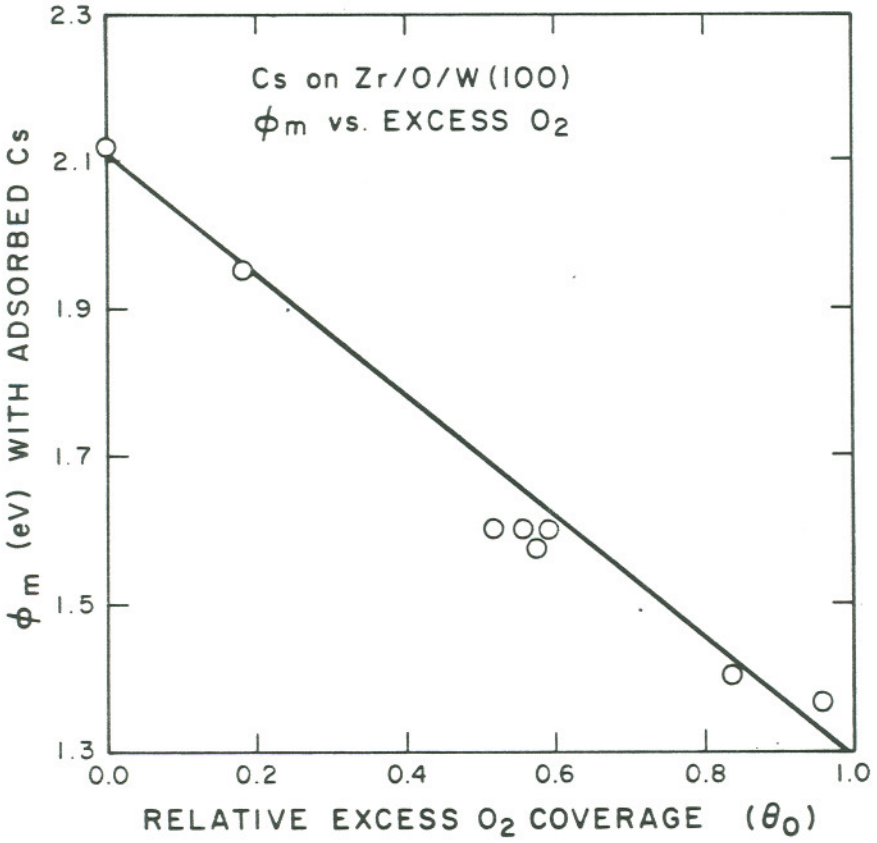

Figure 53. Work function minimum attained by cesium adsorption as a function of excess oxygen adsorbed on the Zr/O/W(100) surface.

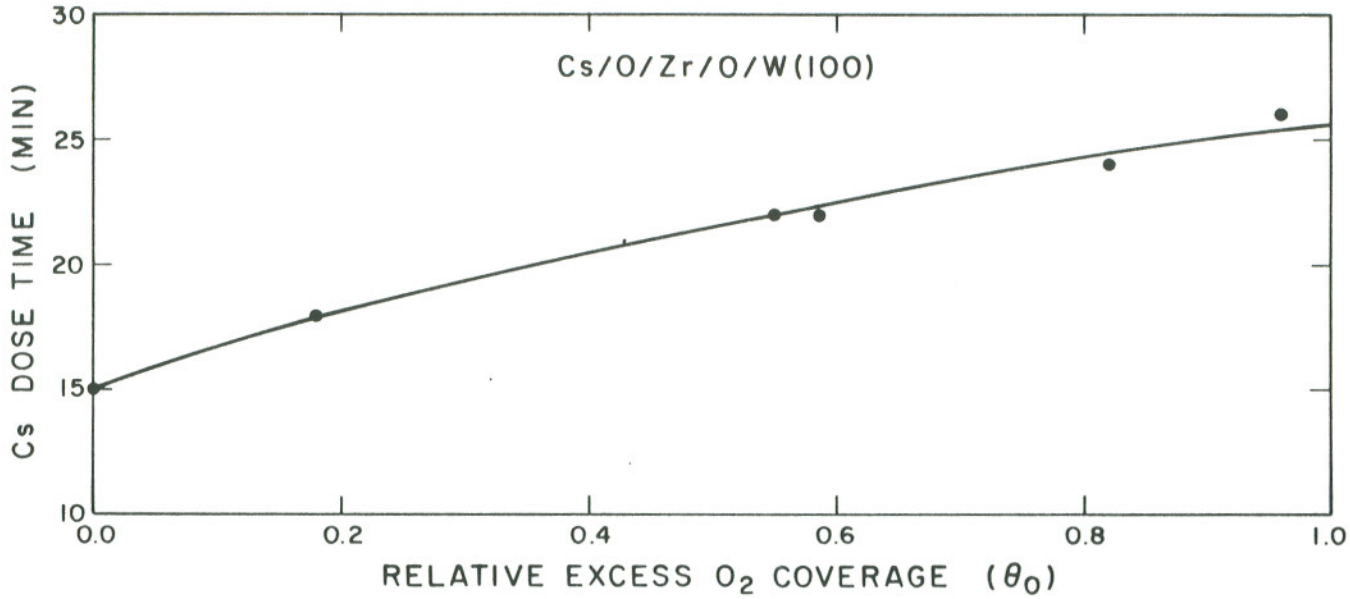

Figure 54. Cs dose time to achieve ϕ_m for various excess O coverages on the Zr/O/W(100) surface.

To interpret these results let us assume that the total work function change $\Delta\phi$ due to adsorbed excess oxygen and cesium is given by

$$\Delta\phi = \Delta\phi_o + \Delta\phi_{Cs} \tag{25}$$

where

$$\Delta\phi_o = k\mu_o\theta_o$$

$$\Delta\phi_{Cs} = -k\mu_{Cs}\theta_{Cs}$$

and k is a constant, θ_o and θ_{Cs} are the excess oxygen and cesium relative coverages. The respective dipole moments are μ_o and μ_{Cs}. Equation 25 can also be written as follows:

$$\Delta\phi = \phi_o - \phi_{ZrO} + \phi_{Cs} - \phi_o$$

$$= \phi_{Cs} - \phi_{ZrO}$$

or

$$\Delta\phi = \phi_{Cs} - \phi_{ZrO} = k(\mu_o\theta_o - \mu_{Cs}\theta_{Cs}) \tag{26}$$

At the minimum work function

$$\Delta\phi_m = \phi^m_{Cs} - \phi_{ZrO} = k(\mu_o\theta_o^m - \mu_{Cs}\theta^m_{Cs}) \tag{27}$$

The Figure 55 results suggest that $\theta^m_{Cs} = k'\theta_o$ or, in other words, the excess O opens up additional binding sites, possibly the B sites indicated in Figure 49. On the basis of this equation 27 becomes

$$\Delta\phi_m = k\theta_o(\mu_o - k'\mu_{Cs}) \tag{28}$$

The plot of $\Delta\phi_m$ as a function of the relative excess oxygen coverage shown in Fig. 55 indicates that $|\Delta\phi_m|$ increases, but not linearly with θ_o. The slight non-linearity may be due to a decrease in μ_{Cs} due to an increasing contribution of mutual depolarization as would be expected with the increasing value of θ^m_{Cs}. Thus, we conclude that the B sites open up sites for additional Cs adsorption on the Zr/O/W(100) surface and that the value of μ_{Cs} is considerably larger for the B sites than for the oxygen free Zr/O/W(100) surfaces, i.e. $|k'\mu_{Cs}| > \mu_o$. This, coupled with the face that $\theta^m_{Cs} \propto \theta_o$, provides the basis for the reduction in ϕ_m with increasing θ_o.

The nature of the B sites for Cs adsorption are such that a highly polar bond is formed between the underlying chemisorbed O and Cs. Because of the ionic bond formed by the Cs 6s electron with one of the O sp orbitals, the Cs effective diameter is reduced from its metallic value. In this way intimate ionic bonding with the underlying electronegative O occurs.

5.1.e. Comparison with $Cs/O/LaB_6(100)$

Oxygen preadsorbed to coverages of 0.45, 0.8, and 0.9 followed by cesium adsorption on a $LaB_6(100)$ surface produced work function minima of 1.45, 1.3 and 1.3 eV, respectively. The minimum work function for $Cs/O/LaB_6(100)$ is close to that of Cs/O/Zr/O/W(100),

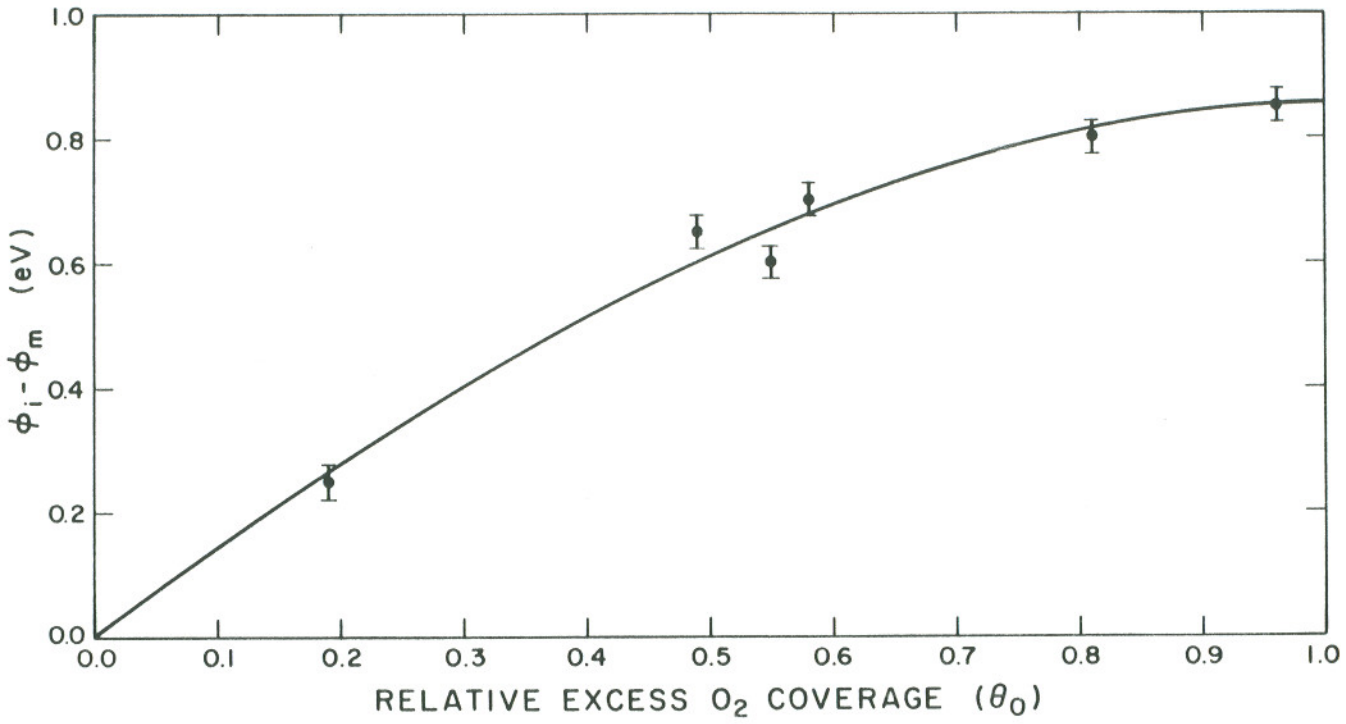

Figure 55. Plot of maximum work function reduction ($\phi_i - \phi_m$) by Cs adsorption vs. excess oxygen coverage on the O/Zr/W(100) surface. ϕ_i = initial work function before Cs adsorption at each excess O_2 coverage. ϕ_m = minimum work function attained by Cs adsorption. $\Delta\phi_m = (\phi_i - \phi_m)$.

even though LaB_6(100) and Zr/O/W(100) are different substrates. The only similarity is the work function value, which indicates that the underlying chemisorbed oxygen is an important parameter for determining ϕ_m.

5.1.f. Comparison with Cs/O/W(100)

The Cs/O/W(100) system has been studied a great deal in the past. Table IV is a summary of results by various investigators, with our Cs/O/Zr/O/W(100) data included for comparison.

TABLE IV

SUMMARY OF THE MINIMUM WORK FUNCTION VALUES OF Cs/O/W(100) STUDIES BY VARIOUS INVESTIGATORS. THE OXYGEN COVERAGE N_o IS INDICATED

Authors	ϕ_m (eV)	N_o ($\times 10^{-14}$)	Method
L. W. Swanson (1967) R. W. Strayer [46]	1.1	3.2 or 4.2	FE
J. M. Chen (1972) C. A. Papageorgopoulos [44]	1.3	7.14	Farnsworth type electron gun
J. L. Desplat (1974) [49]	1.1	5.4 or 12	Kelvin probe
This Study Cs/O/Zr/O/W(100)	1.40	excess 4.32 (0.6 L dose)	FERP

J. L. Desplat[49] has done the most thorough study of the Cs/O/W(100) system. Some of his results are shown in Figure 56. The variation of ϕ_m with the oxygen coverage N_o is plotted on this Figure, together with two normalized quantities - the exposure time t_m to reach ϕ_m and the initial slope ϕ_o' of the ϕ vs θ_{Cs} curve.

In the present study, there are some similarities in behavior with Figure 55. In this study, ϕ_m decreases with increasing oxygen coverage for the Zr/O/W(100) surface. (Figure 53). In Figure 56, ϕ_m decreases when oxygen coverage is in the range $0 \sim 5 \times 10^{14}$ and $8 \times 10^{14} \sim 12 \times 10^{14}$ atoms cm^{-2}. It seems that the adsorption behavior for Cs/O/Zr/O/W(100) is close to that of Cs/O/W(100) at an initial oxygen coverage between 0 and 5×10^{14} atoms cm^{-2}. It has been assumed that the initial oxygen coverage of Zr/O/W(100) is $\theta_o = 0.85$. If an oxygen coverage of 10^{15} atoms cm^{-2} for $\theta_o = 1$ on W(100) is assumed, the initial oxygen coverage for Zr/O/W(100) is 8.5×10^{14} atoms cm^{-2}.

5.1.g. Thermal Desorption Spectrometry of Cs

In the Cs/Zr/O/W(100) system, two major low energy binding states have been found for Cs adsorption. The Cs desorption is complete at 900 K. In the $Cs/LaB_6(100)$ experiment,[47] the desorption is also complete at 900 K, and the shapes of the two desorption spectra are quite similar.

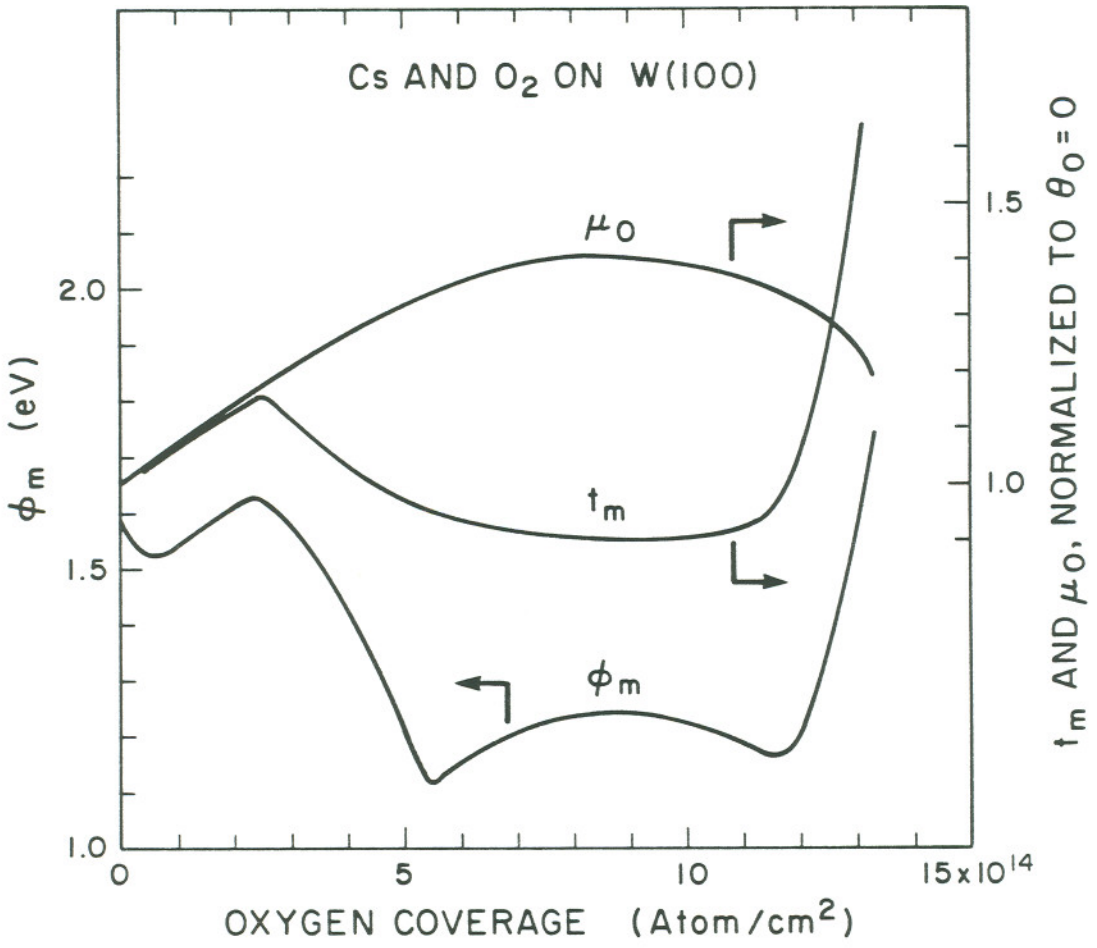

Figure 56. Change of work function minimum (ϕ_m), Cs adsorption time (t_m) required to achieve ϕ_m and slope (μ_o) at the origin of the ϕ vs. Cs coverage curve, all as functions of pre-adsorbed oxygen coverage, for the W(100) surface. Both t_m and μ_o are normalized to the case of no preadsorbed oxygen. (Ref. 49).

In the Cs/O/Zr/O/W(100) case, the shapes of desorption spectra become more complex, with more high energy binding states appearing due to the effect of preadsorbed oxygen. As already discussed, the B sites increase the number of sites for subsequent Cs adsorption. Also, Cs desorption is not complete until around 1300 K for the Cs saturated surface, so an adsorbed cesium layer has greater thermal stability on preadsorbed excess oxygen layers than on the Zr/O/W(100) surface without excess oxygen. The reason for this has been mentioned earlier: due to larger charge transfer from the adsorbed Cs to oxygen, a stronger Cs-O bonding has been created. The Cs/O/LaB_6(100) system also has the same characteristics. The terminal desorption temperature (1200 K) for Cs on preadsorbed oxygen on LaB_6(100) is higher than the terminal desorption temperature (900 K) for Cs on clean LaB_6(100).[47]

For the thermally equilibrated Zr/O/W(100) surface, the major Cs desorption peak shifts to lower temperature because of weaker bonding and less oxygen. For the Cs saturated 0.3 L O_2 thermally equilibrated surface (θ_o = 0.19), the desorption spectrum shows two major binding states appearing at low temperature. The shape of this spectrum is similar to that of Cs on Zr/O/W(100) without excess O. It has been shown that the work function of the 0.3 L O_2 thermally equilibrated surface drops from 4.7 eV to 3.6 eV during 1600 K heating. Auger analysis indicates that the excess oxygen coverage is 0.19 on this equilibrated surface. Both these two parameters are approaching

the values for clean Zr/O/W(100). The TDS data for this surface provide further support of this statement. We thus conclude that the oxygen concentration on the surface decreases due to this thermal equilibration, and the surface approaches the Zr/O/W(100) surface. It should be noted, however, that the terminal desorption temperature is still very high compared with that of the Zr/O/W(100) surface, since a small amount of excess oxygen is still available. In other words, the desorption spectrum is determined by the distribution of various Cs adsorption sites, and this distribution depends upon the excess oxygen coverage.

The TDS spectra for Cs/O/W(100) have not been previously reported in the literature, so direct comparison of these results cannot be made. However J. M. Chen et al. have observed the change in work function with Cs desorption from a Cs-covered surface of clean W(100), (4 x 1)-O and (2 x 1)-O. By heating to 1300 K, the work functions of these surfaces return to the work functions of the clean W(100) or the (2 x 1)-O.

In TDS studies of Cs from W(110), J. L. Desplat[54] has determined the terminal desorption temperature to be 1700 K for 0.71 ML oxygen coverage. This temperature is much higher than that of Cs/O/Zr/W(100).

5.1.h. Electron Reflection

The total electron reflection coefficient as a function of incident electron energy is shown in Figure 57. This figure

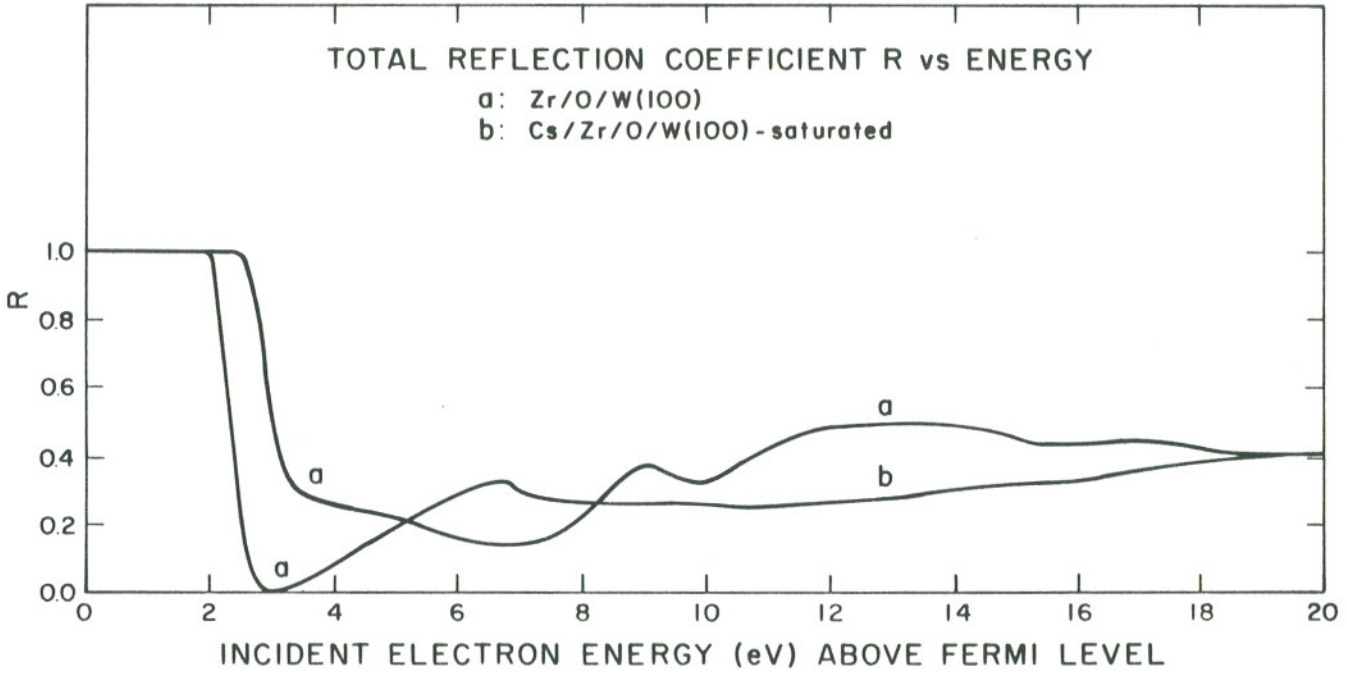

Figure 57. Total reflection coefficient, R, for low energy electrons normally incident upon a Zr/O/W(100) surface, with and without a saturated Cs adsorbed layer.

indicates a significant reduction in total reflection coefficient near threshold accompanying Cs adsorption on the Zr/O/W(100) surface. At 1 eV above threshold (onset of current collection), the adsorption of a saturated layer of cesium decreases the reflection coefficient from $\sim$ 0.29 to $\sim$ 0. In thermionic converter collector applications, lower reflection means more current collection, therefore the lower reflection coefficient for Zr/O/W(100) surface with saturated Cs layer will be a desirable feature in convertor collector applications. Also, reflection may indicate something about the electronic properties of the surface. For higher reflection, it suggests the occurrence of a band gap relatively free of surface states.

5.2. Cs Adsorption on W(100)

5.2.a. Work Function

The Cs/W(100) system has been extensively studied in the past. Table V is a summary of results of various investigators. In Table V, values of μ_o, the dipole moment in the limit of zero coverage, are also included. According to a simple electrostatic argument, μ_o is given by

$$\mu_o = -5.3 \times 10 \left[\frac{d\Delta\phi}{dn}\right]_{n\to o} \text{ (Debye)} \qquad (22)$$

In this study, if a saturated Cs coverage of 4.3×10^{14} cm^{-2} is used, then μ_o = 12.3 Debye.

Several conclusions can be drawn from Table V. The minimum work function ϕ_m and monolayer work function ϕ_p measured in this study are reasonably close to other investigators' results. The absolute work function is measured here using the FERP technique, whereas only relative work functions were obtained from the techniques used by other investigators. The initial dipole moment determined in this study is lower than the dipole moment observed by others, although it is in good agreement with the value of 12.6 Debye predicted by Gadzuk,[59,60] using the many body theory. In general, then, these data substantiate the initial cleanliness of the W(100) surface used for our Zr/O/W(100) studies.

TABLE V

THE SUMMARY OF RESULTS OF Cs/W(100) STUDIES BY VARIOUS INVESTIGATORS

Authors	ϕ_m (eV)	ϕ_p (eV)	μ_o(100) (Debye)	Technique
L.W. Swanson (1967) R.W. Strayer[46]	1.60	1.76	13.2	Field Emission
T.J. Lee (1971) D.H. Blott[55]	1.795	1.82	15.8±0.8	Kelvin
D.L. Fehrs (1968) R.E. Stickney (1971)[56]	1.77	1.82	15.0	Electron-beam Retarding Potential
V.B. Voronin (1972) A.G. Naumovets A.G. Fedorus[57]	1.50	1.89		Electron-beam Retarding Potential
H. Jakusch (1973)[58]	1.45	∿1.9		CPD
J.L. Desplat[49]	1.58±0.02	1.80±0.02		Kelvin
This Study	1.65±0.05	1.95±0.05	12.3	FERP

5.2.b. Thermal Desorption Spectrometry of Cs

Cs adsorption on W(100) has been studied in great detail in the past. The following is a brief history of that work. A clear c(2 x 2) LEED pattern has been observed at a very low Cs coverage, which was then replaced by a hexagonal pattern at higher coverage. MacRae et al.[61] interpreted the above result as the formation of a duolayer. Based on this model MacRae et al. associated a minimum in the work function versus Cs coverage curve with 7.5×10^{14} atoms cm^{-2} of Cs coverage. The above model is not consistent with results of other studies, where it is found that at room temperature Cs forms a poorly ordered single layer, and that a work function minimum occurs before the completion of the layer. These discrepancies were discussed by Fehrs et al[62] and Schmidt.[63]

Subsequently, Voronon et al.[57] reported that the c(2 x 2) was absent when their Cs source was extensively outgassed, and they attributed the c(2 x 2) to the impurity. The first ordered structure of the cesium film observed at 300 K was p(2 x 2). The maximum of the intensity of the corresponding diffraction beams correlates with the passage of the work function through a minimum. This is followed by a gradual increase in the cesium film density which terminates in the formation of a close-packed monolayer having a pseduo-hexagonal structure matched to the substrate at an adsorbed-atom concentration $N = 5.0 \times 10^{14}$ cm^{-2}. J. M. Chen et al.[64] found that the previously reported c(2 x 2) structure for Cs on W(100) was due to small amounts

of H_2 accumulated on the surface at the beginning of Cs desorption. These H atoms, in the presence of Cs, form patches of c(2 x 2). So, according to this model based on LEED experiments by V. B. Voronin et al., the adsorption of Cs on W(100) involves two sites. At low coverages (less than 0.25 monolayer) the Cs atoms are thought to occupy the fourfold sites. At higher coverages, it is thought that bridge positions become occupied, ultimately forming a pseudo-hexagonal closed-packed array with saturation occurring at 1/2 monolayer.

In this study, there are two peaks in each desorption curve. According to Section 4.6.d., desorption of the high energy chemisorbed phase is a first-order reaction with a fixed activation energy, and desorption of the low energy chemisorbed phase is a first-order reaction with an activation energy dependent on coverage. Clearly, these two phases are consistent with the model by V. B. Voronin et al..

The angular dependence of photoemission from Cs 5p core levels suggests that these are not pure core levels, but have some band-like character.[65] R. L. Gerlach and T. N. Rhodin have also reported that alkali metal atoms adsorbed on Ni repel one another at all coverages forming a single layer.[66] Furthermore, the forces between alkali metal adatoms on Ni(110) are highly anisotropic. These nonclassical anisotropic forces are probably reactions via the metal's conduction electrons, as treated

lated to the indirect inter-adsorbate interactions via the metal's conduction electrons, as treated by Grimley.[67]

TDS from Cs/W(100) has not been reported previously in the literature. However, reported studies of Cs, Na and K/Ni(110) have shown desorption characteristics similar to the behavior observed in this study for Cs/W(100). They all have a desorption peak at high binding energy, so correlations with Cs, Na and K/Ni(110) are made here. Ni is an fcc crystal and the surface structure of Ni(110) is similar to the surface structure of W(110) which is a bcc crystal. The surface atom spacings for Ni(110) and W(100) are 3.49 Å and 3.25 Å, respectively. The following is a summary of the structure analysis and binding energies associated with alkali adsorption on Ni(110) made by R. L. Gerlach and T. N. Rhodin.[66]

Graphs of the proposed surface structure versus coverage of Na, K and Cs on Ni(110) are shown in Figure 58. From LEED analysis, Na, K and Cs on Ni(110) probably form coherent surface structures for less than 0.25 monolayer and form one-dimensional incoherent structures for coverages greater than 0.25 monolayer. The Rx(3 x 3) structure and Rx(2 x 2) structure are for Na on Ni(110) with θ = 0.11 and θ = 0.25, respectively. The notation Rx means that the coherent rows of Na atoms are shifted randomly in the x-direction.

The TDS for Na, K and Cs on Ni(110) are shown in Figure 59.[18] These desorption rate curves have considerable structure, which correlates with the significant changes which occur in the corres-

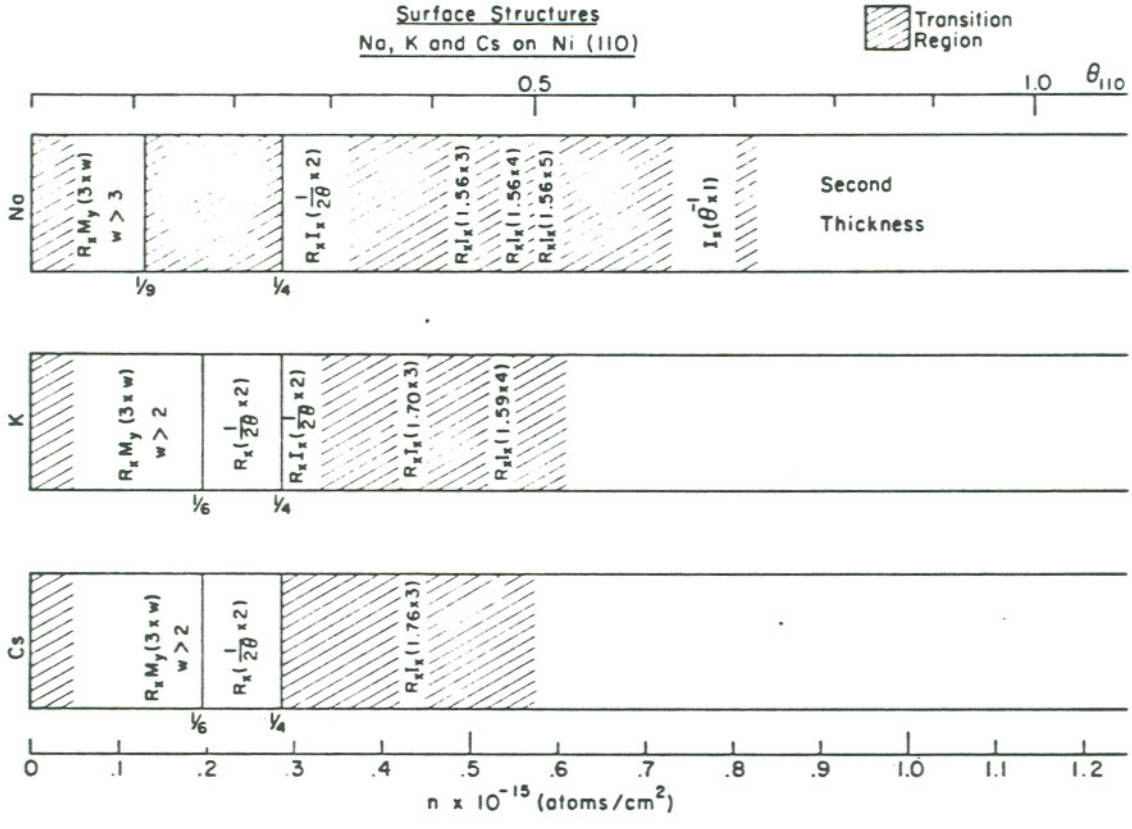

Figure 58. Graph of surface structure observed for Na, K, and Cs on Ni(110). (Ref. 66).

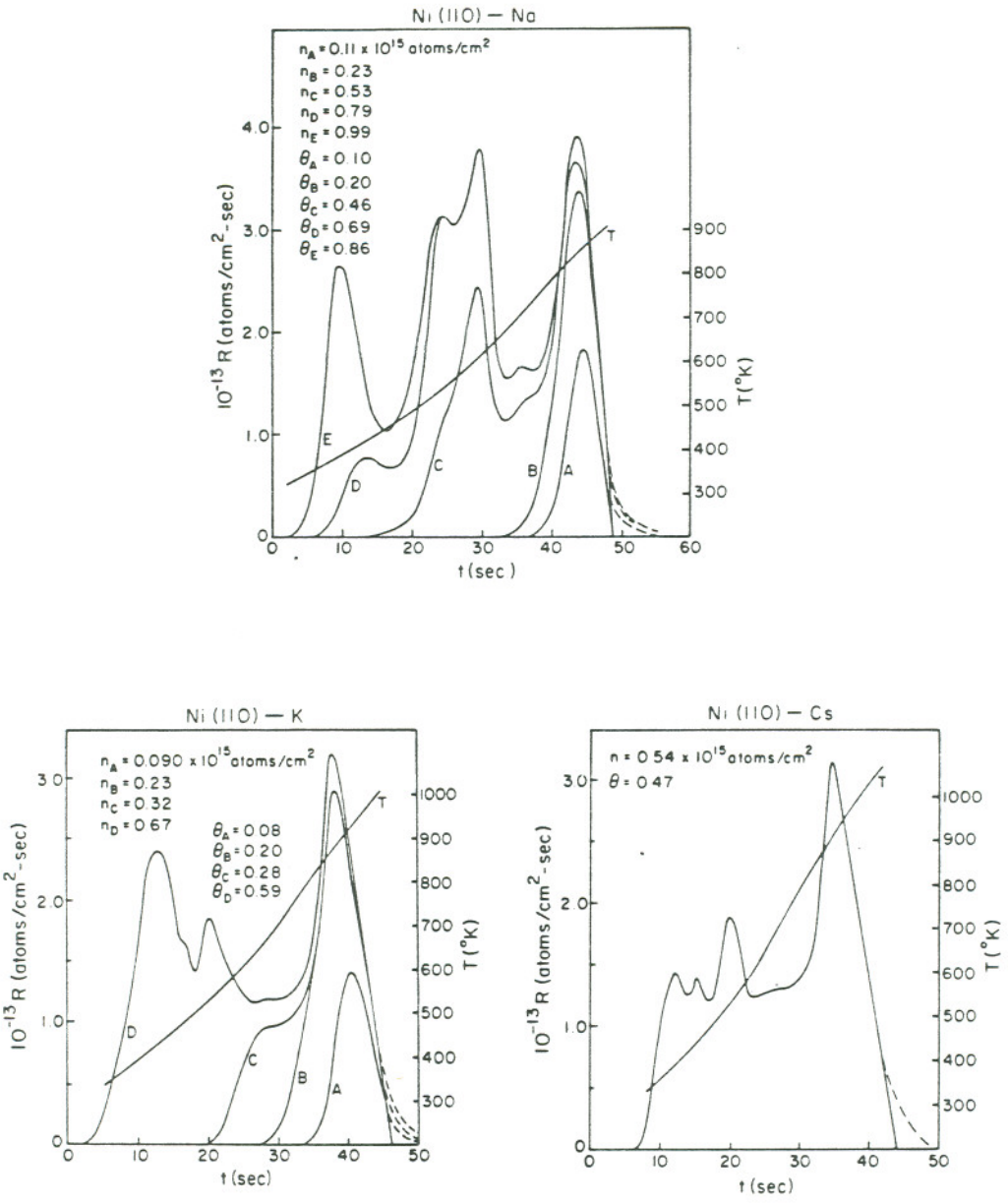

Figure 59. Thermal desorption spectra obtained for alkali metals on Ni(110). a: Na on Ni(110); b: Cs on Ni(110); c: K on Ni(110). Data from Ref. 18.

ponding surface structures (see Figure 58). There is a rather sharp peak around 900 K for Cs on Ni(110) for the coverages θ = 0.25. This peak probably corresponds to Rx(2 x 2) structure. Also, as the coverage increases, this peak shifts only slightly to lower temperature. In the present study, the temperature of the high binding energy state does not change with coverage. Therefore, these correlations offer additional evidence that the high energy chemisorbed phase is associated with p(2 x 2) structure and that the bonding depends purely on the surface geometry.

The desorption energies for Cs on W(100) in this work were calculated from Eq. 19 for various coverages. The desorption energies are 1.43, 1.51, 1.66 and 1.82 eV for the low energy chemisorbed state. The terminal desorption temperature for θ_{Cs} = 0.17 is around 1110°K. If this temperature is used in calculating the neutral desorption in the low coverage limit, the neutral desorption energy E_a is 2.82 eV.

The Cs^+ ion desorption spectra for Cs on W(100) are presented in Figure 47. The equilibrium rates of desorption of ions and atoms are related through the Saha-Langmuir equation

$$\frac{k^+}{k^\circ} = \frac{w^+}{w^\circ} \exp\left[\frac{\phi_o - V_o}{K_T}\right] \qquad (24)$$

where w^+ and w^o are the statistical weights of the ionic and atomic states, ϕ_o is the work function of the system at 0 K and V_o is the first ionization potential of Cs (3.9 eV). Therefore, appreciable

Cs^+ ion desorption occurs when the work function of the desorbing surface is over 3.9 eV. The ion desorption energy can be estimated roughly through Redhead's equation in the following way: The starting desorption temperature for $\theta_{Cs} = 0.08$ is 800 K. If this temperature is used, the calculated ion desorption energy $E_i = 2.16$ eV. This ion desorption energy also fits within 0.1 eV the Schottky equation near zero Cs coverage:

$$E_i = E_a + I - \phi_o \tag{25}$$

I being the Cs atom ionization energy (3.9 eV) and ϕ_o being the W(100) work function (4.65 eV).

Table VI is a summary of measurements of the desorption of Cs ions and atoms from W in the low coverage limit by various investigators. Again, good agreement exists between our desorption energy data and others.

TABLE VI

EXPERIMENTAL DATA ON THE DESORPTION OF CESIUM IONS AND ATOMS FROM TUNGSTEN IN THE LOW COVERAGE LIMIT.

Authors	Substrate	E_a(eV)	E_i(eV)	Technique
T.J. Lee and R.E. Stickney[68]	W(100)	2.78	2.05±0.02	Modulated molecular beam
	W(110)	3.00	1.77±0.02	
Koenig and Pigford[69]	W(100)	2.77±0.05	2.05±0.05	Thermal desorption
Gavrilyuk et al.[70]	W(100)	2.8		Steady state molecular beam
	W(100)	3.2		
This study	W(100)	2.81		Thermal desorption

CHAPTER 6

CONCLUSIONS

The substrate work function ϕ_s, the work function minima ϕ_m of the Cs adsorption and the heating temperatures T_m at the work function minima for the various adsorption systems investigated here are summarized in Table VII.

For the higher ϕ_s, the lower ϕ_m is obtained. The Cs/Zr/O/W(100) system does not give the lowest work function minimum, even though Zr/O/W is the lowest work function substrate. Also, for lower ϕ_m, the T_m is higher. The Cs adsorption on the high work function substrate surface is more stable up to a high temperature than on the low work function surface. The Cs/Zr/O/W(100) system is the least thermally stable system in this table. This implies that the bonding between Cs and Zr/O/W(100) is the weakest. The Cs/W(100) bonding is stronger than that of Cs and Zr/O/W(100) and the bonding between Cs and the O/Zr/O/W(100) surface is the strongest. These experimental results can be explained by the theory from Gomer and Swanson which was discussed in Chapter 2. The differences between I_{Cs} and ϕ_s are 1.2, -0.8 and -1.3 eV respectively, for the Cs/Zr/O/W(100), Cs/W(100) and Cs/O/Zr/O/W(100) systems. The high negative value of $I_{Cs} - \phi_s$ for the Cs/O/Zr/O/W(100) system suggests an ionic bonding, in contrast to a more metallic bonding for the other systems.

TABLE VII

SUMMARY OF T_m, ϕ_m AND ϕ_s FOR Cs ADSORPTION ON THE Zr/O/W(100), O/Zr/O/W(100) AND W(100) SURFACES

	T_m (°K)	ϕ_m(eV)	ϕ_s(eV)
Cs/Zr/O/W(100)	350	2.1	2.7
Cs/W(100)	480	1.7	4.7
Cs/O/Zr/O/W(100)	520	1.4	5.2

The lowest ϕ_m in the Cs/O/Zr/O/W(100) system is probably due to the higher electronegativity difference between the Cs atom and the excess oxygen in the sites of the O/Zr/O/W(100) surface.

The results presented here indicate the significant effects of adsorbed excess O_2 on the Cs adsorption/desorption characteristics of the low work function Zr/O/W(100) surface. The minimum work function attained for Cs adsorption on Zr/O/W(100) is 2.12 eV, while pre-adsorbed excess O_2 can reduce the minimum value to 1.37 eV. Excess O_2 increases the thermal stability of the Cs layer, producing a variety of binding states of energy higher than those observed without excess O_2. Equilibration of excess O_2 layers at 1600 K reduces both the surface Zr and O concentrations, but the corresponding change in Cs adsorption/desorption characteristics appears to be due primarily to the decrease in surface O_2.

Measurements of low energy electron reflection from the Zr/O/W(100) surface with and without adsorbed Cs indicate that the presence of Cs reduces the reflection coefficient of Zr/O/W(100) from $\sim$ 0.27 to $\sim$ 0.0 at 1 eV above threshold.

There are two desorption sites for Cs adsorption on W(100), a fact which was confirmed by TDS in this study. The high binding energy state is coverage independent, and the low binding energy state is coverage dependent. Desorption of Cs^+ can be explained in terms of the Saha-Langmuir and Schottky equations.

REFERENCES

1. L. R. Danielson and L. W. Swanson, Surf. Sci. 88, 14, 1979.
2. J. B. Taylor and I. Langmuir, Phys. Rev. 44, 423, 1933.
3. J. L. Desplat, Surf. Sci. 34, 588, 1973.
4. J. L. Desplat, NASA Contract No. NAS2-9001, May, 1979.
5. V. N. Shrednik, Sov. Phys. - Solid State 3, 1268, 1961.
6. R. A. Collins and B. H. Blott, Surf. Sci. 10, 349, 1968.
7. G.E. Hill, I. Marklund, J. Martinson and B. J. Hopkins, Surf. Sci. 24, 435, 1971.
8. L. W. Swanson and L. C. Crouser, Phys. Rev. 163, 662, 1967.
9. L. W. Swanson and N. A. Martin, J. Appl. Phys. 46, 2029, 1975.
10. P. R. Davis, Surf. Sci. 91, 385, 1980.
11. J. Topping, Proc. Roy. Soc. (London) A114, 67, 1927.
12. L. D. Schmidt and R. Gomer, J. Chem. Phys. 42, 3573, 1965; 43, 2055, 1965; 45, 1605, 1966.
13. R. W. Gurney, Phys. Rev. 47, 479, 1935.
14. R. Gomer and L. M. Swanson, J. Chem. Phys. 38, 1613, 1963.
15. C. B. Duke and M. E. Alferieff, J. Chem. Phys. 46, 923, 1967.
16. E. W. Plummer, J. W. Gadzuk and R. D. Young, Sol. State Commun. 7, 487, 1969.
17. J. W. Gadzuk, Surf. Sci. 6, 133, 159, 1967.
18. R. L. Gerlach and T. N. Rhodin, Surf. Sci. 19, 403, 1970.
19. N. D. Lang and W. Kohn, Phys. Rev. B 1, 4555, 1970.

20. N. D. Lang, Phys. Rev. B 3, 1215, 1971.

21. N. D. Lang, Sol. State Commun. 9, 1015, 1971.

22. E. P. Gyftopoulos and J. D. Levine, J. Appl. Phys. 33, 67, 1962.

23. Thomas A. Flaim and P. Darrell Ownby, Surf. Sci. 32, 519, 1972.

24. D. Steiner and E. P. Gyftopoulos, Report on 27th Annual Conf. on Physical Electronics, Cambridge, Mass. 160, 1967.

25. L. Pauling, The Nature of the Chemical Bond, 3rd ed. Cornell University Press, Ithaca, New York, 1960.

26. R. L. Gerlach, Ph.D. thesis, Cornell University, Feb. 1969.

27. P. R. Davis and H. R. Poppa, J. Vac. Sci. Technol. 15, 1771 (1978).

28. Della Porta et al., SAES Getter S., Technical Report Tr. 18, 1-20151, Milano, Italy, Sept. 1968.

29. R. W. Strayer, W. Mackie and L. W. Swanson, Surf. Sci. 34, 225, 1973.

30. L. W. Swanson and L. C. Crouser, Phys. Rev. 163, 622, 1967.

31. Russel D. Young and Howard E. Clark, Phys. Rev. Lett. 17, 351, 1966.

32. P. J. Estrup and E. G. McRae, Surf. Sci. 25, 1, 1971.

33. G. Ertl and J. Küppers, Monographs in Modern Chemistry, Vol. 4: Low Energy Electrons and Surface Chemistry (H. F. Ebel, ed., Verlag Chemie, Weinheim, 1974).

34. A. W. Smith and S. Aranoff, J. Phys. Chem. 62, 684, 1958.

35. G. Ehrlich, J. Appl. Phys. 32, 4, 1961.

36. P. A. Redhead, Vacuum 12, 203, 1962.

37. G. A. Haas, A. Shih and R. E. Thomas, J. Appl. Phys. 47, 5400, 1976.

38. L. R. Danielson, Thermo Electron Corporation Report 7910, 1980.

39. E. Bauer, H. Poppa and Y. Viswanath, Surf. Sci. 58, 517, 1976.

40. M. Bacal, J. L. Desplat and T. Alleau, J. Vac. Sci. Tech. 9, 851, 1972.

41. T. E. Madey, Surf. Sci. 33, 355, 1972.

42. B. J. Hopkins, G. D. Watts, A. R. Jones, Surf. Sci. 52, 715, 1975.

43. A. E. Abey, J. Appl. Phys. 40, 284, 1969.

44. C. A. Papageorgopoulos and J. M. Chen, Surf. Sci. 39, 313, 1973.

45. P. R. Davis, Final Report, NASA Contract NAS2-9629, 1978.

46. L. W. Swanson and R. W. Strayer, J. Chem. Phys. 48, 2421, 1968.

47. S. A. Chambers, P. R. Davis and L. W. Swanson, Surf. Sci. 118, 93, 1982.

48. L. W. Swanson, D. R. McNeely and M. A. Gesley, NASA CR:-159649. (NASA - Lewis Reserach Center, August 1979).

49. J. L. Desplat, Thesis University of Paris - Orsay, 1974.

50. C. A. Papageorgopoulos and J. M. Chen, J. Vac. Sci. Technol. 9, 570, 1972.

51. C. A. Papageorgopoulos and J. M. Chen, Surf. Sci. 52, 40, 1975.

52. J. L. Desplat and C. A. Papageorgopoulos, Surf. Sci. 92, 97, 1980.

53. J. M. Chen and C. A. Papageorgopoulos, Sol. State Commun. 11, 999, 1972.

54. J. L. Desplat, Report, NASA Contract NAS2-9001, May, 1979.

55. T. J. Lee, D. H. Blott and B. J. Hopkins, J. Phys.F. (Metal Phys.) 1, 309, 1971.

56. D. L. Fehrs and R. E. Stickney, Surf. Sci. 8, 267, 1968; 24, 309, 1971.

57. V. B. Voronin, A. G. Naumovets and A. G. Fedorus, JETP Letts. 15, 370, 1972.

58. H. Jakusch, Thesis, University of Karlsruhe, 1973.

59. J. W. Gadzuk, Surf. Sci. 6, 133, 1967.

60. J. W. Gadzuk, The Structure and Chemistry of Solid Surfaces, Ed. G. A. Somorjai (J. Wiley, New York), 1969.

61. A. U. MacRae, K. Müller, J. J. Lander and J. Morrison, Surf. Sci. 15, 483, 1969.

62. D. L. Fehrs, T. J. Lee, B. J. Hopkins and R. E. Stickney, Surf. Sci. 21, 197, 1970.

63. L. D. Schmidt, J. Vac. Sci. Tech. 10, 218, 1973.

64. C. A. Papageorgopoulos and J. M. Chen, J. Phys. C: Sol. State. Phys. 6, L279, 1973.

65. N. V. Smith, P. K. Larsen and S. Chiang, Phys. Rev. B 16, 2699, 1977.

66. R. L. Gerlach and T. N. Rhodin, Surf. Sci. 17, 32, 1969.

67. T. B. Grimley, Proc. Phys. Soc. (London) 90, 751, 1967; 92 776, 1967.

68. T. J. Lee and R. E. Stickney, Surf. Sci. 32, 100, 1972.

69. D. Koenig and T. H. Pigford, Report on 26th Annual Conf. on Physical Electronics, (MIT, 1966), 126.

70. V. M. Gavrilyuk, Yu. S. Vedula, A. G. Naumovets and A. G. Fedorus, Sov. Phys. -Solid State 9, 881, 1967.

BIOGRAPHICAL NOTE

Hsiung-Ku Chen was born July 24, 1952 in Taiwan, Republic of China. He earned a B.S. degree in Physics from Fu-Jen University, Taipei, Taiwan in 1974 and a M.S. in Physics from Temple University, Philadelphia, in 1976. Before leaving Taiwan to attend Temple University, Hsiung-Ku Chen worked as a research assistant at Kolin Electronic Company and as a job training instructor at Tatang Electrical Company.

Mr. Chen enrolled in a Ph.D. program in Physics at the Oregon Graduate Center in the fall of 1976. After completing his research under the supervision of Professor L. W. Swanson, he returned to Taiwan in 1981 to accept an engineering position in the process development department of the Electronics Research and Service Organization of the Industrial Technology Research Institute, where he is currently employed. His current employment is well matched to his long-term interests in experimental and applied physics, namely, physical electronics and communications systems.